Broadband Light Absorption Based on Nanostructured Resonators and Multimodal Photodetectors

By

Soongyu Yi

A dissertation submitted in partial fulfillment of
the requirements for the degree of

Doctor of Philosophy

(Electrical and Computer Engineering)

at the

UNIVERSITY OF WISCONSIN-MADISON

2019

Date of final oral examination: 4/29/2019

The dissertation is approved by the following members of the Final Oral Committee:
Mikhail Kats, Professor, Electrical and Computer Engineering
Zhenqiang Ma, Professor, Electrical and Computer Engineering
Zongfu Yu, Professor, Electrical and Computer Engineering
Victor Brar, Professor, Physics

Abstract

Optical resonance has been employed as an effective means for enhancing the light-material interaction in conventional optoelectronic devices. Although there has been a great amount of recent interest in 2D material based optoelectronic devices, the ultrathin feature of 2D material limits the amount of time for photons interacting with the materials. The light-material interaction must be significantly enhanced in order for 2D materials to achieve device efficiencies that are comparable to those based on conventional thick semiconductors. Nanostructured graphene such as nano disks and ribbons support localized plasmonic resonances which can significantly enhance its absorption profile but suffer from narrow bandwidth. This thesis will demonstrate enhancing the bandwidth of a 2D material resonator under a multi-resonator approach based on plasmonic resonances of graphene. These multi-resonators have different geometry that support resonances at different frequencies. Owing to their deep subwavelength sizes, graphene resonators can be closely packed in space, resulting in a high optical density of states, which enables the broadband light absorption.

Another important feature of optoelectronic devices besides the light absorption efficiency is the functionality of the device itself. While conventional photodetectors can detect the intensity of light, they are incapable of acquiring other important information, such as the incident angle of the light. The intensity information alone is sufficient for traditional applications, such as photography. However, its limitation becomes apparent in advanced imaging tasks. For example, a single image of the intensity cannot reveal depth-information of objects in a scene, which requires directional information. This thesis will present a multimodal photodetector that can measure both the intensity and the incident angle of light. It is based on non-Hermitian coupling between two Si nanowire elements. By electrically contacting each nanowire to form photodetectors, they afford measurement of the internally stored optical energy through simple photocurrent measurements. Angle sensing is done by simply monitoring the photocurrent difference. In addition to angle sensing, array of multimodal photodetectors are capable of sensing the wavefront of an incident light.

Acknowledgements

First and foremost, I would like to sincerely thank my advisor, Prof. Zongfu Yu for providing me a great opportunity to perform research under his guidance. It is true that research is not always fun or interesting. Sometimes, you get lost or lose motivation during the long journey. However, Zongfu has always provided his sincere advice so that I could enjoy all the hard works with great motivation and interest until the last moment of my PhD journey.

I would also like to thank my dissertation committee members, Prof. Zhenqiang Ma, Prof. Mikhail Kats, and Prof. Victor Brar for their valuable comments and suggestions.

I would like to acknowledge my colleagues for their contribution towards my research. Ming Zhou derived coupled mode theory equations and helped with optical measurements. Zhu Wang provided advice on optical theory and device fabrication. Dianjing Liu worked on network analysis of pixel arrays. Minkyu Cho, Kwagneun Kim, Honghyuk Kim, Sangjune Cho, Jeongpil Park provided advice on device fabrication. Quinn Leonard, Hal Giles, Kurt Kupcho offered technical support in the cleanroom. My acknowledgement also goes to Erfan Khoram, Yixuan Tan, Sam Belling, Nabeel Moin, Ang Chen, Lei Ying, Zhicheng Wu, Boyuan Liu for their valuable help.

Last but not least, I would like to thank my family members, my dad, my mom, my grandma and my brother for their unconditional love and support.

Table of Contents

List of Figures

Fig. 2.6. Perfect absorption achieved by the superradiance of 4 graphene ribbons. The graphene ribbons are doped at low level of 0.2 eV and sit on a 2 μm thick Si (n=3.42) substrate, which is easy to fabricate and offers excellent infrared transparency. The widths of ribbons are 45 nm, 60 nm, 75 nm, and 90 nm with 5 nm spacing. The periodicity is 315 nm. The substrate is on a reflecting mirror. Graphene is doped at 0.2eV with $\omega_p = 1.62 \times 10^{15}\ rad/s$, and collision frequency $\gamma = 4.5 \times 10^{12}\ s^{-1}$. The superradiance creates an absorption peak with 100% absorption. Moreover, the peak has enhanced bandwidth compared to individual ribbons alone (red lines Fig. 2.6).

Fig 3.1. Schematic of absorption cross-section (dashed line). Solid color disks represent the geometrical size of the nanoresonators. Colors represent different frequencies. a) Arrays of a single type of resonator with an absorption cross-section slightly larger than the geometrical size. Since the absorption cross-section can fill the space, efficient large-area absorption can be achieved for a single frequency of ω_1. b) Arrays of three types of resonators with different resonant frequencies. The absorption is inefficient because the absorption cross-sections of different frequencies cannot cover the entire space. c) Resonators with much smaller geometrical sizes enable efficient broadband absorption. Due to their small geometrical sizes, resonators can be closely packed so that the absorption cross-sections at different frequencies can all cover the entire space.

Fig. 3.2. (a) Absorption cross-section of a square graphene resonator with a size D = 100 nm. Dielectric constant of substrate is 2.1 and the thickness t = 1.6 μm. The simulation is performed with a periodic boundary condition with a very large period. The inset is the field distribution at the resonant frequency. Open circles are simulation and the solid line is coupled mode theory. (b) Ratio between the absorption cross-section (σ_a) and the geometric cross-section (σ_g) for different dimensions of graphene D. (c) Absorption rate and coupling rate as a function of graphene dimension D. (d) Resonant frequency shift with respect to graphene dimension. One side is fixed to 100nm, the other side w is varied from 100 nm to 200 nm. $E_{x(y)}$ represents the incident light in the x (y) polarization state.

Fig. 3.3. Linear relationship between coupling rate and $1/p^2$ (red star). Period-dependent absorption (black circle) for arrays of graphene squares. The dimension of the square is 100 nm x 100 nm.

Fig. 3.4. a) Absorption spectra for periodic arrays with only A-type resonator (stars), with only B-type resonator (circles), and with both A- and B-type resonators (solid line). Dot-dashed curves are based on coupled mode theory. b) Ratio between total spectral cross-section (ρ_{AB}) and the upper bound of spectral cross-section ($\rho_A + \rho_B$) as the distance between two resonators dx increases from 20 nm to 200 nm.

Fig. 3.5. a) Absorption spectra for periodic arrays with only A-type resonator (red circles), with

only B-type resonator (black circles), and with both A- and B-type resonators (solid line). Dashed curves are based on coupled mode theory. b) Ratio between total spectral cross-section (ρ_{AB}) and the upper bound of spectral cross-section ($\rho_A + \rho_B$) as Δd varies from 0 nm to 80 nm. Distance between two graphene resonators is 50 nm.

Fig. 3.6. a) Layout of a broadband light absorber based on multiple graphene resonators. Period is 850nm, dielectric constant of the substrate is 2.1 and the thickness is 1.6 μm. b) Absorption spectra of broadband light absorber in Fig. 3.6(a) with a mobility of 10,000 $cm^2V^{-1}s^{-1}$ (high μ) and 1,000 $cm^2V^{-1}s^{-1}$ (low μ). In comparison, dashed line shows the absorption by optimized arrays of single-type graphene resonator with limited bandwidth. A mobility of 10,000 $cm^2V^{-1}s^{-1}$ is used.

Fig. 4.1. (a) Concept of incident angle detection using a lens with a diameter d that produces a finite-sized spot in its focal plane when illuminated by an off-axis, collimated beam. The angular spread $\Delta\theta$ resulting from diffraction limits the minimum detectable angle change given a limited signal-to-noise ratio in a real optical measurement. (b) and (c) Directional hearing of animals based on the detection of an interaural time difference (ITD) or interaural intensity difference (IID). Δt is the arrival time difference and ΔI is the intensity difference between two ears. (d) Head structure of a gecko showing internal coupling between two eardrums. The distance *d* between two ears is typically 1 to 2 cm and thus on a subwavelength scale with respect to audible sound wavelengths in the range from 8.5 - 34 cm.

Fig. 4.2. (a) Schematic of the coupled mode theory for two resonators having amplitudes a_1 and a_2 separated by a distance d. S, γ_i, and γ_r quantify the power of the incident light, the imaginary part, and the real part of the coupling strength, respectively. (b) Ratio of the stored energy in two resonators. It strongly depends on the incident angle for the coupled case (red line), whereas it remains at 1 for decoupled resonators (black line). $d = 0.05\ \lambda_0$ and $\gamma = 0.01\ \omega_0$ is used for both $\gamma_c = 0$ and $\gamma_c \neq 0$ cases. $\gamma_c = 9.8 \times 10^{-3}\ \omega_0$ is used for $\gamma_c \neq 0$ case. (c) Example of the angular profile (blue curves) and the phase configuration of the radiation of the super and subradiant eigenstates for the case of electric dipole radiators. Here we assume the spacing between the two is much smaller (0.1 λ_0) than wavelength. Red and blue are used to indicate a phase difference of π.

Fig. 4.3. (a) Cross-sectional view of two Si nanowires on SiO_2 substrate with Poynting flux lines for a 45° incident angle θ. (b) Absorption ratio between two silicon nanowires for d = 100 nm (red) and d = 2 μm (black) as a function of incident angle. (c) Absorption profile $\sigma(\omega)|E|^2$ for different incident angles, normalized by the highest absorption density in each case. When d = 100 nm, absorption ratio change between two nanowires is clearly visible for different incident angles. (d)

Fig. 5.2. Drawback of a low spatial resolution for wavefront detection. Both detectors at (a) and (b) are not able to sense the rapid wavefront change (red line). Thus, they are not able to tell the wavefront difference between (a) and (b).

Fig. 5.3. (a) For normal incidence case, two neighboring pixels will absorb the same amount of light regardless of the incident angle of light. (b) With a mask on top of the pixels, light absorption ratio between two neighboring pixels are different and it becomes angle (θ) dependent.

Fig. 5.4. (a) Absorption ratio of two neighboring pixels versus the incident angle of light. (b) - (d) Gray scale image of pixel brightness for three different incident angles A ($\theta = 0°$), B ($\theta = 10°$), and C ($\theta = 20°$) as depicted in (a).

Fig. 5.5. Unit cell with 4pixels as 2 by 2 element arrangement which can be used to detect the incident angle of light in 3D space. Yellow arrow represents an incident angle of light. Green color represents pixels in an image sensor, and gray color represents a metallic mask.

Fig. 5.6. Calibration map of absorption ratio versus incident angle of an unit cell for all 6 possible ratio combinations.

Fig. 5.7. (a) Microscope image of a fabricated wavefront sensor showing an array of unit cells. Pixel size of the image sensor is 5.2 μm and the unit cell size is 10.4 μm. (b) Fabricated wavefront sensor mounted on a chip and a black plastic body.

Fig. 5.8. (a) Measurement setup for capturing the wavefront of a diverging beam at three different locations A, B and C. A biconvex lens is used to generate a diverging wave beyond the focal point. (b) Reconstructed wavefront at three different positions A, B and C. Wavefront have larger radius of curvature as the wavefront is captured further away from the focal point.

Fig. 5.9. The 4f- system used to measure the wavefront aberration caused from the PMMA layer. PMMA layer is located at the object plane and the wavefront sensor is located at the image plane.

Fig. 5.10 (a) Wavefront captured using our wavefront sensor. (b) Wavefront captured using a commercial Shack-Hartmann wavefront detector.

CHAPTER ONE

INTRODUCTION

1.1 Background

Optical resonance has been employed as an effective means for enhancing the light-material interaction in conventional optoelectronic devices. Along with emerging two-dimensional (2D) materials such as graphene which have promising potentials for optoelectronic applications because of their unique electronic band structures and low dimensionality, there has been a great amount of recent interest in 2D material based optoelectronic devices. However, ultrathin feature of 2D material limits the amount of time for photons interacting with the materials, resulting in an overall weak light-material interaction. For instance, the absorptance of a single layer of graphene is approximately 2.3% [1] which is too low to be useful for efficient optoelectronic devices. The light-material interaction must be significantly enhanced in order for 2D materials to achieve device efficiencies that are comparable to those based on conventional thick semiconductors.

There has been a great amount of recent interest in applying resonant enhancement in 2D materials. Existing methods can be divided into two categories. The first relies on conventional dielectric materials to construct optical resonators, such as Fabry-Perot cavities based on distributed Bragg reflectors [2] and guided resonances in photonic-crystal slabs [3, 4]. These approaches generally require sophisticated nanofabrication. The second category is based on the intrinsic plasmonic resonances. For instance, nanostructured graphene such as nano disks and ribbons support localized plasmonic resonances [5, 6, 7], particularly in the mid and far infrared spectral regimes. Such resonators do not require any additional dielectric material. Moreover, their resonant properties can be easily tuned by changing the geometrical shape. In both methods, 100%

light absorption has been shown by operating the resonators at the critical coupling condition [3, 8].

However, there has been one significant challenge existing in both aforementioned methods in that the efficient light absorption can only be achieved in a narrow spectral range, which is limited by the bandwidth of a single type of resonator. For instance, the full width at half maximum (FWHM) of the perfect absorption reported in [8] is only about 6% of the resonant frequency. In this thesis, I will describe how to enhance the bandwidth of a 2D material resonator under a multi-resonator approach based on plasmonic resonances of graphene.

Another important feature of optoelectronic devices besides the light absorption efficiency is the functionality of the device itself. While conventional photodetectors can detect the intensity of light, they are incapable of acquiring other important information, such as the incident angle of the light. The intensity information alone is sufficient for traditional applications, such as photography. However, its limitation becomes apparent in advanced imaging tasks. For example, a single image of the intensity cannot reveal depth-information of objects in a scene, which requires directional information. Another example is the light field camera, which uses information from incident angles to refocus even after the image is taken [9, 10]. To measure the incident angle, one has resorted to discrete optical components such as lenses or gratings together with photo-detecting pixels. These components are expensive to integrate and degrade the resolution. Only recently, have researchers been able to successfully integrate angle-sensitive pixels into a CMOS architecture [11, 12]. Their minimum size has been on the order of several microns as their operation relies on the use of gratings. With current scaling trends for imaging systems, the size of pixels is rapidly approaching the optical wavelength λ_0. This poses a seemingly unsurpassable challenge towards angle detection. Existing methods based on micro-lenses or gratings cannot be miniaturized indefinitely because diffraction effects will result in a decrease in the accuracy of the angular measurement. In this thesis, I will demonstrate that non-Hermitian coupling between neighboring photodetector elements can be exploited to realize an intrinsically subwavelength-sized angle sensing photodetector that can measure both the intensity and the incident angle of light. In addition, arrays of angle sensing photodetectors can be utilized to measure the wavefront of incident light.

1.2 Thesis overview

In chapter 2, broadband absorption based on superradiance of optical nanoresonators will be presented. These optical nanoresonators offer an excellent analog of quantum two-level systems. Studying optical analogs of the electromagnetically induced transparency (EIT) and the Fano interference has greatly stimulated the field of nanophotonics. In this context, the theoretical analysis is developed for the optical analog of superradiance in multiple nanoresonators. Unique superradiant effects are found for light absorption in nanoresonators, such as superradiance-induced transparency.

In chapter 3, a multiple-resonator approach based on nanostructured graphene to broaden the enhancement of light-material interaction will be presented. These nanostructures having different geometry support resonances at different frequencies. Owing to their deep subwavelength sizes, graphene resonators can be closely packed in space, resulting in a high optical density of states, which enables the broadband light absorption.

In chapter 4, a subwavelength photodetection pixel that can measure both the intensity and the incident angle of light is presented. It consists of two nanoscale optical resonators where two silicon nanowires are used as an example. Two nanowires can internally circulate light to produce standing electromagnetic waves. Because of the high refractive index of semiconductors, the sizes of resonators and their separation can be much smaller than the free-space optical wavelength. By electrically contacting each nanowire to form photodetectors, they afford measurement of the internally stored optical energy through simple photocurrent measurements. It will be shown that the two electrically-isolated and optically-coupled photodetectors allow angle-sensing by monitoring the difference in stored energy between the resonators.

Lastly, in chapter 5, I will demonstrate that an array of angle sensing pixels can be used to detect the wavefront of an incident light. Although Shack-Hartmann wavefront detector [13, 14] is the most widely used wavefront detector, there is a trade-off between the spatial resolution and the dynamic range in wavefront detection. Is this chapter, I will show that by placing a metallic mask on top of a CMOS image sensor, a wavefront detector with a spatial resolution that is an order of magnitude higher than the Shack-Hartmann wavefront detector can be achieved. In addition to that, the dynamic range is also greatly enhanced compared to Shack-Hartmann wavefront detector.

References

[1] K. Mak, M. Sfeir, Y. Wu, C. Lui, J. Misewich, and T. Heinz, "Measurement of the Optical Conductivity of Graphene," Phys. Rev. Lett. **101**, 196405 (2008).

[2] M. Furchi, A. Urich, A. Pospischil, G. Lilley, K. Unterrainer, H. Detz, P. Klang, A. M. Andrews, W. Schrenk, G. Strasser, and T. Mueller, "Microcavity-Integrated Graphene Photodetector," Nano Lett. **12**, 2773–2777 (2012).

[3] J. R. Piper and S. Fan, "Total Absorption in a Graphene Monolayer in the Optical Regime by Critical Coupling with a Photonic Crystal Guided Resonance," ACS Photonics **1**, 347–353 (2014).

[4] Y. Liu, A. Chadha, D. Zhao, J. R. Piper, Y. Jia, Y. Shuai, L. Menon, H. Yang, Z. Ma, S. Fan, F. Xia, and W. Zhou, "Approaching total absorption at near infrared in a large area monolayer graphene by critical coupling," Appl. Phys. Lett. **105**, 181105 (2014).

[5] F. H. L. Koppens, D. E. Chang, and F. J. García de Abajo, "Graphene Plasmonics: A Platform for Strong Light–Matter Interactions," Nano Lett. **11**, 3370–3377 (2011).

[6] S. Zhang, D. A. Genov, Y. Wang, M. Liu, and X. Zhang, "Plasmon-Induced Transparency in Metamaterials," Phys. Rev. Lett. **101**, 047401 (2008).

[7] H. Yan, X. Li, B. Chandra, G. Tulevski, Y. Wu, M. Freitag, W. Zhu, P. Avouris, and F. Xia, "Tunable infrared plasmonic devices using graphene/insulator stacks," Nat. Nanotechnol. **7**, 330–334 (2012).

[8] S. Thongrattanasiri, F. Koppens, and F. García de Abajo, "Complete Optical Absorption in Periodically Patterned Graphene," Phys. Rev. Lett. **108**, 047401 (2012).

[9] R. Ng *et al*. “Light field photography with a hand-held plenoptic camera”, *Stanford Univ. C.S. Tech report CSTR 2005-02* (2005).

[10] A. Wang, P. Gill, A. Molnar, “Light field image sensors based on the Talbot effect”, *Appl. Opt.* **48,** 5897–5905 (2009).

[11] A. Wang, P. Gill, A. Molnar, “Angle sensitive pixels in CMOS for lensless 3D imaging”, *Proc. Cust. Integr. Circuits Conf.* 371–374 (2009). doi:10.1109/CICC.2009.5280840

[12] S. Sivaramakrishnan, A. Wang, P. R. Gill, A. Molnar, “Enhanced Angle Sensitive Pixels for Light Field Imaging”, *2011 IEEE Int. Electron Devices Meet.* 191–194 (2011).

[13] B. C. Platt, R. S. Shack, “History and principles of Shack-Hartmann wavefront sensing”, *J. Refract. Surg.* **17**, S573–S577 (2001).

[14] J. Primot, “Theoretical description of Shack-Hartmann wave-front sensor”, *Opt. Commun.* **222**, 81–92 (2003).

CHAPTER TWO

THE OPTICAL ANALOG OF SUPERRADIANCE IN NANORESONATORS

2.1 Introduction

Discovered by Dicke in 1954 [1], superradiance describes a collective coherent effect in a cluster of identical quantum emitters: a single quantum emitter prepared in the upper level creates spontaneous emission with an intensity I; when N emitters are placed together within a wavelength dimension, the total emission intensity grows to N^2I, instead of the incoherent addition NI. The emitters have no direct near-field coupling, and yet their phases are synchronized. Such in-phase oscillation is mediated through the free-space field that they radiate to.

Compared to the analogs [2–11] of EIT [12] and Fano [13] interference, the optical analog of superradiance is more challenging to achieve. It requires N nanoresonators with deep subwavelength sizes placed within a wavelength dimension [14]. While the superradiance can be created with properly managed near-field interactions, which will be discussed later, a faithful analog of quantum emitters requires the near-field interaction to be minimal. The requirements of subwavelength sizes [15] and minimal near-field interaction rule out many nanoresonator candidates. In addition to the challenges in the implementation, theoretical treatments developed for quantum emitters also need to be adapted to include the light absorption in nanoresonators, which is of practical importance for optoelectronic devices.

2.2 Coupled mode theory for multi-resonator multi-channel

We present a classical optical theory for the analog of superradiance based on a multi-resonator multi-channel temporal coupled mode theory. The theory reveals unique superradiant absorption effects, such as superradiance-induced transparency where total absorption of N resonators is suppressed by a factor of $1/N$ with single resonator's absorption suppressed by $1/N^2$. This suppression effect is in great contrast to the enhancement effect in superradiant emission. It is also in great contrast to an intuitive dipole-approximation picture that is used to explain the N^2 emission enhancement [16]. The dipole approximation would predict that the absorption increases linearly with *N*. To validate theoretical predications, we simulate the analog of superradiance using graphene ribbon resonators [17–20], which offer deep subwavelength sizes as well as easy control of near-field interactions.

Note that the superradiant effect has been frequently noted in two-resonator systems in the optical analogs of EIT and Fano interferences [2,21–23]. In addition, *N*-resonator has also been studied before, but it was treated in an incoherent manner without considering neither the near-field nor the far-field interactions among resonators [24,25]. The work here provides a complete theoretical treatment of *N*-resonator system and demonstrates unique superradiant absorption effects.

Consider a cluster of *N* optical resonators. The damping mechanism in the resonator includes the light absorption by materials and the coupling to the free space radiation. The dynamics can be described with a temporal coupled mode theory [26,27]. From the energy conversation and the time-reversal symmetry, one can obtain the equation governing the interaction between multiple resonators and multiple free-space radiation channels [21,28]:

$$\frac{d}{dt}\boldsymbol{a} = (i\Omega - \Gamma)\boldsymbol{a} + D^T\,\boldsymbol{S}_{IN} \tag{1}$$

where $\boldsymbol{a} = (a_1, a_2, \dots, a_N)$ are the amplitudes of resonators normalized such that $|a_i|^2$ is the energy stored in the resonator. $S = (S_1, S_2, \dots, S_m)$ are the amplitudes of the power flux carried by each orthogonal radiation channel. *D* is the coupling rate between *N* resonators and m free-space channels. *T* is the transpose operator. The Hamiltonian Ω is given by:

$$\Omega = \begin{pmatrix} \omega_1 + \frac{i\gamma_1}{2} & .. & \Omega_{1N} \\ .. & .. & .. \\ \Omega_{N1} & .. & \omega_n + \frac{i\gamma_N}{2} \end{pmatrix} \tag{2}$$

where ω_i, γ_i are the resonant frequencies and the absorption rates, respectively. The off-diagonal elements Ω_{ij} are the *near-field interaction* among resonators due to the overlap of near fields. In addition to the near field, there is also a *far-field interaction* among resonators, represented by $\Gamma = \frac{1}{2}D^T D$. The far-field interaction is a direct consequence of energy conservation. Because all resonators couple to the same radiation fields and their radiation amplitudes add up coherently, the resonators needs to coordinate with each other in order to comply with the energy conservation law. This coordination is reflected by the far-field interaction term Γ, which is the key to the far-field superradiant effect.

The amplitudes of reflected lights are given by

$$\boldsymbol{S}_{out} = C\boldsymbol{S}_{in} + D\boldsymbol{a} \tag{3}$$

where *C* is a $m \times m$ matrix representing the direct transmission from the incident to the outgoing channels without routing through the resonators.

Consider a faithful analog of quantum emitters: *N* non-interacting identical resonators couple to a single radiation channel S_1. Without any near-field interaction, $\Omega = (\omega_0 + i\frac{\gamma_0}{2})\boldsymbol{I}$ is diagonal, where $\boldsymbol{I}$ is a *N*-dimensional identity matrix. The coupling to the channel is identical for all resonators $D = (\sqrt{\gamma_c}, \sqrt{\gamma_c}, \dots, \sqrt{\gamma_c})$.

2.3 Superradiant emission

First, a brief review of the superradiant emission. To study the emission, assume that there is no incident light i.e. $S_{IN} = 0$. For single resonator alone, using Eq.2 an Eq.3, it is easy to show that the amplitude of an excited resonator decays as $|a_i|^2 \sim \exp[-(\gamma_0 + \gamma_c)t]$. With N resonators together, the amplitude decays as $|a_i|^2 \sim \exp[-(\gamma_0 + N\gamma_c)t]$. The enhanced decaying rate due to the in-phase oscillation of all resonators directly leads to the an emission intensity N times stronger for each resonator, and N^2 stronger for all resonators together.

Now, consider the superradiant absorption in the presence of an incident field S_{IN}. The superradiant in-phase oscillation of resonators has more complex consequences on absorption. As a reference for comparison, the absorption of a single resonator alone is

$$A_s(\omega_0) = \frac{4\gamma_0\gamma_c}{(\gamma_0+\gamma_c)^2} \tag{4}$$

For N resonators, $C = -1$ is chosen such that D is real for Eq.3. We take $\frac{d}{dt} = i\omega$. Eq. 1 then becomes

$$a = \left(i(\omega I - \Omega) + \frac{1}{2}D^T D\right)^{-1} D^T S_{in} \tag{5}$$

Substitute Eq. 5 into Eq. 3, we have

$$S_{out} = -S_{in} + D\left(i(\omega I - \Omega) + \frac{1}{2}D^T D\right)^{-1} D^T S_{in} \tag{6}$$

Therefore

$$\frac{S_{out}}{S_{in}} = -1 + D\left(i\left(\omega - \omega_0 - i\frac{\gamma_0}{2}\right)I + \frac{1}{2}D^T D\right)^{-1} D^T \tag{7}$$

DD^T is a scalar representing the summation of all coupling rates. Using Eq. 7 and 8, we obtain the reflection $R = S_{out}/S_{in}$

$$|R(\omega)|^2 = \frac{(\omega-\omega_0)^2 + \left(\frac{\gamma_0}{2} - \frac{1}{2}DD^T\right)^2}{(\omega-\omega_0)^2 + \left(\frac{\gamma_0}{2} + \frac{1}{2}DD^T\right)^2} \tag{9}$$

Then the absorption is

$$A_N(\omega) = 1 - |R(\omega)|^2 = \frac{\gamma_0 DD^T}{(\omega-\omega_0)^2+\left(\frac{\gamma_0}{2}+\frac{1}{2}DD^T\right)^2} \tag{10}$$

with a peak value at the resonance frequency

$$A_N(\omega_0) = \frac{4\gamma_0 DD^T}{(\gamma_0+DD^T)^2} \tag{11}$$

where $DD^T = N\gamma_c$. Comparing Eq.4 and Eq.11, we can see that *N* resonators behave as if they were just a single "macro-resonator" with a coupling rate enhanced by *N* times. We next discuss three different regimes of superradiant absorption below.

First, for weakly absorptive resonators $\gamma_0 \ll \gamma_c$, the superradiance greatly suppresses the absorption. The absorption of a single resonator when alone is $A_s(\omega_0) \approx 4\gamma_0/\gamma_c$. Using Eq. 11, the total absorption of *N* resonators is

$$A_N(\omega_0) \approx \frac{1}{N}\frac{4\gamma_0}{\gamma_c} = \frac{A_s(\omega_0)}{N} \tag{12}$$

The absorption of the individual resonator in the *N*-resonator system is suppressed by N^2 times:

$$A'_s(\omega_0) = \frac{A_N(\omega_0)}{N} = \frac{A_s(\omega_0)}{N^2} \tag{13}$$

This suppression effect is in great contrast to the enhancement effect in the emission. It is caused by the *N*-fold enhanced coupling rate, which drives the resonator further away from the critical-coupling condition and leads to a weaker absorption. It is interesting to recognize that for a single weakly absorptive resonator alone, if we increase the coupling rate by *N* times, the absorption can only be reduced by *N* times, instead of N^2 times. Here the superradiant suppression of N^2 times is a coherent effect due to the far-field interaction among resonators.

Second, for strongly absorptive resonators $\gamma_0 \gg N\gamma_c$, above coherent effect is quenched. In this regime, a single resonator's absorption is $A_S \approx 4\gamma_c/\gamma_0$ when it is alone. In the presence of the superradiance, Eq.11 gives us a total absorption $A_t = NA_S$, a simple incoherent summation of *N* resonators. Individual resonators in the N-resonator system have the same absorption as the case when they are alone. In another word, resonators are not affected by the presence of others.

Lastly, Eq.11 also shows a superradiance-induced transparency effect: when $N \rightarrow \infty$, the total absorption approaches zero independent of the values of γ_0 and γ_c (Fig. 2.1(e)).

2.4 Superradiant absorption effects of graphene ribbons

To demonstrate above superradiant absorption effects, we perform simulations by numerically solving the full-wave Maxwell's equations. The nanoresonator is based on graphene ribbons. Graphene can be modeled using surface conductivity. Under random phase approximation, conductivity of graphene can be expressed in intraband and interband parts [29]. For the frequency range when $\hbar\omega \ll E_F$, the interband part can be neglected leaving only the intraband part as

$$\sigma_S^{intra} = \frac{2e^2 k_B T}{\pi\hbar^2} \ln(2\cosh\frac{E_F}{2k_B T}) \frac{i}{\omega + i\tau^{-1}} \tag{14}$$

where E_F is chemical potential and τ is relaxation time. Thus, conductivity of graphene is expressed in Drude-like form. The effective permittivity of graphene used for numerical simulation is obtained as [30]

$$\varepsilon(\omega) = 1 + i\frac{\sigma_S}{\varepsilon_0 \omega \Delta} \tag{15}$$

where Δ is the thickness of graphene. This equation is in identical form as the Drude model equation where plasma frequency can be expressed as

$$\omega_p = \left[\frac{2e^2 k_B T}{\pi\hbar^2 \varepsilon_0 \Delta} \ln(2\cosh\frac{E_F}{2k_B T})\right]^{1/2} \tag{16}$$

In our simulation, Δ= 1 nm, E_F= 0.4 eV, leading to plasma frequency $\omega_p = 2.3 \times 10^{15}$ rad/s.

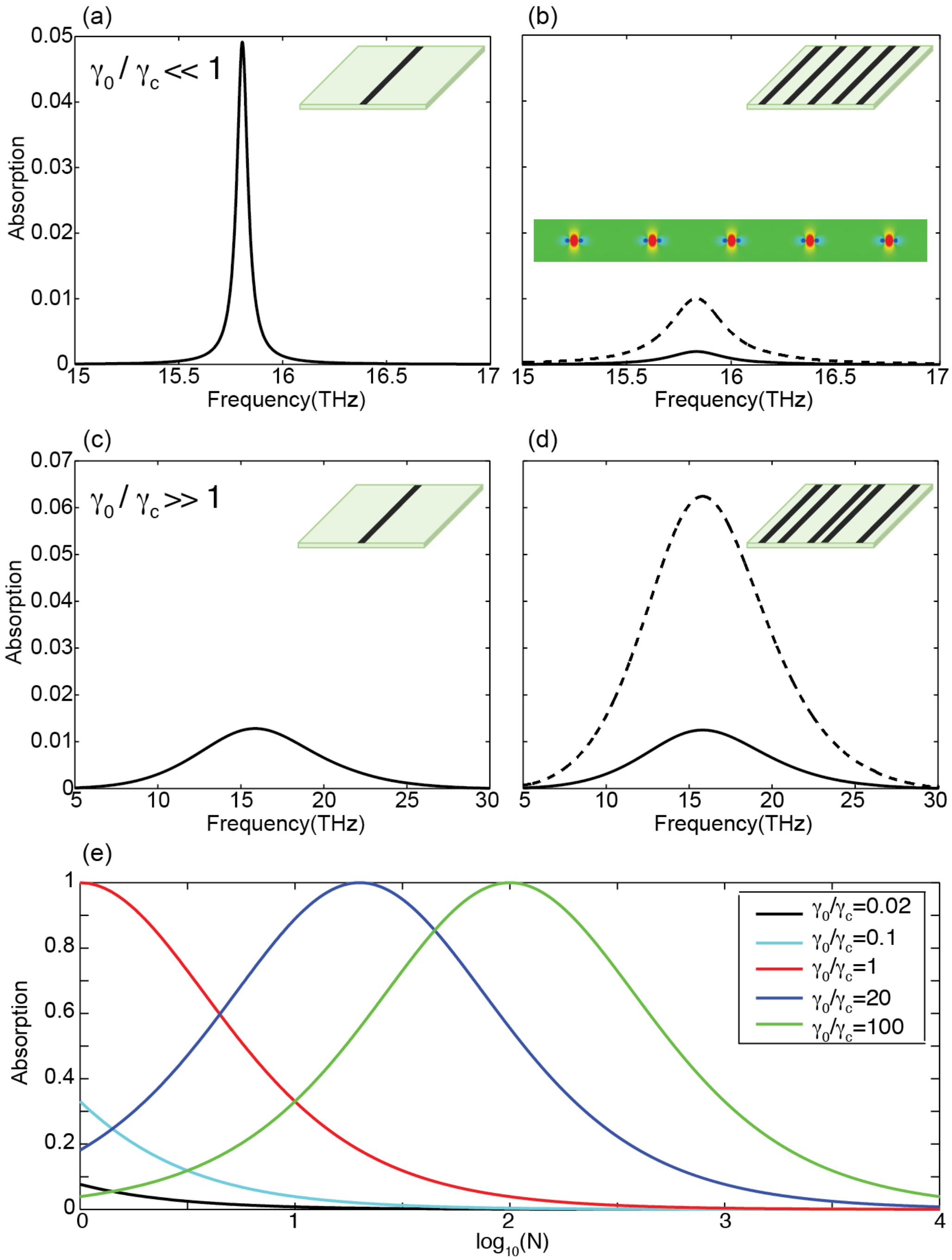

Fig. 2.1. Superradiant absorption in graphene ribbon nanoresonators, for weakly (a,b) and highly (c,d) absorptive cases. (a) Absorption by a single ribbon with a low collision frequency $5 \times 10^9\ s^{-1}$. (b) The superradiance of 5 ribbons suppresses the total absorption by 5 times (dashed line). Individual ribbon's absorption (solid line) is suppressed by 25 times. Inset: the schematic of

the structures (not-to-scale). Middle inset: the field distribution of the superradiant mode. (c) Absorption by a single ribbon with a high collision frequency $1.25 \times 10^{14}\ s^{-1}$. (d) The superradiance of 5 ribbons enhances the total absorption by 5 times (dashed line). Individual ribbon's absorption (solid line) remains the same. The substrate has a refractive index $n = 2$ and a thickness 2400 nm. Each ribbon is 250 nm wide, 1 nm thick, and infinitely long. The simulation domain is 10 μm wide. (e) The total absorption as a function of N calculated using Eq.11. Independent of the ratio of the absorption γ_0 and coupling γ_c rates, transparency is induced by the superradiance with increasing N.

A 250nm wide ribbon has a fundamental resonant mode with a free-space wavelength around 20 μm (Fig. 2.1(a)). Since the electric fields are tightly confined to the edges of ribbons, the near-field interaction is minimal even when they are placed closely. These properties are difficult to achieve in conventional dielectric materials. In the simulations, a transverse magnetic (TM) plane wave is normally incident from the top. A large computational domain is used to ensure sufficient spacing between ribbons. The spacings between ribbons can be equal (Fig. 2.1(b)) or random (Fig. 2.1(d)) as long as near-field interactions remain minimal. The specific boundary conditions do not affect the physics. Periodic boundary condition is used while perfect reflecting boundary conditions would offer the same effects.

First, we study the weakly absorptive case when $\gamma_0/\gamma_c \ll 1$. The superradiance of 5 ribbons (Fig. 2.1(b) inset) suppresses the individual ribbons' absorption by 25 times (solid line Fig. 2.1(b)) compared to when they are alone (Fig. 2.1(a)). The total absorption of 5 ribbons (dashed line Fig. 2.1(b)) is only 1/5 of the absorption of single ribbon alone. For the strongly absorptive regime $\gamma_0/\gamma_c \gg 1$, we use a high collision frequency of graphene to increase the absorption rate γ_0. In this case, the superradiance barely affects the individual resonators' absorption (solid line Fig. 2.1(d)) compared to that of a single ribbon alone (Fig. 2.1(c)). The total absorption of 5 ribbons is enhanced by 5 times as a result of incoherent addition (dashed line Fig. 2.1(d)). When N is sufficiently large, the superradiance induces a transparency effect with the absorption approaching zero. Such transparency effect is independent of the ratio of γ_0 and γ_c (Fig. 2.1(e)).

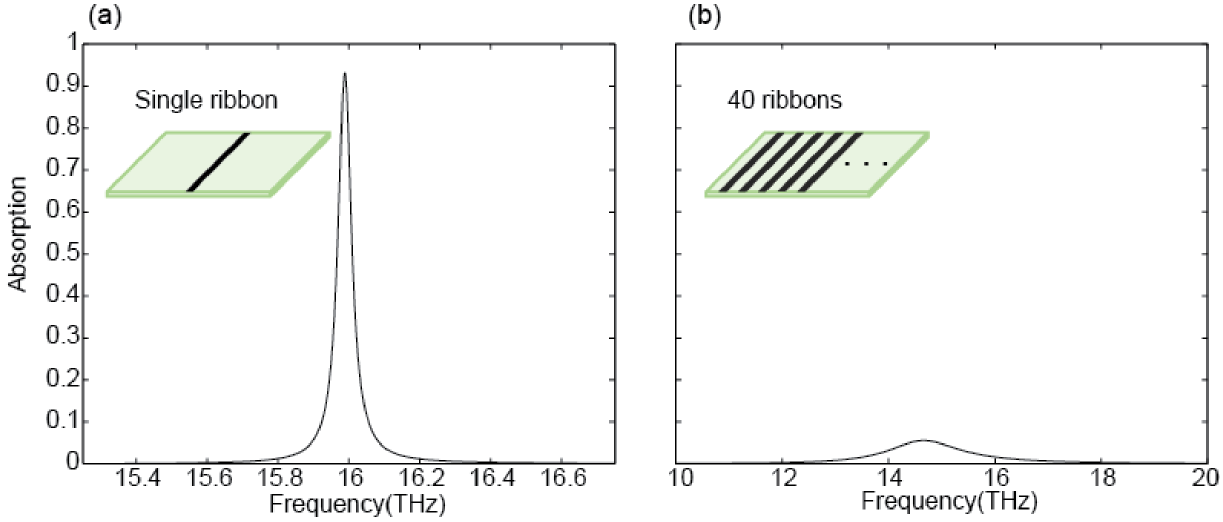

Fig. 2.2. (a) Single ribbon having absorption close to 100%. (b) Superradiant-induced transparency using 40 identical ribbons. The computational domain is 18 μm with a periodic boundary condition. The collision frequency is $\gamma = 1.25 \times 10^{11}\ s^{-1}$ and the doping level is 0.4 eV. The ribbon width is 250 nm on $2.5\mu m$ thick substrate (n = 2).

The simulation of superradiance-induced transparency is shown in Fig. 2.2. When the absorption rate is similar to the coupling rate, a single graphene resonator has a high absorption above 90% (Fig. 2.2(a)). For 40 identical ribbons, the superradiance significantly increases the coupling rate. As a result, the absorption is reduced close to zero (Fig. 2.2(b)).

In above discussion of the direct analog of quantum emitters, we have intentionally avoided the near-field interaction. In fact, near-field interactions when properly managed can also create superradiance. The near-field elements Ω_{ij} $(i \neq j)$ in the Hamiltonian Ω hybridize N resonators to form a new set of eigenmodes $U\boldsymbol{a}$, where U is a unitary transformation that diagonalizes Ω. The new eigenmodes couple to the free-space radiation with a coupling strength UD^T. We next show that if all Ω_{ij} $(i \neq j)$ have the same sign, the superradiance always occurs with all resonators oscillating in-phase. Moreover, this superradiant mode will either have the highest or the lowest eigenfrequency.

It is straightforward to show that Ω_{ij} $(i \neq j)$ can be expressed in real numbers if the system preserves the time-reversal symmetry. To see this, we write the resonators' fields in real functions, which is always possible for standing waves. Then, the time-reversal operator T has no effects on the fields, which means that the Hamiltonian matrix satisfies $T\Omega = \Omega T$. Therefore Ω must be real. Here we have neglected the absorption without affecting the conclusion. In addition, energy conservation requires $\Omega_{ij} = \Omega_{ji}^*$ [27], which leads to $\Omega_{ij} = \Omega_{ji}$.

Next, we show that if $\Omega_{ij}(i \neq j) > 0$, the superradiant mode always exists at highest eigenfrequency. For the normalized eigenmode with the highest frequency, we can write it as $|s\rangle = \sum_{i=1,K} c_i |a_i\rangle - \sum_{i=K+1,N} c_i |a_i\rangle$ with positive and real c_i when the system preserves the time-reversal symmetry. Now we define another state $|x\rangle = \sum_{i=1,K} c_i |a_i\rangle + \sum_{i=K+1,N} c_i |a_i\rangle$, and evaluate

$$\rho \equiv \langle s|\Omega|s\rangle - \langle x|\Omega|x\rangle = -4 \sum_{i=K+1}^{N} \sum_{j}^{K} c_i c_j \Omega_{ij} \tag{17}$$

Since $|s\rangle$ is the eigenmode with the highest frequency, the variational theorem requires $\rho \geq 0$. However, the coefficients on the right hand side of Eq.17 determine that ρ must be non-positive. Therefore $\rho = 0$ and $N = K$, i.e. all N resonators oscillating with the same phase. Similarly, we can show that if near-field interactions are all negative $\Omega_{ij} < 0$, the superradiance mode always exists and is located at the lowest eigenfrequency.

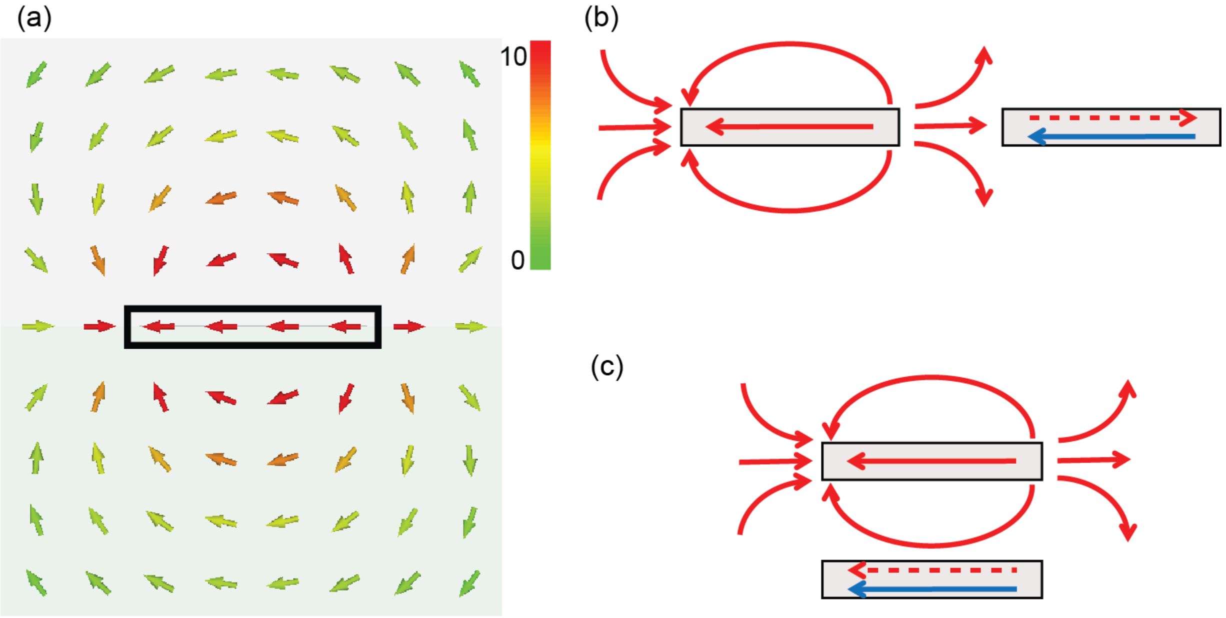

Fig. 2.3. Near-field interactions among nearby graphene ribbons. (a) The electric field distribution of a ribbon resonator. (b). Negative interaction in the side-by-side configuration. The field generated by resonator i (red dashed arrow) is in the opposite direction of that of resonator j (blue arrow). (c) Positive interaction in the top-bottom configuration where fields are in the same direction.

For numerical simulations, we configure the spatial arrangement of graphene ribbons to tune their near-field interactions. Fig. 2.3(a) shows the distribution of the electric field around a graphene ribbon resonator. The near-field interaction is determined by the field overlap $\int_{V_j} E_i(\vec{r})E_j(\vec{r})(1 - \epsilon(\vec{r}))d\vec{r}$ where E_i, E_j are the electric fields generated by the i^{th} (red lines Fig. 2.3(b)-(c)) and j^{th} resonator (blue lines Fig. 2.3(b)-(c)), respectively. The integration is performed on the site of the

j^{th} resonator V_j. The dielectric constant of graphene is negative. For a side-by-side configuration (Fig. 2.3(b)), the opposite directions of the fields lead to $\Omega_{ij} < 0$. For a top-bottom configuration, the aligned fields lead to $\Omega_{ij} > 0$.

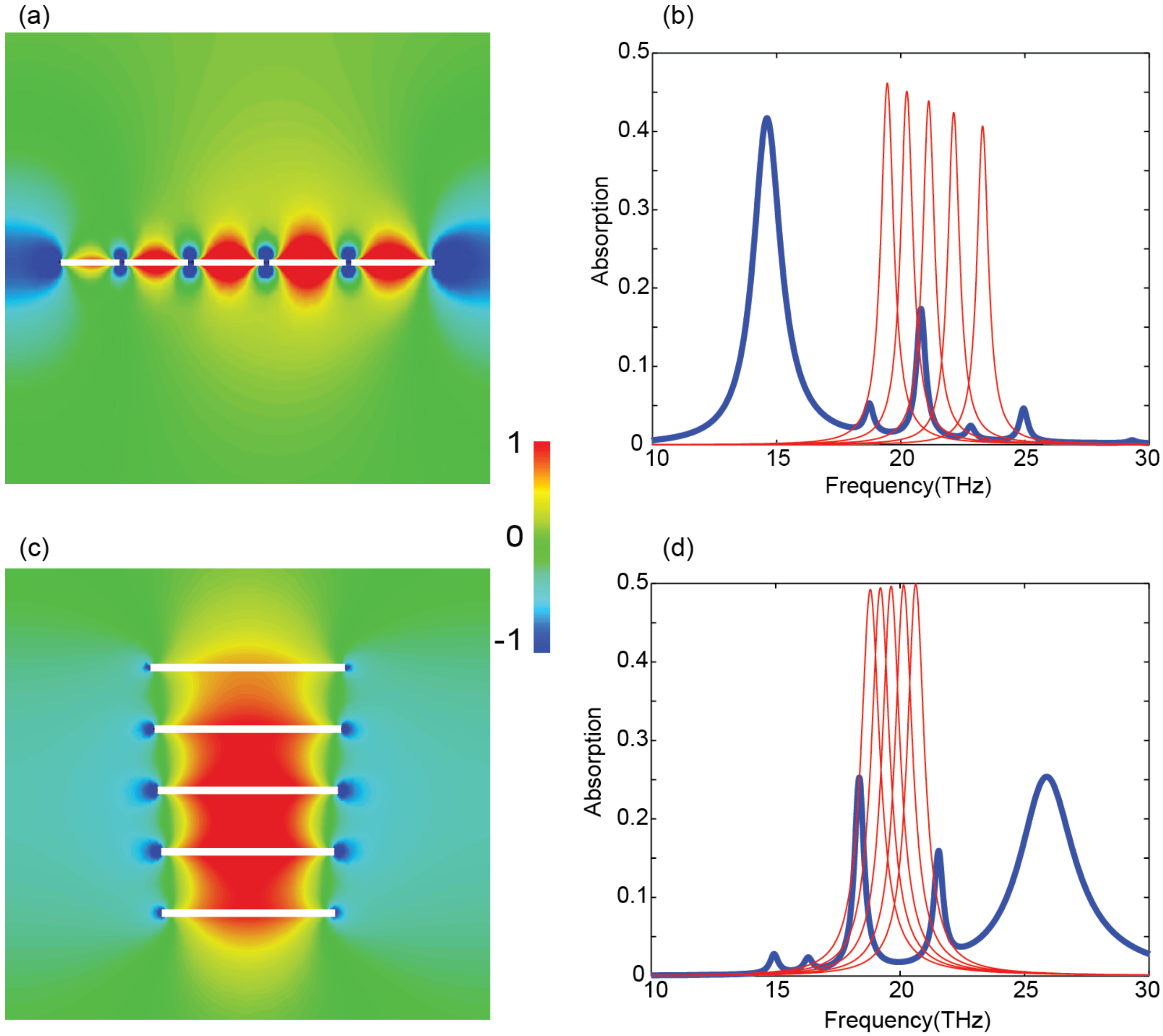

Fig. 2.4. Near-field superradiance. (a) The electric field distribution of the superradiant mode in the side-by-side configuration. Ribbons (white bars) are spaced by 10nm. Their widths are 280nm, 310nm, 340nm, 370nm, and 400nm from the left to the right. (b) The superradiant mode has the lowest frequency (blue line). (c) The superradiant mode of 5 ribbons with widths 400nm, 385nm,

370nm, 355nm, and 340nm from the top to the bottom. The spacing is 130nm. (d) The superradiant mode has the highest frequency (blue line). The size of simulation domains for a) and c) are $2.24\mu m$ and $1.5\mu m$, respectively. The collision frequency is $2.5 \times 10^{12} s^{-1}$. Red lines in b) and d) are the absorption spectra of individual ribbons when they are alone.

To highlight the near-field effect in the simulation, we detune the resonant frequencies of N ribbons. The detuning suppresses the far-field interaction. But the near-field interactions are made strong enough to survive the detuning and become the main mechanism responsible for the superradiance. For 5 ribbons in a side-by-side configuration, all $\Omega_{ij} < 0$. The superradiant mode creates a broad absorption peak (Fig. 2.4(b)) at the lowest frequency with all resonators oscillating in-phase (Fig. 2.4(a)). It also has a much broader bandwidth compared to those of individual resonators alone (red lines Fig. 2.4(b)). The bandwidth broadening is a direct consequence of the enhanced superradiant coupling.

In contrast, for 5 ribbons in a top-bottom configuration (Fig. 2.4(c)), all $\Omega_{ij} > 0$. The superradiant mode (Fig. 2.4(c)) creates a broad absorption peak at the highest frequency (Fig. 2.4(d)), again featuring broadened bandwidth. When the near-field interactions are not properly managed with mixed signs such as the case shown in Fig. 2.5(b), there is no superradiant mode (Fig. 2.5(a)). None of the resonant modes (Fig. 2.5(c)-(g)) shows the in-phase oscillation.

Similar to the far-field case, the near-field superradiance has the same effect on light absorption. Unlike the far-field superradiance, the coupling rate typically increases by less than N times. To show this, we first note that the total coupling rates of all resonators are conserved despite the hybridization of resonators due to near-field interactions. Without near-field interactions, the total coupling rates to each channel are given by the diagonal elements of the matrix DD^T. With near-field interactions, the new coupling rates of the hybridized eigenstates are $D' = DU^{-1}$. The total coupling rates remain the same $D'D'^T = DD^T$. The near-field interaction only redistributes coupling rates among resonances.

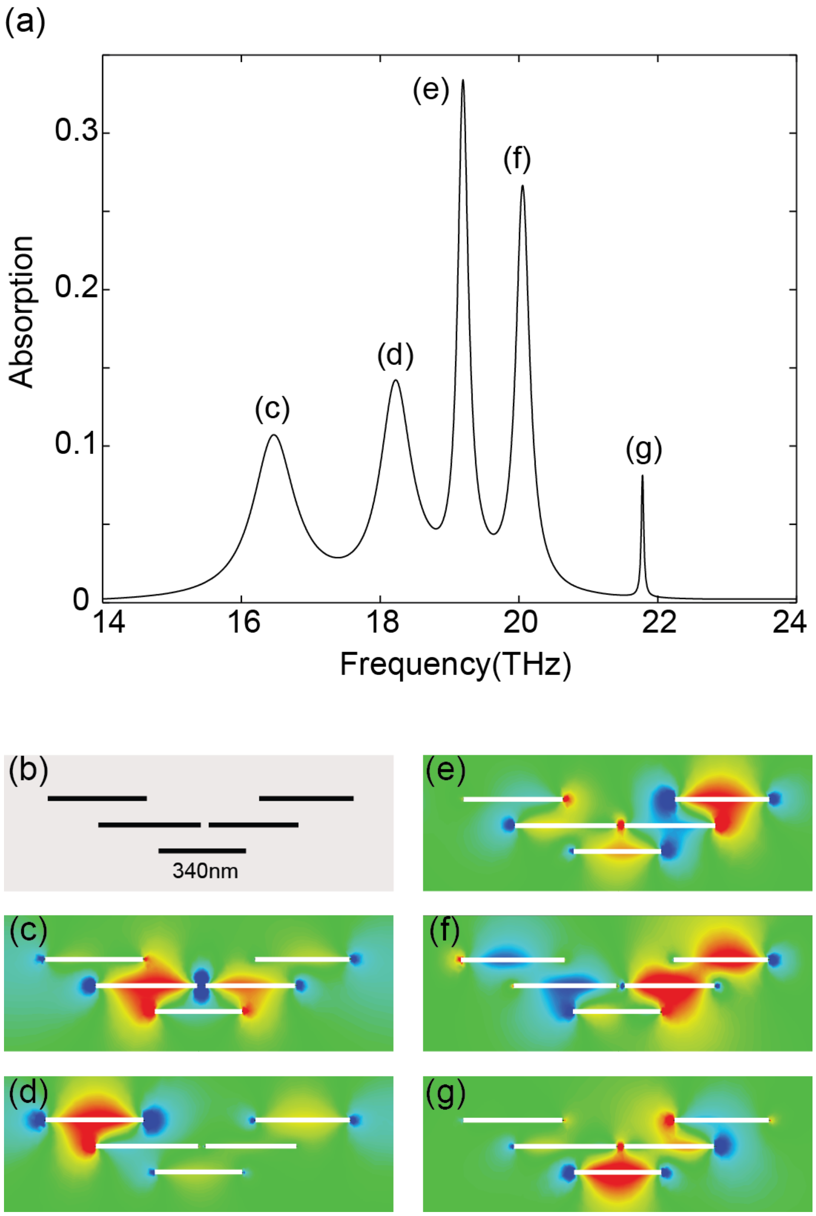

Fig. 2.5. (a) No superradiant mode in five ribbons arranged with mixed positive and negative near-field interactions. (b) The schematic of the structure. (c)-(g) The electric field distributions of resonances, showing no in-phase oscillation. The collision frequency is $2.5 \times 10^{11}\ s^{-1}$.

The superradiant mode has to enhance its coupling at the expense of decreased coupling for other modes. In the far-field case, the superradiant mode is the only mode coupling to the free space and thus takes the entire coupling rate, leading to a N-fold enhancement. For the near-field case, other modes are typically not completely dark and the coupling rate of the superradiant mode normally does not increase by N times.

2.5 Conclusion

As the final remark, we discuss some potential applications of superradiance in solar cells and photodetectors. Most subwavelength nanoresonators have very weak coupling to the free space because of their extremely small sizes. The imbalance of the absorption and the coupling rates leads to overall weak absorption, which limits the performance of the conversion from photons to charge carriers. The enhanced coupling rate in superradiance could allow nanoresonators to operate closer to the critical-coupling condition, where the absorption and coupling rates are balanced and the absorption reaches 100%. For example, graphene is a highly absorptive material. But one still need to rely on optical resonances in order to achieve 100% absorption in a single layer. For this purpose, the coupling rate of graphene resonators needs to be greatly enhanced to match the strong absorption rate. A recent proposal [20] showed the enhancement of coupling through careful material choices, such as a low-index substrate (n = 1.45) and a high doping level 0.4eV. These choices turn out to be experimentally difficult, particularly for the mid-infrared spectral range where low-index transparent materials are rare. Alternatively, we could use superradiance to enhance the coupling rate. The challenging material requirement can be relaxed. For instance, Fig. 2.6 shows the perfect absorption with the superradiance of 4 graphene ribbons doped only at 0.2 eV on high-index Si substrate. It makes it easier to realize in experiment because of easy fabrication and excellent infrared transparency.

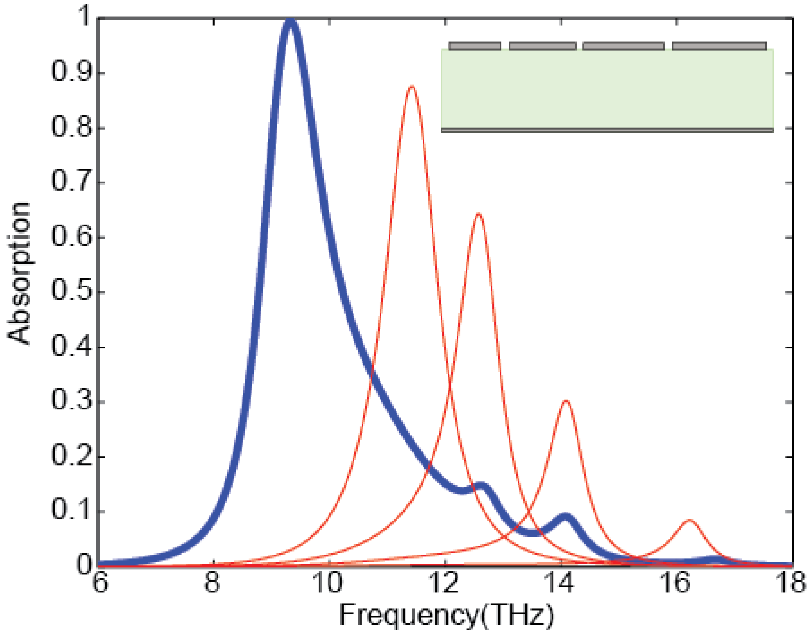

Fig. 2.6. Perfect absorption achieved by the superradiance of 4 graphene ribbons. The graphene ribbons are doped at low level of 0.2 eV and sit on a 2 μm thick Si (n=3.42) substrate, which is easy to fabricate and offers excellent infrared transparency. The widths of ribbons are 45 nm, 60 nm, 75 nm, and 90 nm with 5 nm spacing. The periodicity is 315 nm. The substrate is on a reflecting mirror. Graphene is doped at 0.2eV with $\omega_p = 1.62 \times 10^{15}\ rad/s$, and collision frequency $\gamma = 4.5 \times 10^{12}\ s^{-1}$. The superradiance creates an absorption peak with 100% absorption. Moreover, the peak has enhanced bandwidth compared to individual ribbons alone (red lines Fig. 2.6).

References

[1] R. H. Dicke, Phys. Rev. **93**, 99 (1953).

[2] S. Zhang, D. a. Genov, Y. Wang, M. Liu, and X. Zhang, Phys. Rev. Lett. **101**, 047401 (2008).

[3] B. Luk'yanchuk, N. I. Zheludev, S. a Maier, N. J. Halas, P. Nordlander, H. Giessen, and C. T. Chong, Nat. Mater. **9**, 707 (2010).

[4] Q. Xu, S. Sandhu, M. Povinelli, J. Shakya, S. Fan, and M. Lipson, Phys. Rev. Lett. **96**, 123901 (2006).

[5] M. Yanik, W. Suh, Z. Wang, and S. Fan, Phys. Rev. Lett. **93**, 233903 (2004).

[6] L. Maleki, a B. Matsko, a a Savchenkov, and V. S. Ilchenko, Opt. Lett. **29**, 626 (2004).

[7] D. Smith, H. Chang, K. Fuller, a. Rosenberger, and R. Boyd, Phys. Rev. A **69**, 063804 (2004).

[8] M. Fleischhauer and J. P. Marangos, Rev. Mod. Phys. **77**, 633 (2005).

[9] A. E. Miroshnichenko, S. Flach, and Y. S. Kivshar, Rev. Mod. Phys. **82**, 2257 (2010).

[10] Q. Xu, P. Dong, and M. Lipson, Nat. Phys. **3**, 406 (2007).

[11] C. Wu, A. B. Khanikaev, R. Adato, N. Arju, A. A. Yanik, H. Altug, and G. Shvets, Nat. Mater. **11**, 69 (2012).

[12] K. J. Boller, A. Imamoglu, and S. E. Harris, Phys. Rev. Lett. **66**, 2593 (1991).

[13] U. Fano, Phys. Rev. **124**, 1866 (1961).

[14] J. Pan, S. Sandhu, Y. Huo, N. Stuhrmann, M. L. Povinelli, J. S. Harris, M. M. Fejer, and S. Fan, Phys. Rev. B **81**, 041101 (2010).

[15] P. Lalanne and J. P. Hugonin, Nat. Phys. **2**, 551 (2006).

[16] N. E. Rehler and J. H. Eberly, Phys. Rev. A **3**, 1735 (1971).

[17] L. Ju, B. Geng, J. Horng, C. Girit, M. Martin, Z. Hao, H. a Bechtel, X. Liang, A. Zettl, Y. R. Shen, and F. Wang, Nat. Nanotechnol. **6**, 630 (2011).

[18] M. Jablan, H. Buljan, and M. Soljačić, Phys. Rev. B **80**, 245435 (2009).

[19] H. Yan, X. Li, B. Chandra, G. Tulevski, Y. Wu, M. Freitag, W. Zhu, P. Avouris, and F. Xia, Nat. Nanotechnol. **7**, 330 (2012).

[20] S. Thongrattanasiri, F. H. L. Koppens, and F. J. García de Abajo, Phys. Rev. Lett. **108**, 047401 (2012).

[21] L. Verslegers, Z. Yu, Z. Ruan, P. B. Catrysse, and S. Fan, Phys. Rev. Lett. **108**, 083902 (2012).

[22] Y. Sonnefraud, N. Verellen, H. Sobhani, G. A. E. Vandenbosch, Ḱ. V. V Moshchalkov, P. Van Dorpe, P. Nordlander, and S. A. Maier, ACS Nano **4**, 4 (2010).

[23] P. a. Huidobro, a. Y. Nikitin, C. González-Ballestero, L. Martín-Moreno, and F. J. García-Vidal, Phys. Rev. B **85**, 155438 (2012).

[24] Z. Yu, A. Raman, and S. Fan, Proc. Natl. Acad. Sci. U. S. A. **107**, 17491 (2010).

[25] Z. Yu, A. Raman, and S. Fan, Phys. Rev. Lett. **109**, 173901 (2012).

[26] D. F. Walls and G. J. Milburn, *Quantum Optics* (Springer-Verlag, 1995), p. 121.

[27] H. A. Haus, *Waves and Fields in Optoelectronics* (Prentice-Hall, 1984), p. 212.

[28] W. Suh, Z. Wang, and S. Fan, IEEE J. Quantum Electron. **40**, 1511 (2004).

[29] G. W. Hanson, J. Appl. Phys. **103**, 064302 (2008)

[30] A. Vakil and N. Engheta, Science. **332**, 1291, (2011)

CHAPTER THREE

A MULTIPLE-RESONATOR APPROACH FOR BROADBAND LIGHT ABSORPTION IN A NANOSTRUCTURED GRAPHENE

3.1 Introduction

Emerging two-dimensional (2D) materials such as graphene have promising potentials for optoelectronic applications because of their unique electronic band structures and low dimensionality, which allows ultra-fast injection and extraction of charge carriers, enabling efficient energy conversion between electrons and photons [1-3]. However, their ultrathin feature limits the amount of time for photons interacting with the materials, resulting in an overall weak light-material interaction. For instance, the absorptance of a single layer of graphene is approximately 2.3% [4], which is impressive considering that it is absorbed by a single layer of atoms. But it is still too low to be useful for efficient optoelectronic devices. The light-material interaction must be significantly enhanced in order for 2D materials to achieve device efficiencies that are comparable to those based on conventional thick semiconductors.

Optical resonance has been employed as an effective means for enhancing the light-material interaction in conventional optoelectronic devices. There has been a great amount of recent interest in applying resonant enhancement in 2D materials. Existing methods can be divided into two categories. The first relies on conventional dielectric materials to construct optical resonators, such as Fabry-Perot cavities based on distributed Bragg reflectors [5] and guided resonances in photonic-crystal slabs [6, 7]. These approaches generally require sophisticated nanofabrication. The second category is based on the intrinsic plasmonic resonances. For instance, nanostructured graphene such as nano disks and ribbons support localized plasmonic resonances [8, 9, 10], particularly in the mid and far infrared spectral regimes. Such resonators do not require any additional dielectric material. Moreover, their resonant properties can be easily tuned by changing the geometrical shape. In both methods, 100% light absorption has been shown by operating the resonators at the critical coupling condition [6, 11].

However, there has been one significant challenge existing in both aforementioned methods in that the efficient light absorption can only be achieved in a narrow spectral range, which is limited by the bandwidth of a single type of resonator. For instance, the full width at half maximum (FWHM) of the perfect absorption reported in ref.[11] is only 6% of the resonant frequency. To overcome the bandwidth limitation, we design a multi-resonator approach based on plasmonic resonances of graphene. Compared to their resonant wavelengths, these graphene resonators have extremely small sizes, allowing multiple resonators with different frequencies to be densely packed in space. Each type of resonators is responsible for the enhancement of light-matter interaction in a limited bandwidth. Together, they offer an efficient broadband light absorption in a single layer of graphene. These closely packed deep-subwavelength resonators create an ultrathin medium with a high optical density of states [12-16], which enables broadband light absorption. The broadband absorption demonstrated here is one important step toward efficient 2D-material optoelectronic devices.

3.2 Broadband light absorption based on multiple resonators

Figure 3.1 illustrates the concept of broadband light absorption based on multiple resonators. A large area is covered by arrays of nanoresonators. These nanoresonators could be constructed by for example, a nanodisk of single-layer graphene. We use absorption cross-section σ_a to characterize the absorption of individual nanoresonators.

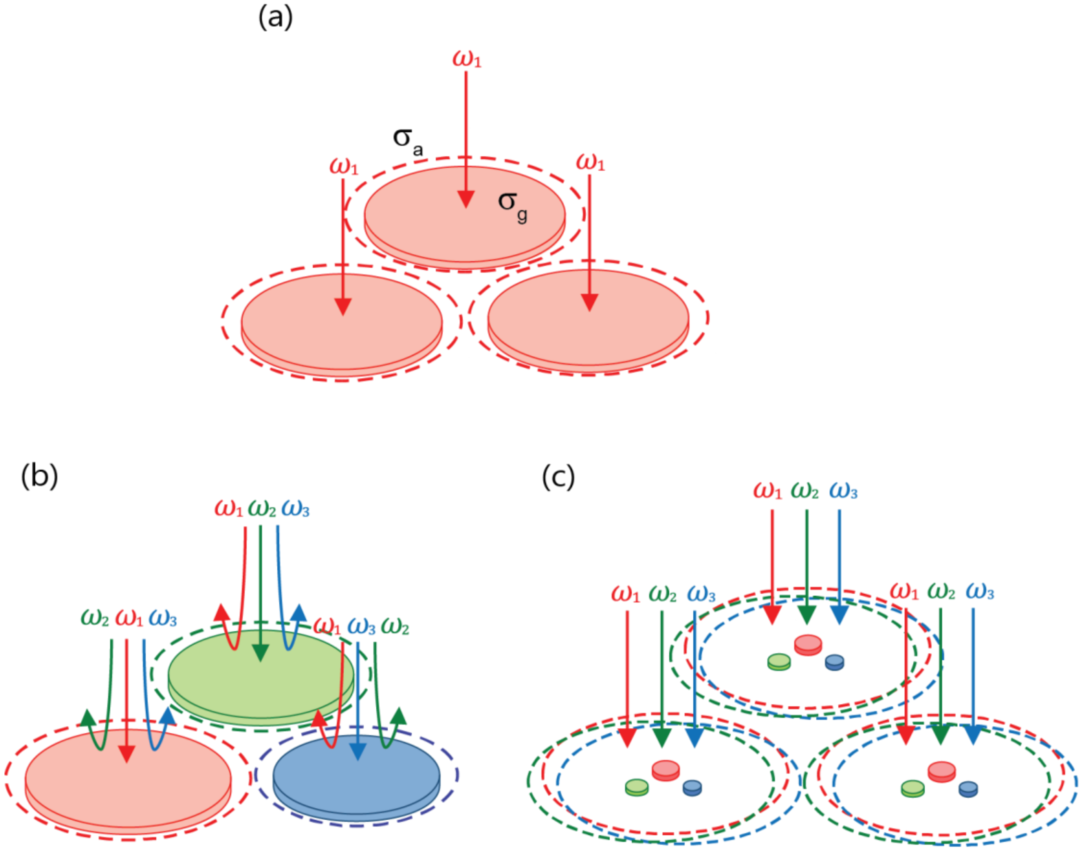

Fig 3.1. Schematic of absorption cross-section (dashed line). Solid color disks represent the geometrical size of the nanoresonators. Colors represent different frequencies. (a) Arrays of a single type of resonator with an absorption cross-section slightly larger than the geometrical size. Since the absorption cross-section can fill the space, efficient large-area absorption can be achieved for a single frequency of ω_1. (b) Arrays of three types of resonators with different resonant frequencies. The absorption is inefficient because the absorption cross-sections of different frequencies cannot cover the entire space. (c) Resonators with much smaller geometrical sizes enable efficient broadband absorption. Due to their small geometrical sizes, resonators can be closely packed so that the absorption cross-sections at different frequencies can all cover the entire space.

σ_a is conceptually illustrated by the dashed circles in Fig. 3.1(a). Light falling within the circle is fully absorbed by the resonator. For efficient absorption over a large area, the dashed circles have to fill the most part of the space as shown in Fig. 3.1(a), which can be achieved if σ_a is larger than the geometrical size σ_g of the resonator. Arrays of the same type of resonators (Fig. 3.1(a)) have been used to achieve efficient absorption with resonators made from high-index semiconductors [17] and single-layer graphene [11]. Since the absorption cross-section decreases significantly away from the resonant frequency, only narrow-band absorption can be achieved in this way.

In order to broaden the spectral bandwidth, one has to rely on multiple resonators with different resonant frequencies [12]. Then a significant challenge arises because of the limited space to accommodate different types of resonators. To illustrate this point, we show three closely packed nanoresonators of different frequencies in Fig. 3.1(b). Their absorption cross-sections are coded with different colors to represent different resonant frequencies. When the geometrical sizes σ_g are only slightly smaller than σ_a, the dashed circle of each color can only fill a subset of the space. Consequently, light absorption becomes less efficient when the bandwidth is broadened by multiple resonators. On the other hand, if σ_g can be significantly smaller than the σ_a as shown in Fig. 3.1(c), one can place resonators closely with each other with their absorption cross-sections overlapping in space. When packed in arrays, dashed circles of each color can fill the space, resulting in efficient absorption in a broader spectral range. Base on this analysis, it is evident that the key to achieve broadband absorption is to realize a large σ_a/σ_g ratio.

To evaluate the ratio σ_a/σ_g, we can use a coupled mode theory [18] to derive the general form as

$$\sigma_a(\omega) = \frac{\lambda^2}{4\pi} \times \frac{\gamma_a \gamma_c}{(\omega - \omega_0)^2 + (\gamma_a + \gamma_c)^2/4} G \qquad (1)$$

where ω_0 is the resonant frequency, λ is the resonant wavelength. γ_a and γ_c are the absorption and the coupling rate, respectively. They characterize the rates of the loss of photons due to intrinsic material absorption (γ_a) and radiation to the free space (γ_c). *G* is the directivity associated with the angular response of the resonator, which is 1 and 3/2 for isotropic and dipolar angular responses, respectively. To maximize σ_a, a resonator must operate at the critical coupling condition, i.e. $\gamma_a = \gamma_c$. In this case, the maximum absorption cross-section of an isotropic resonator (*G* = 1) is

$$\sigma_{a,max} = \frac{\lambda^2}{4\pi} \tag{2}$$

which is obtained at the resonant frequency. Obviously, the maximal σ_a is only determined by wavelength.

On the other hand, the geometrical size σ_g is not necessarily related to σ_a. In most dielectric materials, σ_g scales as λ^2/n^2 where n is the refractive index. Therefore the ratio of σ_a/σ_g is normally not a large number in the visible and infrared spectral ranges. However, in 2D materials that support plasmonic resonances, such as graphene, the geometrical size σ_g can be hundreds times smaller than the wavelength [19], leading to a unique opportunity to achieve a large σ_a/σ_g.

In addition to the requirement of a large ratio σ_a/σ_g, we also need analyze the near-field interaction among closely packed resonators. As we will show later, the near-field interaction introduces spectral competition of absorption cross-sections and often negatively impacts the absorption. The near-field interaction can be minimized by judiciously arranging the spatial configuration of nearby nanoresonators, the details of which will be discussed later.

3.3 Single graphene nanoresonators

Based on the general strategy outlined above, we now demonstrate a specific example based on graphene nanoresonators. Localized plasmonic resonances in graphene nanostructures exhibit extremely strong light confinement. The sizes of nanoresonators are often hundreds times smaller than the free-space wavelength [20]. Since σ_a is determined by the free-space wavelength, $\sigma_a/\sigma_g \gg 1$ can be realized.

We first calculate σ_a/σ_g of graphene nanoresonators by solving the full-wave Maxwell's equations numerically. We use a resonator with a square shape as shown in the inset of Fig. 3.2(a). It is placed on a perfect mirror with a dielectric spacer, which has a dielectric constant $\varepsilon = 2.1$ and a thickness t = 1.6 μm. Optical properties of graphene are modeled by the complex permittivity [21]

$$\varepsilon(\omega) = 1 + i\frac{\eta_s}{\varepsilon_0 \omega \Delta} \tag{3}$$

where $\Delta = 1$ nm is assumed for the thickness of graphene and η_s is the surface conductivity [22] given by

$$\eta_s = \frac{2e^2 k_B T}{\pi \hbar^2} \ln\left(2\cosh\frac{E_F}{2k_B T}\right)\frac{i}{\omega + i\tau^{-1}} \tag{4}$$

with E_F being the chemical potential and τ the relaxation time. Here, only the intraband transition is considered and the interband transition is neglected because $\hbar\omega \ll E_F$ is satisfied in the frequency range of interest. The size of the graphene resonator is 100 nm × 100 nm and the doping level of graphene is assumed to be $E_F = 0.6$ eV.

The simulated absorption cross-section is shown in Fig. 3.2(a). The coupled mode theory shown in Eq. 1 agrees extremely well with the simulation result. The coupling and absorption rates can easily be extracted from the fitted curve (solid line in Fig. 3.2(a)). Most importantly, the resonant absorption cross-section of 5.2×10^5 nm^2 is more than 50 times larger than the geometrical size of 10^4 nm^2. Such a large ratio is not a result of any special choices of the shape or the size. In fact, the ratio stays around 40 for square sizes ranging from 50 nm to 100 nm (Fig. 3.2(b)).

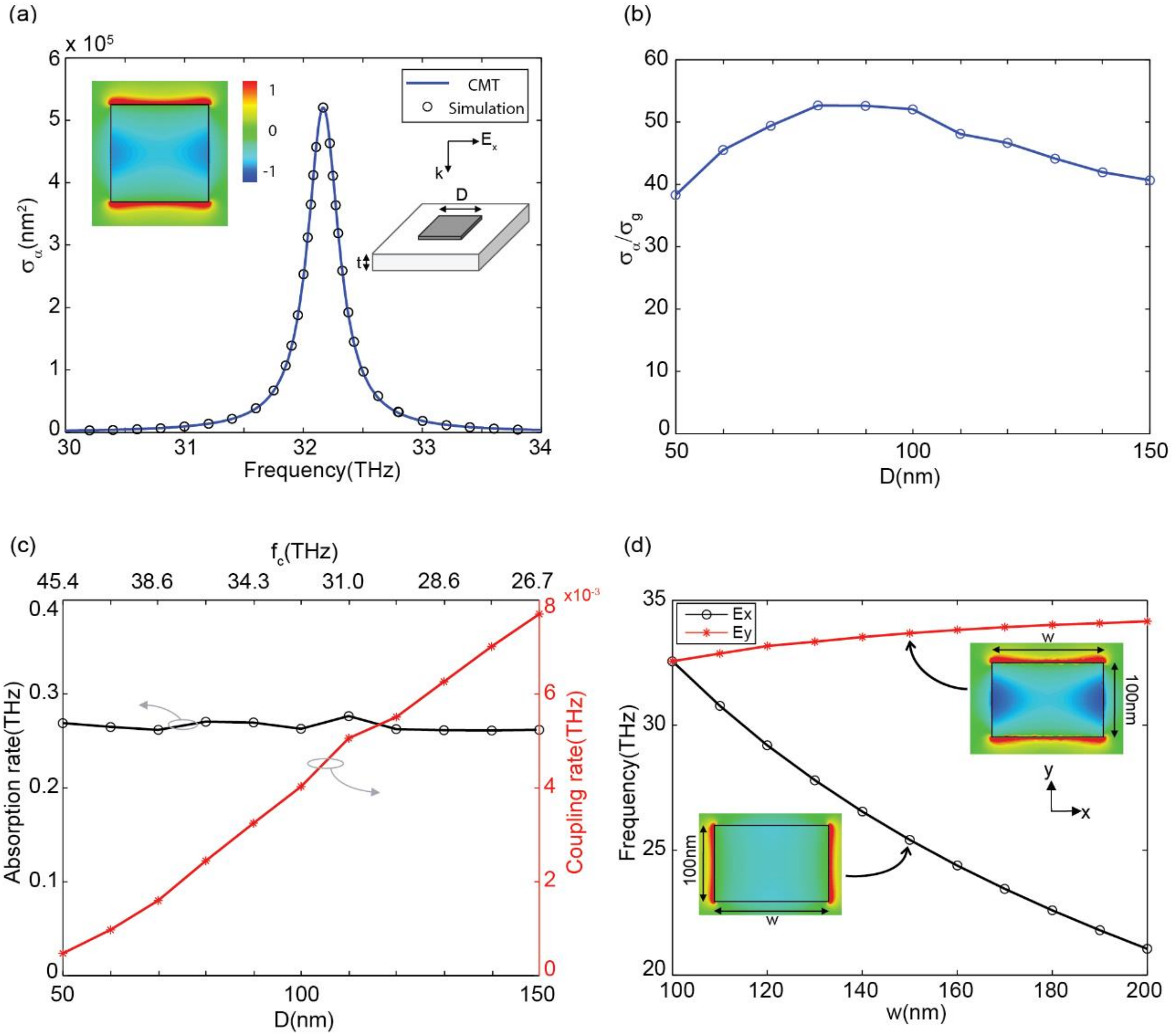

Fig. 3.2. (a) Absorption cross-section of a square graphene resonator with a size D = 100 nm. Dielectric constant of substrate is 2.1 and the thickness t = 1.6 μm. The simulation is performed with a periodic boundary condition with a very large period. The inset is the field distribution at the resonant frequency. Open circles are simulation and the solid line is coupled mode theory. (b) Ratio between the absorption cross-section (σ_a) and the geometric cross-section (σ_g) for different

dimensions of graphene *D*. (c) Absorption rate and coupling rate as a function of graphene dimension *D*. (d) Resonant frequency shift with respect to graphene dimension. One side is fixed to 100nm, the other side *w* is varied from 100 nm to 200 nm. $E_{x(y)}$ represents the incident light in the *x* (*y*) polarization state.

It is very difficult to achieve such a large ratio in conventional dielectric materials. For most dielectric materials, such as Si and Ge, σ_a is only slightly larger than σ_g[13]. Even though $\sigma_a > 40\,\sigma_g$, σ_a still does not reach the upper bound $\sigma_{a,max}$ in Eq (2). For a resonant wavelength of 9.32 μm, the calculated $\sigma_{a,max}$ is approximately 6.91 μm^2, which is about 691 times of the geometrical size. The reason that this resonator does not reach the upper bound is because it operates in the under-coupling condition with $\gamma_c \ll \gamma_a$. Fig. 3.2(c) shows the fitted absorption and coupling rates of these nanoresonators. It can be seen that $\gamma_c \leq 0.03\gamma_a$. When the size increases, the coupling rate increases while the absorption rate remains about the same. To operate closer to the critical coupling condition, one could decrease the absorption rate by increasing the mobility of carriers in graphene.

To take advantage of the large ratio of σ_a/σ_g, we need a set of resonators of different frequencies, which can be easily achieved by tuning the shape of nanostructures. A graphene square supports two degenerate states that can be excited by x- or y- linearly polarized light. The degeneracy is lifted when one side of the square increases as shown in Fig. 3.2(d). The x-polarized resonance shows a red shift as the size increases because the length of the x-direction dipole increases (lower inset of Fig. 3.2(d)). To the contrary, the y-polarized resonance undergoes a blue shift. Since the length of the resonator in y-direction is fixed, changing length in x-direction does not affect the spatial length of the dipolar resonance (upper inset of Fig. 3.2(d)). Instead, this blue shift could be understood using a perturbation theory. The dielectric constant of graphene is negative in the mid-infrared spectral range. According to the perturbation theory [23], the presence of materials with negative dielectric constant increases the resonant frequencies.

3.4 Array of multiple graphene nanoresonators

So far, we have focused on the properties of individual nanoresonators. To obtain large-area light absorption, we need to use periodic arrays of graphene resonators. First, we discuss arrays that consist of a single type of resonator, which has been investigated in many previous works [11, 24, 25]. In contrast to these works, our focus here is to interpret the absorption based on the absorption cross-section.

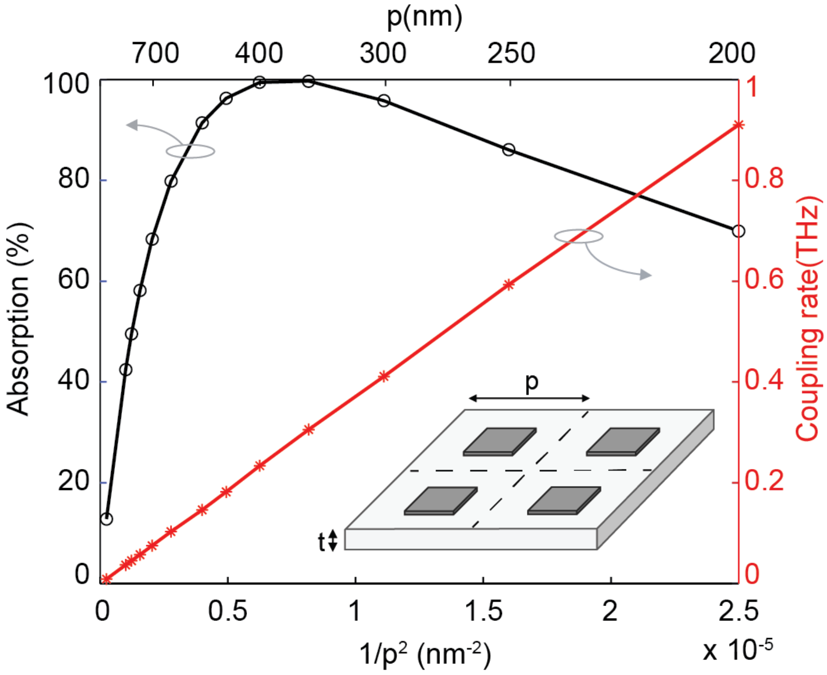

Fig. 3.3. Linear relationship between coupling rate and 1/p^2 (red star). Period-dependent absorption (black circle) for arrays of graphene squares. The dimension of the square is 100 nm x 100 nm.

First, we show how the density of the nanoresonator affect the total large-area absorption by using an example of periodic arrays. The period p dictates the spatial density of resonators and thus how the absorption cross-sections fill the space. Fig. 3.3 shows the simulated absorption of arrays of graphene squares. For very large periods, the absorption cross-sections (See dashed circles in Fig. 3.1) cannot fill the entire space and the large-area absorption is well below 100%. When p decreases, the large-area absorption increases because the absorption cross-sections can fill more of the space. 100% absorption is achieved when p is around 400 nm. It is interesting to note that the absorption does not increase monotonically with a decreasing p. We can use the coupled mode theory to understand such trend. Because of the presence of a back mirror and a period that is smaller than the wavelength, these resonators only radiate light into one direction [26]. As a result, one can calculate the large-area absorption as [6]

$$A = \frac{\gamma_c \gamma_a}{(\omega - \omega_0)^2 + (\gamma_c + \gamma_a)^2/4} \tag{5}$$

The absorption rate γ_a is again independent of the period and the shape of the resonator. On the other hand, the coupling rate γ_c scales linearly with $1/p^2$ as shown by the red line in Fig. 3.3. When the $\gamma_c = \gamma_a$ at p ~ 400 nm, the critical coupling condition is satisfied and A = 100%. Further reducing the period increases γ_c and the resonator arrays enter the over-coupling condition $\gamma_c \geq \gamma_a$. The absorption then starts to decrease. The above analysis shows that overcrowded resonators in space actually reduces large-area absorption. This observation connects well with the effect of spectral competition to be discussed below

For broadband absorption, we place multiple resonators of different frequencies in the unit cell. Ideally, each type of resonators can still absorb the same amount of light as the case when they are not placed together. However, the near-field interaction results in undesirable spectral competition. To quantify such competition, we define the spectral cross-section [14]

$$\rho = \int_0^\infty A(\omega)d\omega \tag{6}$$

It measures the total broadband absorption. Similar to the absorption cross-section σ_a, ρ has an upper limit that is determined by the number of types of resonator [14]. We next use a specific example to illustrate the result of the spectral competition. We consider two types of resonators, A and B as shown in the inset of Fig. 3.4(a). Both are 100 nm long. Resonator A and B are 60 nm and 50 nm wide, respectively. The period is fixed at 850 nm. When the unit cell only has the A-type resonator, the absorption spectrum is shown by star markers (red) in Fig. 3.4(a). The case for B-type is shown by the circular markers (black). $\rho_{A(B)}$ can be easily calculated to measure the broadband absorption.

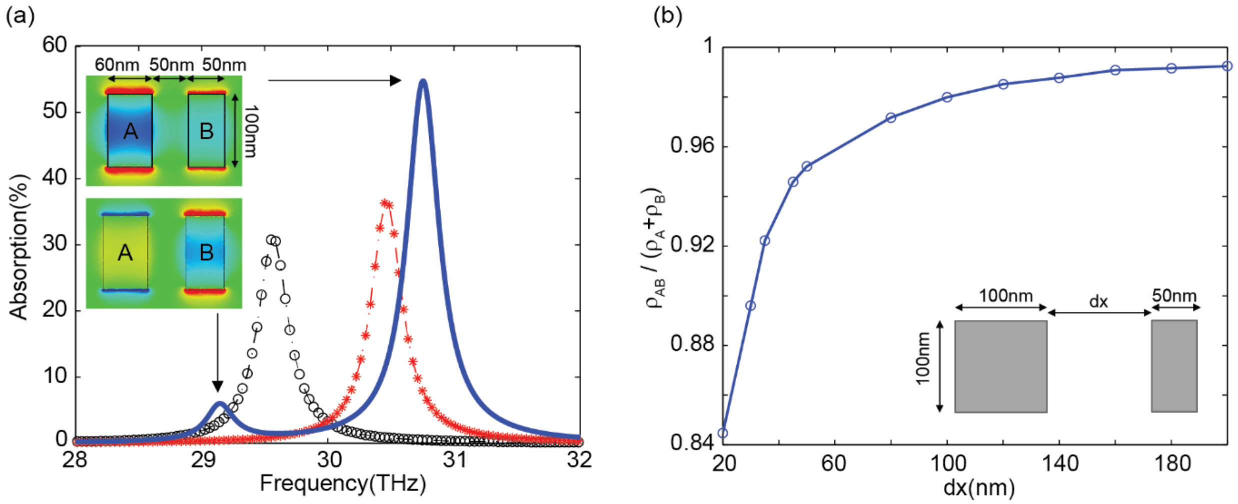

Fig. 3.4. (a) Absorption spectra for periodic arrays with only A-type resonator (stars), with only B-type resonator (circles), and with both A- and B-type resonators (solid line). Dot-dashed curves are based on coupled mode theory. (b) Ratio between total spectral cross-section (ρ_{AB}) and the upper bound of spectral cross-section ($\rho_A + \rho_B$) as the distance between two resonators *dx* increases from 20 nm to 200 nm.

Now, we place both A- and B-type resonators together in the unit cell with a spacing of d = 50 nm between them. The absorption spectrum is shown by the solid blue line in Fig. 3.4(a). The spectral cross-section ρ_{AB} can also be calculated. It turns out that

$$\rho_{AB} \leq \rho_{\mathrm{A}} + \rho_{B} \tag{7}$$

because of the coupling between the two resonators. The coupling can be visualized by the field distribution at the two resonant peaks where the fields spread over two squares at both resonant frequencies (insets in Fig. 3.4(a)). These two nanoresonators compete for the absorption, resulting in a total spectral cross-section ρ_{AB} that is smaller than the linear addition of ρ_{A} and ρ_{B}. The ratio $\rho_{\mathrm{AB}}/(\rho_{\mathrm{A}} + \rho_{B})$ can be used to evaluate the spectral competition for different spatial configurations of the resonators. For example, Fig. 3.4(b) shows the ratio as a function of the spacing. It decreases when the spacing reduces, indicating greater spectral competition and more penalty in absorption. For large spacing, ρ_{AB} increases and the $\rho_{\mathrm{AB}}/(\rho_{\mathrm{A}} + \rho_{B})$ approaches 1. However, using large spacing to improve light absorption is a waste of the precious empty space between those resonators. These empty spaces are afforded by the deep sub-wavelength-sized resonators and should be used to fill more resonators with different frequencies to broaden the absorption bandwidth.

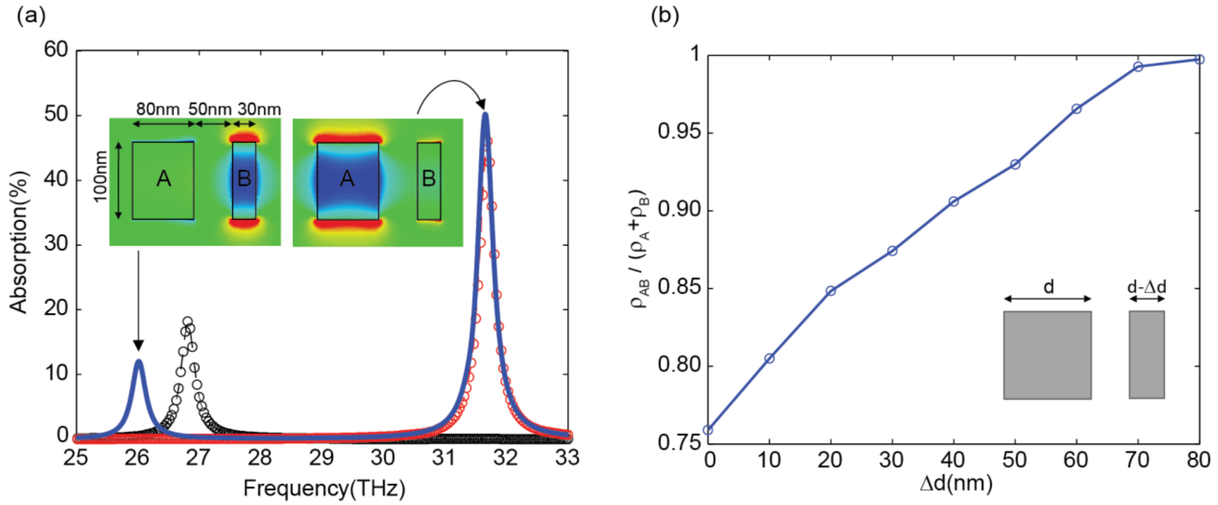

Fig. 3.5. (a) Absorption spectra for periodic arrays with only A-type resonator (red circles), with only B-type resonator (black circles), and with both A- and B-type resonators (solid line). Dashed curves are based on coupled mode theory. (b) Ratio between total spectral cross-section (ρ_{AB}) and the upper bound of spectral cross-section ($\rho_A + \rho_B$) as Δd varies from 0 nm to 80 nm. Distance between two graphene resonators is 50 nm.

To overcome this challenge, we use frequency detuning to suppress the spectral competition when the inter-resonant distance is small. As described in the perturbation theory [27], the effect of the coupling between resonant modes decreases when the difference between two resonant frequencies increases. To illustrate this point, we consider two graphene nanoresonators with quite different sizes. They are closely spaced in space, but their resonant frequencies are well separated. The spectral competition can be kept minimal. As shown in Fig. 3.5(a), the absorption spectrum (solid line) for the array consisting of both resonators is very close to the linear summation of the spectra of arrays that only consist of individual resonators (markers). The field distributions (inset of Fig. 3.5(a)) at the two absorption peaks (blue line) also indicate that the nature of the resonances is dominated by that of individual resonators despite a small spacing of 50 nm. Fig. 3.5(b) shows the ratio $\rho_{AB}/(\rho_A + \rho_B)$ as a function of the frequency detuning. The spacing is fixed at 50 nm. When the width difference between the two structures $\Delta d = 0$, two resonators are identical. There is significant spectral competition and $\rho_{AB}/(\rho_A + \rho_B) = 0.76$**.** When Δd increases, the frequency detuning increases and $\rho_{AB}/(\rho_A + \rho_B)$ approaches 1. Fig. 3.5(b) shows that the general strategy of optimal spatial configuration is to place resonators of large frequency detuning closer and to keep resonators with similar frequencies far away.

3.5 Broadband absorption

Following the strategy outlined above, we next show an example of broadband absorption in a single layer of graphene. The unit cell has 29 graphene resonators (Fig. 3.6(a)) and the period is 850 nm. The sizes of these resonators are all deep sub-wavelength. There are 15 different types of resonators. The substrate is the same as used in Fig. 3.1. In particular, we place graphene resonators of similar sizes sparsely and resonators of different sizes closely. This arrangement is to reduce the spectral competition. Fig. 3.6(b) shows the absorption spectrum, which exhibits broadband absorption spanning from 24 THz to 33 THz. The relative bandwidth $\Delta\omega/\omega_0$ is about 29%, where the central frequency $\omega_0 = 28.5$ THz. It consists of 17 resonant peaks, a number close to the number of types of the resonators.

For comparison purpose, the dashed line in Fig. 3.6(b) shows the absorption of optimized arrays of a single type of resonators. The bandwidth is rather limited. In contrast, the multiple resonators approach significantly broadens the bandwidth.

The total spectral absorption cross-section is enhanced by 4.6 times compared to the single resonator case. Here, we use a relatively high mobility for graphene $\mu = 10{,}000\ \mathrm{cm^2V^{-1}s^{-1}}$. Higher mobility generally increases the light absorption because resonators can operate closer to the critical coupling condition. For experimental realization with graphene synthesized by chemical vapor deposition, the mobility is generally lower. The broadband absorption enhancement can still be observed even when the mobility is only 1,000 cm^{2}V^{-1}s^{-1}. The absorption spectrum is shown by solid curve (green) in Fig. 3.6(b).

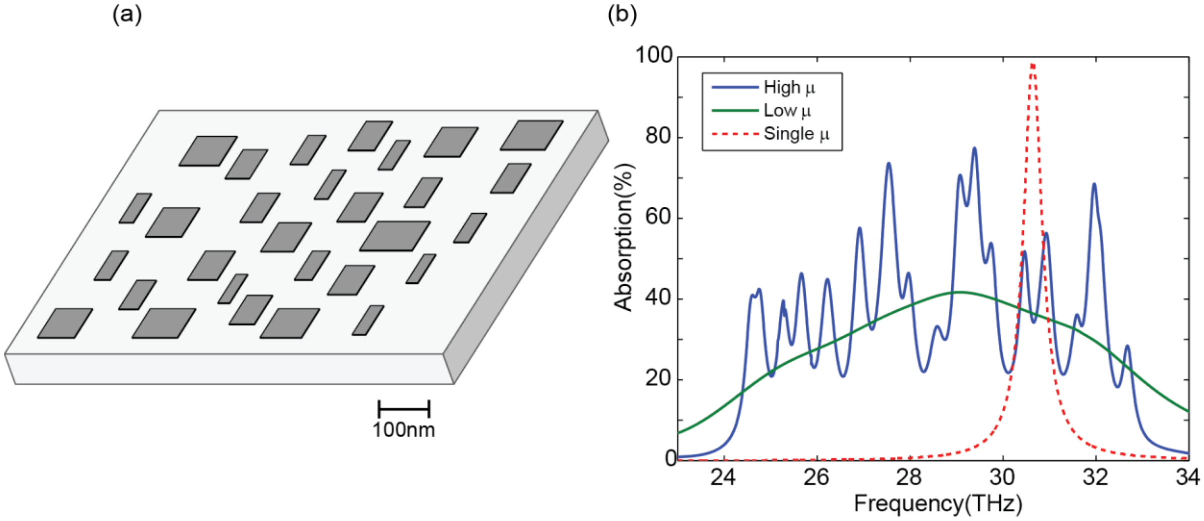

Fig. 3.6. (a) Layout of a broadband light absorber based on multiple graphene resonators. Period is 850nm, dielectric constant of the substrate is 2.1 and the thickness is 1.6 μm. (b) Absorption spectra of broadband light absorber in Fig. 3.6(a) with a mobility of 10,000 cm^{2}V^{-1}s^{-1} (high μ) and 1,000 cm^{2}V^{-1}s^{-1} (low μ). In comparison, dashed line shows the absorption by optimized arrays of single-type graphene resonator with limited bandwidth. A mobility of 10,000 cm^{2}V^{-1}s^{-1} is used.

3.6 Conclusion

In conclusion, we show a design based on multiple graphene nanoresonator to achieve broadband light absorption. There are two key factors. First, the absorption cross-section needs to be significantly larger than the geometrical size of the nanoresonators. This requirement ensures that many resonators can be packed together such that their absorption cross-sections at different frequencies can all fill the space. Graphene nanoresonators are particularly attractive in that the sizes of graphene resonators can be in the deep sub-wavelength regime with a very high ratio between the absorption cross-section and the geometrical size. Second, we need to arrange the spatial configuration of resonators to suppress spectral competition. For this purpose, a resonator should be neighbored by resonators with different frequencies. Again, graphene nanoresonators afford great tunability through changing the geometrical size. By fulfilling these two requirements, we show one example of broadband graphene absorber with an averaged absorption above 20% with a relative bandwidth of 29%, significantly higher than that of arrays of a single type of resonators. This method can also be applied to other deep sub-wavelength nanoresonators to enhance broadband light-matter interaction in ultrathin materials.

References

[1] K. S. Novoselov *et al.*, “Electric Field Effect in Atomically Thin Carbon Films,” *Science*, vol. 306, no. 5696, pp. 666–669, Oct. 2004.

[2] S. Thongrattanasiri, F. H. L. Koppens, and F. J. García de Abajo, “Complete Optical Absorption in Periodically Patterned Graphene,” *Phys. Rev. Lett.*, vol. 108, no. 4, p. 047401, Jan. 2012.

[3] Y. Liu *et al.*, “Approaching total absorption at near infrared in a large area monolayer graphene by critical coupling,” *Appl. Phys. Lett.*, vol. 105, no. 18, p. 181105, Nov. 2014.

[4] J. R. Piper and S. Fan, “Total Absorption in a Graphene Monolayer in the Optical Regime by Critical Coupling with a Photonic Crystal Guided Resonance,” *ACS Photonics*, vol. 1, no. 4, pp. 347–353, Apr. 2014.

[5] K. F. Mak, M. Y. Sfeir, Y. Wu, C. H. Lui, J. A. Misewich, and T. F. Heinz, “Measurement of the Optical Conductivity of Graphene,” *Phys. Rev. Lett.*, vol. 101, no. 19, p. 196405, Nov. 2008.

[6] M. Furchi *et al.*, “Microcavity-Integrated Graphene Photodetector,” *Nano Lett.*, vol. 12, no. 6, pp. 2773–2777, Jun. 2012.

[7] F. H. L. Koppens, D. E. Chang, and F. J. García de Abajo, “Graphene Plasmonics: A Platform for Strong Light–Matter Interactions,” *Nano Lett.*, vol. 11, no. 8, pp. 3370–3377, Aug. 2011.

[8] L. Cao *et al.*, “Semiconductor Nanowire Optical Antenna Solar Absorbers,” *Nano Lett.*, vol. 10, no. 2, pp. 439–445, Feb. 2010.

[9] Z. Yu, A. Raman, and S. Fan, “Fundamental limit of nanophotonic light trapping in solar cells,” *Proc. Natl. Acad. Sci.*, vol. 107, no. 41, pp. 17491–17496, Oct. 2010.

[10] Z. Fang *et al.*, “Gated tunability and hybridization of localized plasmons in nanostructured graphene,” *ACS Nano*, vol. 7, no. 3, pp. 2388–2395, Mar. 2013.

[11] A. Vakil and N. Engheta, “Transformation Optics Using Graphene,” *Science*, vol. 332, no. 6035, pp. 1291–1294, Jun. 2011.

[12] G. W. Hanson, “Dyadic Green’s functions and guided surface waves for a surface conductivity model of graphene,” *J. Appl. Phys.*, vol. 103, no. 6, p. 064302, Mar. 2008.

[13] S. Yi, M. Zhou, Z. Wang, and Z. Yu, “Superradiant absorption in multiple optical nanoresonators,” *Phys. Rev. B*, vol. 89, no. 19, p. 195449, May 2014.

[14] S. Thongrattanasiri and F. J. García de Abajo, “Optical field enhancement by strong plasmon interaction in graphene nanostructures,” *Phys. Rev. Lett.*, vol. 110, no. 18, p. 187401, May 2013.

[15] Z. Fang *et al.*, “Active Tunable Absorption Enhancement with Graphene Nanodisk Arrays,” *Nano Lett.*, vol. 14, no. 1, pp. 299–304, Jan. 2014.

[16] Z. Yu, A. Raman, and S. Fan, “Fundamental limit of light trapping in grating structures,” *Opt. Express*, vol. 18, no. 103, pp. A366–A380, Sep. 2010.

[17] F. Bonaccorso, Z. Sun, T. Hasan, and A. C. Ferrari, “Graphene photonics and optoelectronics,” *Nat. Photonics*, vol. 4, no. 9, pp. 611–622, Sep. 2010.

[18] K. I. Bolotin *et al.*, “Ultrahigh electron mobility in suspended graphene,” *Solid State Commun.*, vol. 146, no. 9, pp. 351–355, Jun. 2008.

[19] D. M. Callahan, J. N. Munday, and H. A. Atwater, “Solar Cell Light Trapping beyond the Ray Optic Limit,” *Nano Lett.*, vol. 12, no. 1, pp. 214–218, Jan. 2012.

[20] K. Aydin, V. E. Ferry, R. M. Briggs, and H. A. Atwater, “Broadband polarization-independent resonant light absorption using ultrathin plasmonic super absorbers,” *Nat. Commun.*, vol. 2, p. 517, Nov. 2011.

[21] Y. Cui *et al.*, “Ultrabroadband Light Absorption by a Sawtooth Anisotropic Metamaterial Slab,” *Nano Lett.*, vol. 12, no. 3, pp. 1443–1447, Mar. 2012.

[22] H. Hu, D. Ji, X. Zeng, K. Liu, and Q. Gan, “Rainbow Trapping in Hyperbolic Metamaterial Waveguide,” *Sci. Rep.*, vol. 3, p. 1249, Feb. 2013.

[23] M. Jablan, H. Buljan, and M. Soljačić, “Plasmonics in graphene at infrared frequencies,” *Phys. Rev. B*, vol. 80, no. 24, p. 245435, Dec. 2009.

[24] J. J. Sakurai, J. J. Napolitano, Modern Quantum Mechanics, 2nd Edition (Addison-Wesley, 2010).

[25] L. Verslegers, Z. Yu, P. B. Catrysse, and S. Fan, “Temporal coupled-mode theory for resonant apertures,” *JOSA B*, vol. 27, no. 10, pp. 1947–1956, Oct. 2010.

[26] H. Yan *et al.*, “Tunable infrared plasmonic devices using graphene/insulator stacks,” *Nat. Nanotechnol.*, vol. 7, no. 5, pp. 330–334, May 2012.

[27] S. Zhang, D. A. Genov, Y. Wang, M. Liu, and X. Zhang, “Plasmon-Induced Transparency in Metamaterials,” *Phys. Rev. Lett.*, vol. 101, no. 4, p. 047401, Jul. 2008.

CHAPTER FOUR

SUBWAVELENGTH ANGLE-SENSING PHOTODETECTORS INSPIRED BY INTERNALLY COUPLED EARS IN SMALL ANIMALS

4.1 Introduction

Imaging chips are constructed from a large array of photo-detecting pixels. Conventional pixels only detect the intensity of light and are incapable of acquiring other important information, such as the incident angle of the light. While the intensity information alone is sufficient for traditional applications, such as photography, its limitation becomes apparent in advanced imaging tasks. For example, a single image of the intensity cannot reveal depth-information of objects in a scene, which requires directional information. Another example is the light field camera, which uses information from incident angles to refocus even after the image is taken [1-2]. To measure the incident angle, one has resorted to discrete optical components such as lenses or gratings together with photo-detecting pixels. These components are expensive to integrate and degrade the resolution. Only recently, have researchers been able to successfully integrate angle-sensitive pixels (ASPs) into a CMOS architecture [3-4]. Their minimum size has been on the order of several microns as their operation relies on the use of gratings. With current scaling trends for imaging systems, the size of pixels is rapidly approaching the optical wavelength λ_0. This poses a seemingly unsurpassable challenge towards angle detection. Existing methods based on micro-lenses or gratings cannot be miniaturized indefinitely because diffraction effects will result in a decrease in the accuracy of the angular measurement. Figure 4.1(a) illustrates this point for a system that uses a lens to measure the incident angle by focusing light of different directions to distinct spatial locations. The measurement accuracy is reduced by the diffraction-limited spot size in the focus, which scales as $\Delta\theta \sim \lambda_0/dcos(\theta)$. Consequently, when the lens' diameter d decreases below λ_0, the accuracy degrades severely. This accuracy can be quantified in terms of a minimum detectable angle change $\delta\theta$ that is ultimately limited by the presence of noise. In this work, we demonstrate that non-Hermitian coupling between neighboring photodetector elements can be exploited to for the first time realize an intrinsically subwavelength-sized ASP with a $\delta\theta$ = 0.24 degrees. Such a small $\delta\theta$ would be unimaginable for a subwavelength pixel without this type of optical coupling.

A similar challenge in the miniaturization of angle sensors is encountered in a completely different context: directional hearing in animals. Using two *independent* ears, large mammals can easily determine the incident angle of sound based on two well-understood mechanisms as illustrated in Fig. 4.1(b)-(c) [5]. The first relies on the interaural time difference (ITD) of the arrival time of the sound. The second method, the interaural intensity difference (IID) measures the intensity difference caused by the shadow of the body. Both mechanisms completely fail in small animals of subwavelength sizes. The ITD becomes too small to detect directly from the timing between neural spikes [6]. The IID also diminishes as the shadow of a subwavelength body is blurred by wave diffraction. How small animals achieve directional hearing has been a subject of intense research and debate for many years. It is believed that the signals acquired by two ears need to couple [7-9], in great contrast to the essentially independent ears used by large animals. For example, a gecko uses a tunnel through the head to acoustically couple two eardrums (Fig. 4.1(d)) [10-11]. Acoustic simulations suggest that this coupling greatly amplifies interaural differences [12-13].

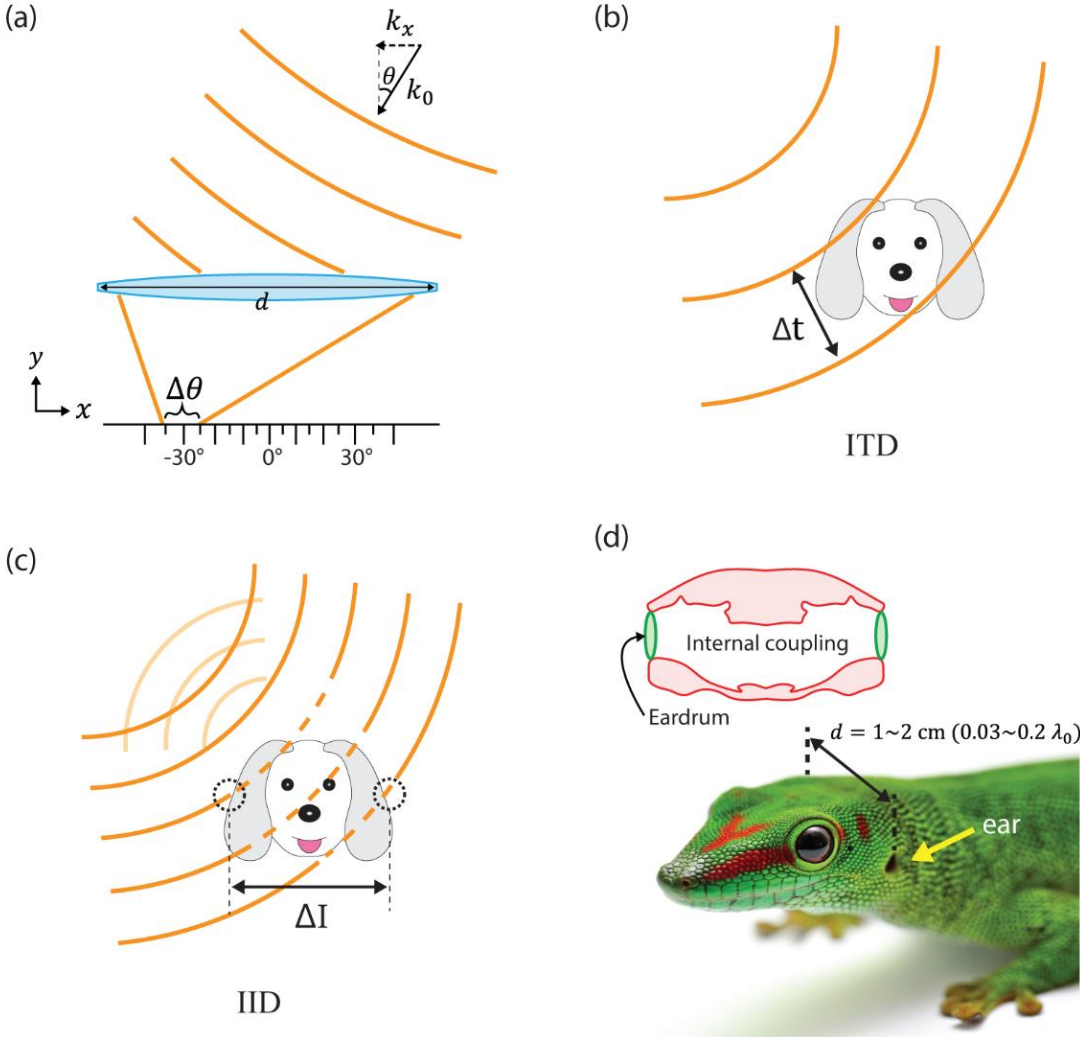

Fig. 4.1. (a) Concept of incident angle detection using a lens with a diameter d that produces a finite-sized spot in its focal plane when illuminated by an off-axis, collimated beam. The angular spread $\Delta\theta$ resulting from diffraction limits the minimum detectable angle change given a limited signal-to-noise ratio in a real optical measurement. (b) and (c) Directional hearing of animals based on the detection of an interaural time difference (ITD) or interaural intensity difference (IID). Δt is the arrival time difference and ΔI is the intensity difference between two ears. (d) Head structure of a gecko showing internal coupling between two eardrums. The distance d between two

ears is typically 1 to 2 cm and thus on a subwavelength scale with respect to audible sound wavelengths in the range from 8.5 - 34 cm. Image credit: marima/Shutterstock.com.

Closely following the design of the auditory system in small animals [12 -13], here we design a subwavelength photodetection pixel that can measure both the intensity and the incident angle of light. It consists of two nanoscale optical resonators, which serve the equivalent role of the two eardrums (Fig. 4.2(a)). In our case, two Si nanowires serve as the optical resonators. They can internally circulate light to produce standing electromagnetic waves in an analogous way as an eardrum hosts standing mechanical vibrations [14-16]. Because of the high refractive index of semiconductors, the sizes of resonators and their separation can be much smaller than the free-space optical wavelength. By electrically contacting each nanowire to form photodetectors, they afford measurement of the internally stored optical energy through simple photocurrent measurements. We will show that the two electrically-isolated and optically-coupled photodetectors allow angle-sensing by monitoring the difference in stored energy between the resonators.

4.2 Coupled mode theory and non-Hermitian coupling

We start by modeling the simple case of two single-mode resonators coupled to the free-space continuum as [17-19]:

$$i\frac{d}{dt}\begin{pmatrix}a_1\\a_2\end{pmatrix} = H_0\begin{pmatrix}a_1\\a_2\end{pmatrix} + H_i\begin{pmatrix}a_1\\a_2\end{pmatrix} + i\kappa_\theta S(\theta)\begin{pmatrix}\exp(-i\pi\, sin(\theta)\, d/\lambda)\\ \exp(i\pi\, sin(\theta)\, d/\lambda)\end{pmatrix} \tag{1}$$

where $\left|a_{1,2}\right|^2$ is normalized to represent the stored energy in the resonators. $H_0 = \begin{pmatrix} \omega_0 - i\gamma & 0 \\ 0 & \omega_0 - i\gamma \end{pmatrix}$ is the usual Hamiltonian for a pair of two independent resonators with ω_0 and γ being the resonant frequency and the decay rate, respectively. The incident light, whose flux is represented by $S(\theta)$, pumps energy into two resonators with an effectiveness determined by a coupling rate κ_θ. It is important to note that the phases $\mp\frac{i\pi\,sin(\theta)d}{\lambda}$ of the excitation wave at the relevant location of each resonator are different because of their spatial separation. A similar coupled mode theory can be derived for coupled acoustic resonators [20].

We turn our focus to the non-Hermitian Hamiltonian $H_i = \begin{pmatrix} 0 & \gamma_c \\ \gamma_c & 0 \end{pmatrix}$, which facilitates an angularly-dependent response. The coupling strength is quantified by $\gamma_c = \gamma_r + i\gamma_i$, where γ_r and γ_i describe the real and the imaginary part of the coupling strength, respectively. The real part γ_r is governed by the exchange of virtual photons [21], while the imaginary part γ_i arises when localized resonators couple to the same optical mode(s) in the continuum in an open system [22], a conceptually similar origin as the super and subradiance seen for a collection of quantum emitters [23-26]. This non-Hermitian coupling allows the incident light to manipulate the local storage of resonant energy at a deep subwavelength scale. For example, Ref [22] shows the spectral resolving capability using non-Hermitian interaction.

To show the effect of coupling, we first analyze the useful reference case when there is no coupling $\gamma_c = 0$, which is realized when two resonators are far away from each other ($d \gg \lambda_0$). As shown by the black line in Fig. 4.2(b), the energies in the two resonators are always the same i.e. $|a_1|^2 = |a_2|^2$ regardless of the incident angle. In contrast, when the resonator spacing is reduced to $d \leq \lambda_0$, there is a non-Hermitian coupling $\gamma_c \neq 0$, resulting in a strong angular response to the incident light. As shown by the red line in Fig. 4.2(b), the ratio of the amplitudes in the two resonators provides an unambiguous way to determine the incident angle. Resonances are not only beneficial for enhancing the light absorption in the nanowires, they are also critical for achieving angle sensing as we will show in the next paragraph. If we choose a low-index material for the same nanowire geometry, which would not support a resonance in the spectral regime of interest, angle sensing does not work.

Next, we discuss how the imaginary part of the coupling gives rise to an angularly-dependent response. The mathematical framework that leads to Eq.1 allows for a straightforward calculation of the energy storage in the individual nanowires, which is needed to predict the photocurrent generation in each wire. However, to understand the angle-dependence of the photoresponse, it is more insightful to describe the system in terms the superradiant and subradiant eigenstates supported by the optically-coupled pair of nanowires. We illustrate this point for two electric dipole resonators that oscillate in phase for the even, superradiant eigenstate and 180° out-of-phase for the odd, subradiant eigenstate. The distinct symmetry of these eigenstates naturally gives rise to the different angular radiation patterns shown in Fig. 4.2(c). By reciprocity, when light is incident from different angles, the excitation amplitudes of the super and subradiant are also different. For illumination at normal incidence, only the superradiant eigenstate is excited and thus the two resonators have equal amplitudes. When the incident light tilts away from the normal, the subradiant eigenstate can also be excited. When both even and odd eigenstate are excited simultaneously, their fields amplitude will add constructively in one wire and negate each other in the other wire. In other words, the energy is redistributed between the wires to make the photocurrent generation in one wire more effective. As the odd eigenstate is subradiant and features a higher radiation Q than the even, superradiant eigenstate, the energy storage in this state can become significant with minor tilting of the incident beam. Naively, it is expected that a smaller spacing will give rise to stronger γ_i and thus a greater angular response. However, γ_r also increases with smaller spacing and this coupling cannot be larger than the bandwidth of the resonators to avoid a detrimental splitting of the Eigen-frequencies of the super and subradiant eigenstates. On the other hand, the imaginary part of the coupling never splits the Eigen-frequency and can take any large value.

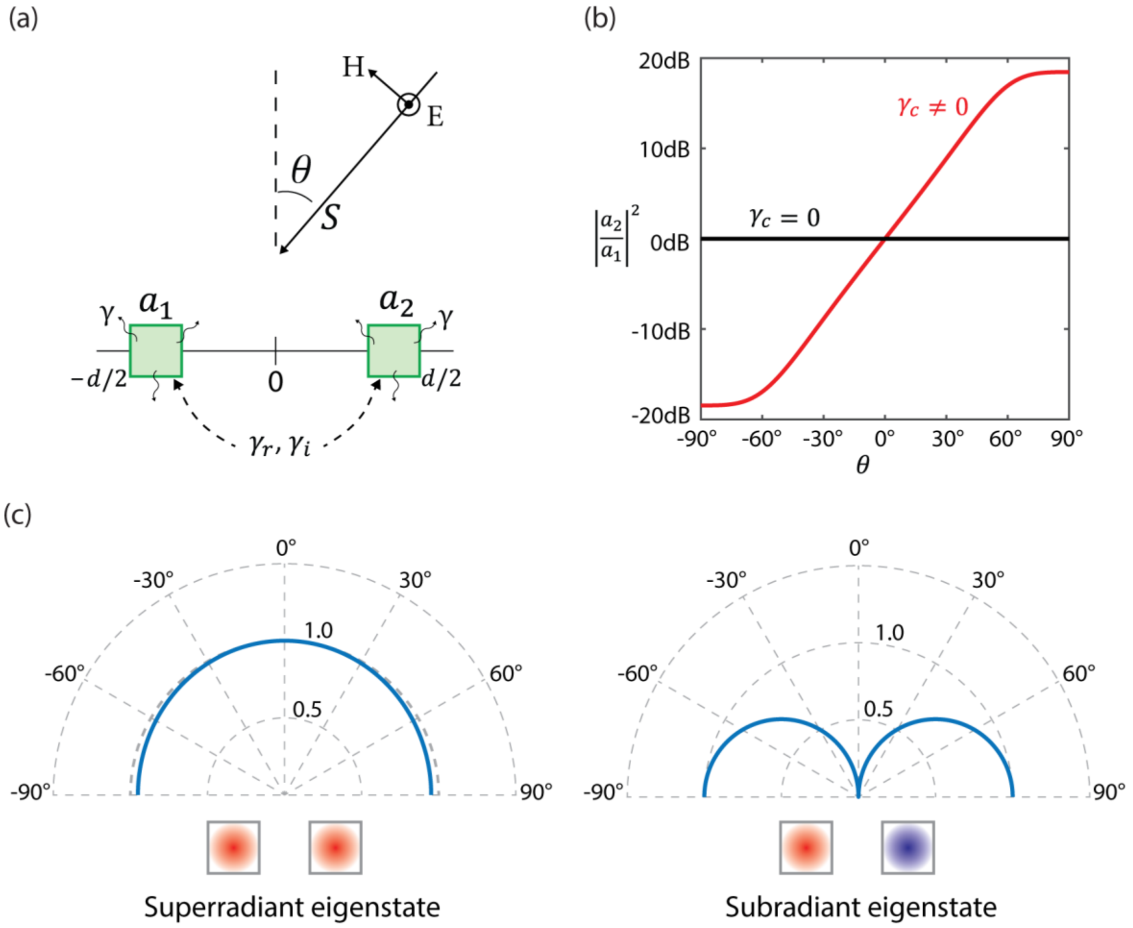

Fig. 4.2. (a) Schematic of the coupled mode theory for two resonators having amplitudes a_1 and a_2 separated by a distance d. S, γ_i, and γ_r quantify the power of the incident light, the imaginary part, and the real part of the coupling strength, respectively. (b) Ratio of the stored energy in two resonators. It strongly depends on the incident angle for the coupled case (red line), whereas it

remains at 1 for decoupled resonators (black line). $d = 0.05\ \lambda_0$ and $\gamma = 0.01\ \omega_0$ is used for both $\gamma_c = 0$ and $\gamma_c \neq 0$ cases. $\gamma_c = 9.8 \times 10^{-3}\ \omega_0$ is used for $\gamma_c \neq 0$ case. (c) Example of the angular profile (blue curves) and the phase configuration of the radiation of the super and subradiant eigenstates for the case of electric dipole radiators. Here we assume the spacing between the two is much smaller ($0.1\ \lambda_0$) than wavelength. Red and blue are used to indicate a phase difference of π.

4.3 Coupling between two Si nanowires

We implement the subwavelength resonator using two Si nanowires on a SiO_2 substrate, as schematically shown in Fig. 4.3(a). Both the width and height of the nanowire are 100 nm. Despite its subwavelength size, each wire supports several strong resonances in the visible spectral regime [14-15, 27-28]. Whereas the example above describes the case where each nanowire supports a single-mode at the illumination frequency, it is important to note that some nanowire modes can be doubly degenerate. In these cases the coupled mode theory needs to include four modes.

Using full-wave simulations of Maxwell's equations, we examine how the light absorption in the nanowires changes with the illumination direction. The local absorption in the nanowires is calculated by computing $\sigma(\omega)|E|^2$ in the structures where $\sigma(\omega)$ is the conductivity at the angular frequency ω and E is the electric field. The illumination wavelength is fixed at 550 nm with the incident electric field polarized along the nanowire, causing the excitation of the doubly degenerate, second-order mode TM_2. We first set the spacing to be 100 nm, for which strong coupling is expected. Indeed, the absorption difference shows a strong angular dependence as shown by the red line in Fig. 4.3(b). The maximum contrast ratio for the absorption is around 3. Figure 4.3(c) shows the spatial distribution of the absorption for different incident angles. The bright red color indicates strong absorption while the dark blue is for zero absorption. Under normal incidence when $\theta = 0°$, the two nanowires display an identical absorption profile. The flow of light changes to concentrate more light in one wire when the incident angle is tilted away from the normal. Figure 4.3(a) shows the calculated flow lines of the Poynting vector (black lines) to illustrate the flow of light in the vicinity of the resonators when light is incident from the left at a $45°$ angle. The resonator on the left effectively “casts a shadow” and reduces the absorption in the nanowire on the right. The extent of the shadow, measured by the absorption cross section, can often be much larger than the resonator’s geometrical size [29].

When we set a larger spacing of $d = 2\ \mu$m to effectively eliminate the coupling γ_c, there is no absorption difference in the two nanowires, regardless of incident angle (black line in Fig. 4.3(b)). In Fig. 4.3(d), two resonators always have the same absorption $\sigma(\omega)|E|^2$ profile, despite the spatial pattern of light absorption varies for different incident angles.

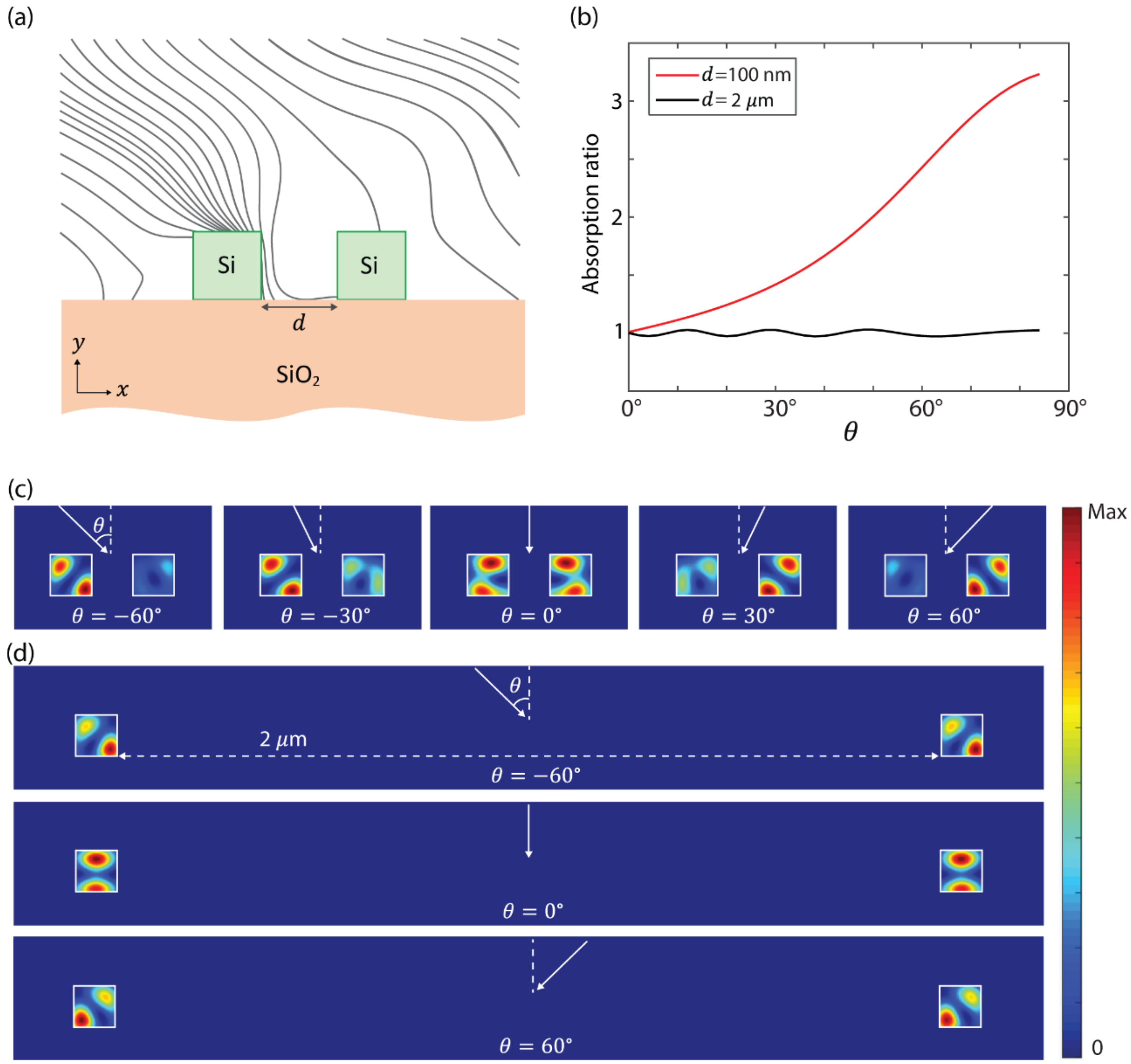

Fig. 4.3. (a) Cross-sectional view of two Si nanowires on SiO_2 substrate with Poynting flux lines for a 45° incident angle θ. (b) Absorption ratio between two silicon nanowires for d = 100 nm (red) and d = 2 μm (black) as a function of incident angle. (c) Absorption profile $\sigma(\omega)|E|^2$ for different incident angles, normalized by the highest absorption density in each case. When d = 100 nm, absorption ratio change between two nanowires is clearly visible for different incident angles. (d) When d = 2 μm, both nanowires feature an almost identical absorption profile for any incident angle. (a)-(d) Electric field of incident wave is along z-direction (TM polarization).

4.4 Angle sensing photodetectors

Now we describe the experimental demonstration of angle sensing photodetectors. Figure 4.4(a) shows the schematic of a fabricated device. Gold electrodes cover the two ends of each nanowire to form two photodetectors. These two photodetectors are electrically isolated from each other, but optically coupled. Two photocurrents can be measured from this four-terminal device. The difference in photocurrent is proportional to the difference in light absorption, which tells the incident angle of light.

Figure 4.4(b) shows a scanning electron microscope (SEM) image of the device. For the fabrication, a lightly n-doped Poly-Si is deposited on a glass substrate, followed by electron beam lithography to define the nanowires and gold contacts. The inset shows a close-up view of the 105-nm-wide (A and C) nanowires separated by an equally large gap (B). Each nanowire forms a photoconductive detector whose resistance changes upon illumination. The voltage-current relation shows good Ohmic contacts. To characterize the optical resonance in the nanowires, we measure the spectra of the photocurrent for normally-incident light. Both the TM_2 (Fig. 4.4(c)) and the TE_1 (Fig. 4.4(d)) polarizations, where the subscripts indicate the order number of the resonance, exhibit a resonant peak in the visible wavelength range.

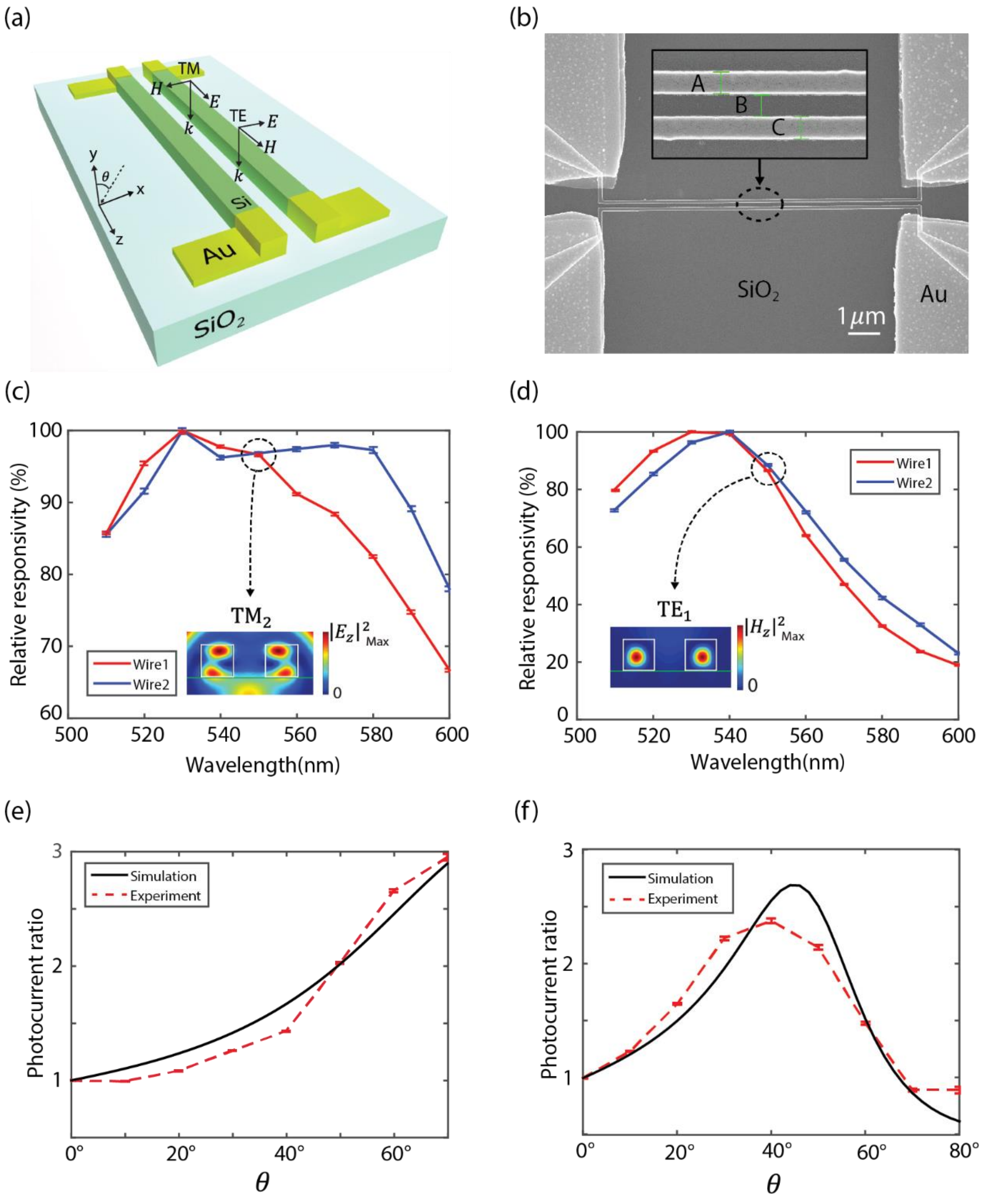

Fig. 4.4. (a) Schematic of an angle-sensing photodetector. (b) Scanning electron microscope image of fabricated angle sensing photodetector. Top inset shows a close-up view where A=105 nm, B=105 nm and C=103 nm. (c) Normalized responsivity of two nanowires with electric field polarized in z-direction. The responsivity is defined as R=I/P, where *I* is the measured photocurrent; P is the incident power. Inset shows the electric field intensity for TM_2 mode. (d) Normalized

responsivity of two nanowires with magnetic field polarized in z-direction. Inset shows the magnetic field intensity for TE_1 mode. (e) Photocurrent ratio between two nanowires as a function of θ with the same polarization as in (c). (f) Photocurrent ratio between two nanowires as a function of θ with the same polarization as in (d).

We measure the angular response at the wavelength of 550 nm. For TM polarization, the photocurrent ratio increases from 1 to 3 as the incident angle increases from 0° to 70° (Fig. 4.4(e)). For TE polarization, the photocurrent ratio increases monotonically up to 45° (Fig. 4.4(f)). In both cases, the experimental results agree with the full-wave simulations (solid lines Fig. 4.4(e)-(f)) very well. The peak in Fig. 4.4(f) is created by the unique radiation profile of the TE superradiant eigenstate. This detector can work for unpolarized light by confining the field of view (FOV) to $\pm 45°$, sufficient for many applications.

Angle-sensing has a wide range of applications in the radio frequency (RF) regime, including most prominently for direction finding. This includes a recent work on employing subwavelength antennas [30]. RF direction finding is relatively straightforward because the phase information of RF signals are easily preserved in the detection process. As a result, most RF methods rely on coherently combining multiple signals received at different locations or rely on antennas that are much larger than the operating wavelength. These methods cannot be applied to optical signals because optoelectronic conversion is intrinsically an incoherent process in which all phase information is lost. To overcome this limitation, we manage to integrate coherent manipulation of optical waves directly into optoelectronic conversion through the use of coupled nanowires. It represents a new class of detectors that provides direct access to the coherent properties of light.

4.5 Depth sensing

One immediate application of angular photodetectors is depth-sensing. As a demonstration, we use two angle-sensing photodetectors to triangulate the position of a light emitting diode (LED). A top view photograph of the experimental setup is provided in Fig. 4.5(a). It shows the photodetectors and LED as placed in the same horizontal plane. The LED light source has a center wavelength of 520 nm. A chopper is used together with a lock-in amplifier to measure the photocurrent. Two angle-sensing detectors are mounted on two chips separated by 50 mm. A top view schematic is shown in Fig. 4.5(b). All coordinates are in the unit of millimeter. Using triangulation, the location of the LED during movement, including both the lateral position *x* and the depth *y*, can be obtained from the measured incident angles $\Theta_{1,2}$ for the LED light falling onto the two angle sensors:

$$(x, y) = \left(\frac{(tan\Theta_1)x_1 - (tan\Theta_2)x_2}{tan\Theta_1 - tan\Theta_2},\ \frac{tan\Theta_1 \cdot tan\Theta_2}{tan\Theta_1 - tan\Theta_2} \cdot (x_1 - x_2)\right) \qquad (2)$$

where $x_{1,2}$ are the coordinates of the two detectors. Θ in Eq. (2) is defined with respect to horizontal plane i.e. $\Theta = 90°$ for normal incidence.

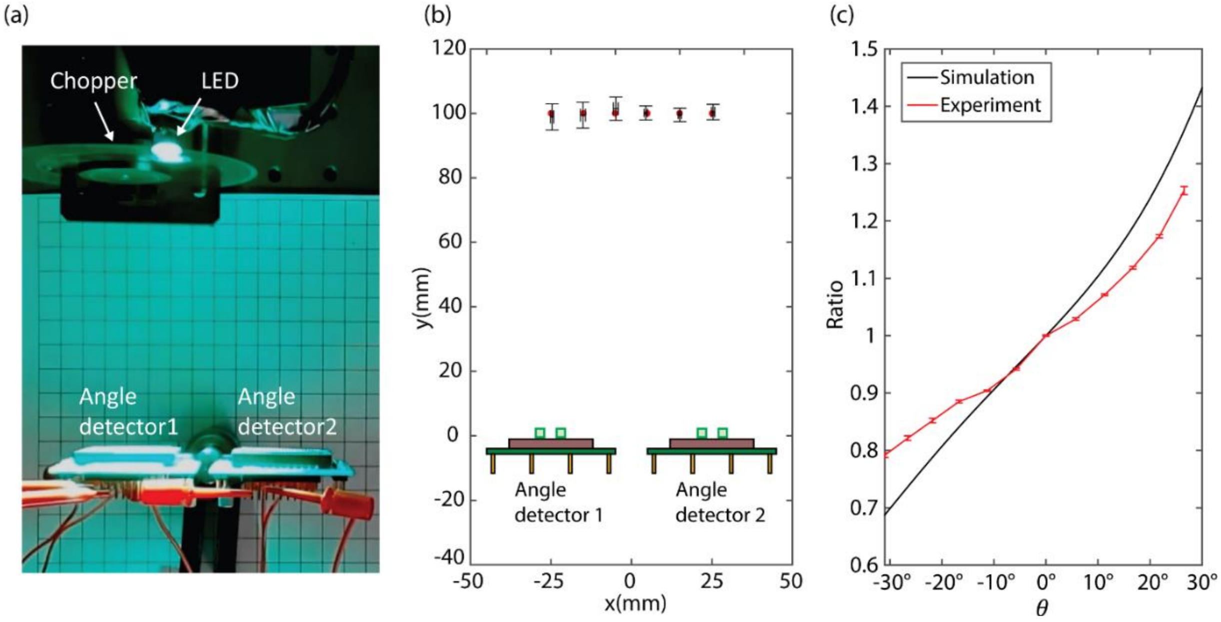

Fig. 4.5. (a) Measurement setup for lens-less positioning. (b) LED position uncertainty in x- and y-direction for six discrete measurements in 2D plane where the red dots represent the true location of LED light source. Error bars are generated using 50 measurements at each location with propagation of uncertainty method. (c) Full-wave simulation and experimentally measured photocurrent ratio under unpolarized light.

In the experiment, we first characterize the angular response of an individual angle-sensing photodetector under LED illumination up to angles of $\pm 30°$. A monotonic angular profile is obtained (red line in Fig. 4.5(c)), in agreement with the full-wave simulation results (black line in Fig. 4.5(c)) for unpolarized light . The error bars in Fig. 4.5(c) are generated based on 100 measurements in each location. The average length of the error bars is 0.006. Using the experimental curve as the calibration, we measure the incident angles $\Theta_{1,2}$ of the light and then use Eq. (2) to estimate the location of the LED. The black markers in Fig. 4.5(b) show the calculated LED positions while the red markers show its true locations. The triangulation provides an excellent measurement of the location of light source. We used an LED light source embedded in a hemispherical glass lens with a diameter of 5.6mm. In this experiment, we assume the LED as a point source.

The depth of an object in a scene provides critical information for the navigation of autonomous systems such as self-driving cars. Compared to existing methods based on time-of-flight or stereo cameras [31], angular photodetectors provide a much simpler solution to depth-sensing. It can reach centimeter accuracy for a range up to ten meters, which is comparable to leading commercial depth sensors [32]. More importantly, it does not use any lenses or require time synchronization. In addition, the possibility to fabricate the device using standard semiconductor fabrication techniques can enable low cost solutions.

Finally, we discuss the limitation of this angle sensor and the potential ways to overcome these limitations. The geometry of two nanowires represents a faithful imitation of the coupled ears of small animals. Consequently, this design also inherits the same limitations found in the biological world, including a limited operational bandwidth, lack of full azimuth and elevation angle capability, and a difficulty in differentiating multiple incoming waves. For example, the crickets' directional hearing only works in a narrow spectral band tuned to the species' song [33]. The limitations of these natural designs can be overcome. For example, by using two pairs of angle detectors orientated orthogonally, one can detect both azimuth and elevation angles. One can also use multiple (instead of two) resonant detectors to expand the bandwidth of operation and to differentiate multiple incident waves. These designs generally use more than two "ears", which is expensive for a biological system but is straightforward to implement in integrated device technologies.

4.6 Minimum detectable angle change

The minimum detectable angle change is determined by the contrast ratio for the photocurrent as well as the signal-to-noise ratio (*SNR*) of the photodetector. For near-normal incidence, the minimum detectable angle change can be calculated as $\delta\theta = \frac{2}{SNR}\frac{D}{R_{max}-1}$ assuming a linear angular dependence that has a dynamic range up to D degree and a maximum contrast ratio of R_{max}. Derivation of the minimum detectable angle change is shown below.

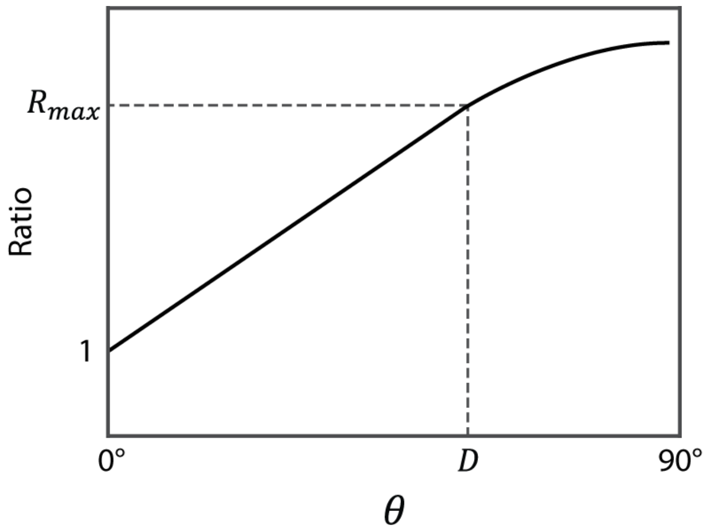

Fig. 4.6. An example of a contrast ratio of photocurrent having a linear response up to D degree.

The angular accuracy for the two-wire detector system $\delta\theta$ can be expressed as:

$$\delta\theta = \Delta R \cdot \frac{d\theta}{dR} \tag{3}$$

where R is the contrast ratio. Assuming a linear angular dependence as in Fig. 4.6, $d\theta/dR$ can be expressed as

$$\frac{d\theta}{dR} = \frac{D}{R_{max}-1} \tag{4}$$

where D is the dynamic range of the incident angle and R_{max} is the maximum contrast ratio at D degree. Now we calculate the accuracy for incident light around normal direction. Since $R = I_1/I_2$ where I_1 and I_2 are the photocurrent in two nanowires, ΔR can be expressed as:

$$\Delta R = \left|\frac{dR}{dI_1}\right| \Delta I_1 + \left|\frac{dR}{dI_2}\right| \Delta I_2 = \left|\frac{1}{I_2}\right| \Delta I_1 + \left|\frac{I_1}{I_2^2}\right| \Delta I_2 \tag{5}$$

Since $I_1 \approx I_2$ for normal incident direction, the equation above can be simplified as

$$\Delta R = \left|\frac{1}{I_1}\right| \Delta I_1 + \left|\frac{1}{I_2}\right| \Delta I_2 = \frac{2}{SNR} \tag{6}$$

Thus, substituting Eq. 4 and 6 into Eq. 3, we get

$$\delta\theta = \frac{2}{SNR} \cdot \frac{D}{R_{max} - 1} \tag{7}$$

In our measurement, we obtain a maximum SNR of 28 dB by using a lock-in amplifier and averaging over multiple measurements. This *SNR* leads to a $\delta\theta$ of 0.32 degree. Our detectors are photoconductors, which are known to have high noise levels. Future experiments could employ photodiodes together with integrated amplification circuits to greatly reduce noise. For example, using CMOS image sensing technology a typical *SNR* of 43.4 dB in Ref [34] can be reached and this leads to a $\delta\theta$ of 0.009 degrees. In addition, the coupled mode theory suggests that the contrast ratio and angular accuracy can be further enhanced by increasing the quality factor and optimizing the evanescent coupling.

4.7 Modal profiles and spectral response of resonant Si nanowires

Figure 4.7 shows the absorption cross section spectrum and field profiles of a single nanowire with a 100 nm width and height on top of a SiO_2 substrate for normal incident light. The finite difference frequency domain (FDFD) method was used for the calculations. Figure 4.7(a) shows the spectrum for TE polarized light and the field profiles of $|H_z|^2$ at each of the resonance peaks are shown. The lowest resonant mode for TE polarized light appears around a 590 nm wavelength and higher order modes are seen around 450 nm and 390 nm. Figure 4.7(b) shows the spectrum for TM polarized light and the field profiles of $|E_z|^2$ at each of the resonance peaks are shown. The fundamental mode for TM polarized light is located beyond 1 μm wavelength and is not shown. Higher-order modes are seen around wavelengths of 600 nm, 440 nm, and 400 nm.

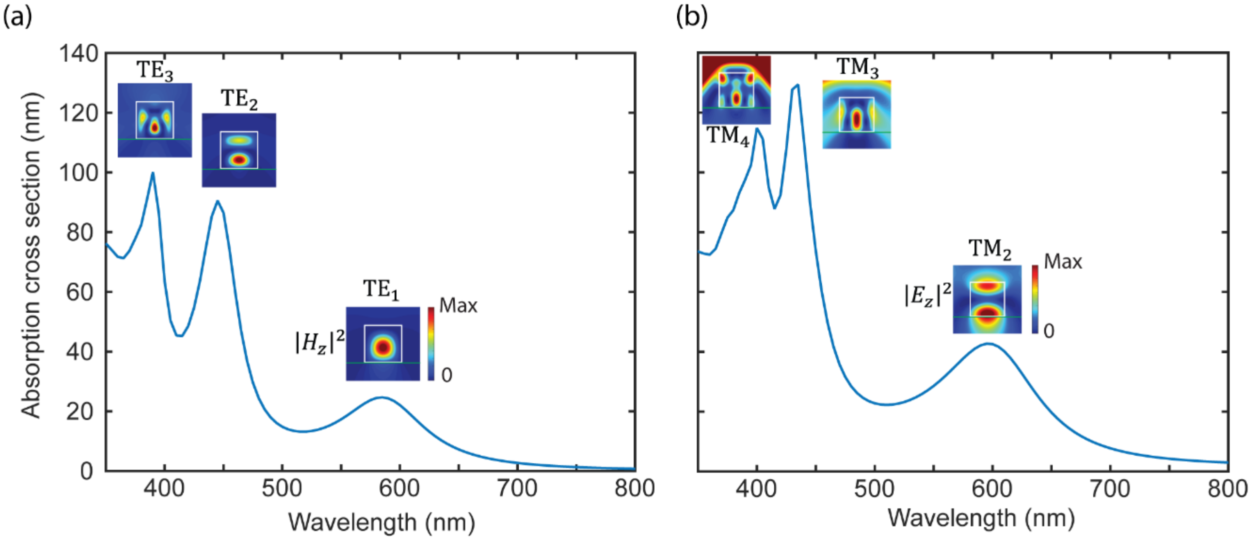

Fig. 4.7. (a) Absorption cross section spectrum and its $|H_z|^2$ field profiles on resonance peaks for a Si nanowire on top of a SiO_2 substrate with TE polarization. Width and height of Si nanowire are 100 nm. (b) Absorption cross section spectrum and its $|E_z|^2$ field profile of Si nanowire for TM polarization.

4.8 Experimental voltage-current relation and responsivity

Figure. 4.8 shows the voltage-current relationship of both nanowires without incident light i.e. dark current. A DC power supply is used to apply the voltage and measure the current. Both nanowires show an Ohmic contact. As a result, the photodetection device is a photoconductor-type detector.

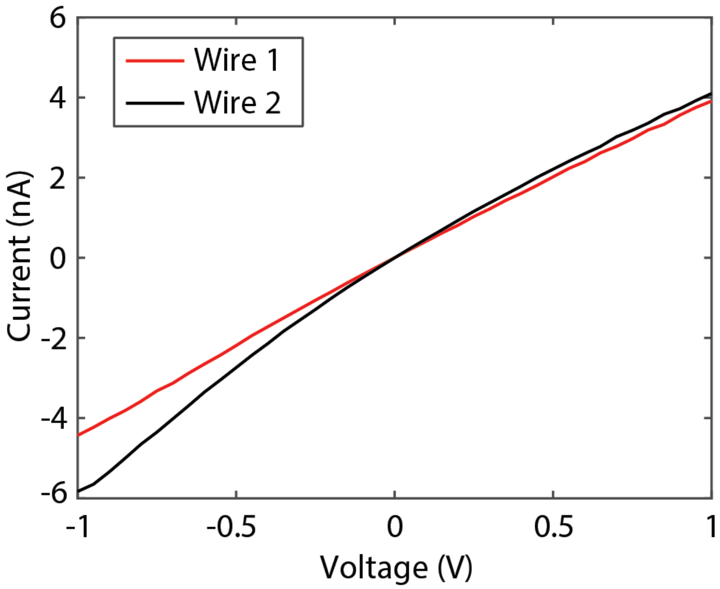

Fig. 4.8. Voltage-current measurement of two Si nanowires. Both nanowires show a resistor-like behavior.

The responsivity of two nanowires at 550 nm wavelength are 0.52 A/W and 0.34 A/W for TE mode and 0.5 A/W and 0.31 A/W for TM mode. It is calculated by considering the geometrical area of the nanowire and the incident power density, which is estimated to be around 60 W/m^2. We note that nanowires increase the absorption cross sections, which often exceed the geometric cross sections. Near-unity absorption can be realized in nanowire arrays. Figure 4.9 shows the measured photocurrent and responsivity of two nanowires for normal incident light with TE and

TM polarization. Two nanowires have different responsivity. They differ by a factor of 1.53, which could be attributed to fabrication variation. This responsivity difference is factored in when we calculate the ratio of the two photocurrents.

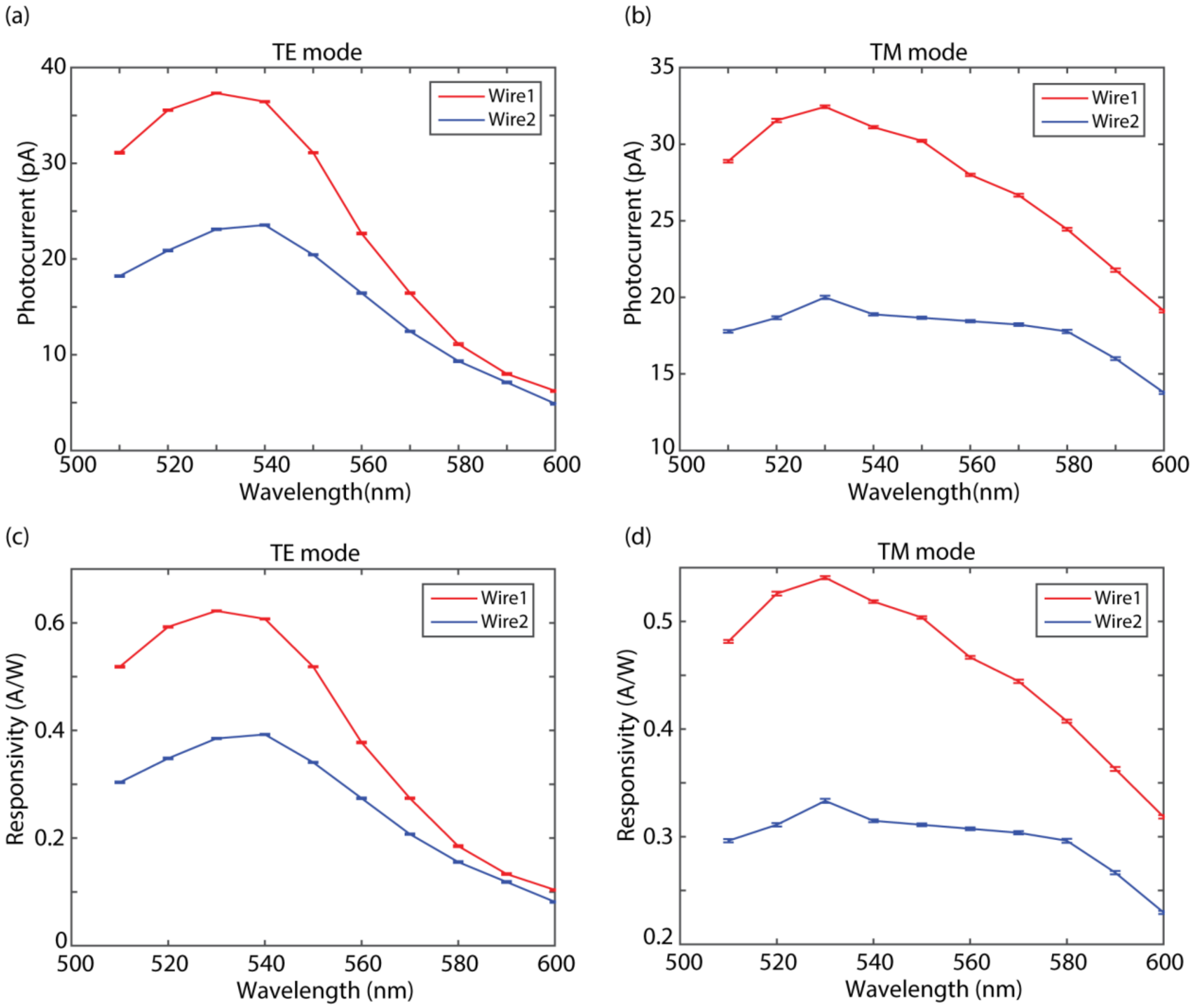

Fig. 4.9 The spectra of the measured photocurrent and calculated responsivity of two nanowires under illumination of TE and TM light.

4.9 Short nanowires for angle sensing

The length of the nanowires shown in Fig. 4.4(b) is 10 μm, which is used to avoid light scattering from the large electrodes. The length of the nanowires can be reduced down to a subwavelength length and yet an angle –sensing pixel can maintain its angular response. We show the angular response for nanowires that are only 300 nm long. Figure 4.10(a) shows the schematic of two parallel Si nanowires that are 300 nm long and placed on top of a SiO_2 substrate. The gap between the two nanowires are 100 nm and the nanowires feature a 100 nm × 100 nm cross-sectional area. The angular response of these angle sensing pixel is shown in Fig. 4.10(b). The energy ratio between the two nanowires is 1 at normal incidence ($\theta = 0°$) and maintains a monotonically increasing angular response up to $\theta = 40°$ under illumination of unpolarized light.

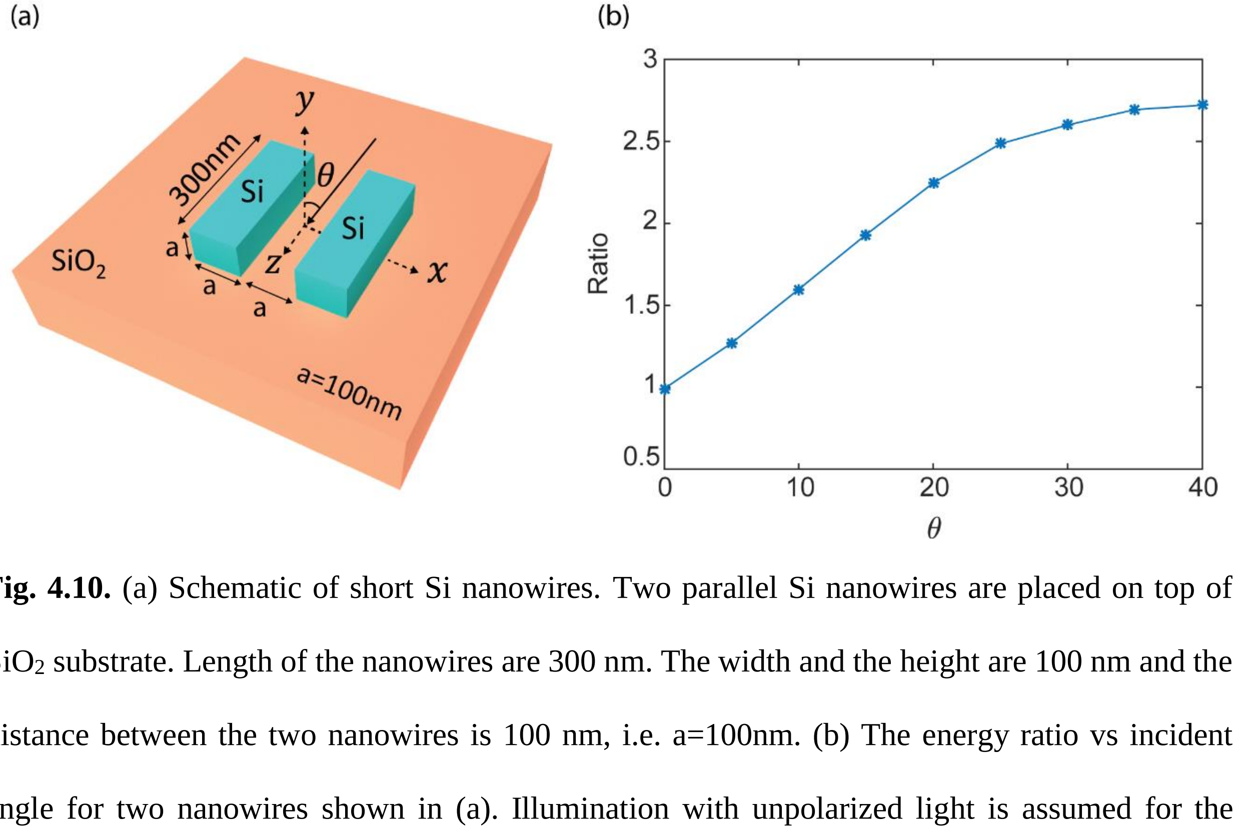

Fig. 4.10. (a) Schematic of short Si nanowires. Two parallel Si nanowires are placed on top of SiO_2 substrate. Length of the nanowires are 300 nm. The width and the height are 100 nm and the distance between the two nanowires is 100 nm, i.e. a=100nm. (b) The energy ratio vs incident angle for two nanowires shown in (a). Illumination with unpolarized light is assumed for the calculations.

4.10 Spacing between arrays of angle sensing pixels

The optical cross section of the nanowires can be very large due to the optical resonances supported by the wires. Therefore, when angle sensing pixels are densely packed on a chip, there is a minimal spacing between pixels for the most optimal operation. When the spacing is smaller than then the illumination wavelength, neighboring pixels can no longer be considered as being by themselves and the interaction between nearby pixels can reduce the accessible range for the angle sensing.

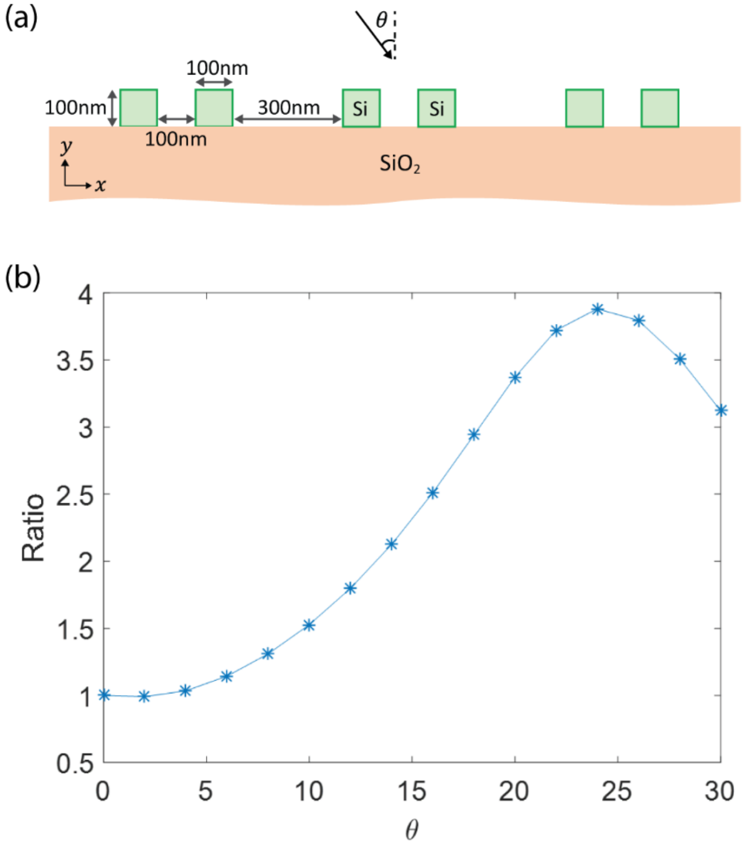

Fig. 4.11 (a) Schematic of three detectors placed next to each other with 300nm gap to form an array of angle sensing detectors. (b) Energy ratio of two nanowires in single pixel under incident

light having 580 nm wavelength. Periodic boundary condition and unpolarized light is used for the calculation.

Figure 4.11(a) shows an array of angle sensing detectors placed next to each other with 300 nm spacing. Figure 4.11(b) shows an energy ratio between two nanowires of one of the angle sensing detector. Incident light with a wavelength of 580 nm and unpolarized light is used for the calculation. Since the spacing between the detectors are smaller than the wavelength of incident light, there will be a strong coupling between neighboring detectors and this will affect the dynamic range. As it can be seen in Fig. 4.11(b), the dynamic range is only up to 25 degree. The reduced dynamic range is a trade-off for densely packing the detectors. However, when the spacing between detectors increase to 500 nm, the coupling effect become negligible and dynamic range increases.

4.11 Working principle of an angular sensing capability in coupled resonators

As we discussed in the main text, the non-Hermitian coupling between coupled resonators facilitates angular sensing. In this section, we will discuss the underlying principle in detail using coupled mode theory.

Two resonators coupled to the free-space continuum can be modelled using coupled mode theory as

$$i\frac{d}{dt}\begin{pmatrix} a_1 \\ a_2 \end{pmatrix} = \begin{pmatrix} \omega_0 - i\gamma & 0 \\ 0 & \omega_0 - i\gamma \end{pmatrix}\begin{pmatrix} a_1 \\ a_2 \end{pmatrix} + \begin{pmatrix} 0 & \gamma_c \\ \gamma_c & 0 \end{pmatrix}\begin{pmatrix} a_1 \\ a_2 \end{pmatrix}$$

$$+ i\kappa_\theta S(\theta)\begin{pmatrix} \exp(-i\pi\, sin(\theta)\, d/\lambda) \\ \exp(i\pi\, sin(\theta)\, d/\lambda) \end{pmatrix} \qquad (8)$$

where $\left|a_{1,2}\right|^2$ is normalized to represent the energy of the resonant modes. ω_0 and γ are the resonant frequency and the decay rate, respectively. The non-Hermitian coupling strength is given by $\gamma_c = \gamma_r + i\gamma_i$, where γ_r and γ_i quantify the strength of the real and the imaginary parts of the coupling strength, respectively. The incident light, whose flux is represented by $S(\theta)$, pumps energy into two resonators with an effectiveness determined by a coupling rate κ_θ. The phases$\mp i\pi\, sin(\theta)\, d/\lambda$ for the two resonators are different based on their spatial separation.

Under a steady-state excitation with an angular frequency of ω, we can elect to write the amplitude for each resonator mode as a superposition of the superradiant and subradiant eigenstates.

$$\begin{pmatrix} a_1 \\ a_2 \end{pmatrix} = \alpha(\omega,\theta) \begin{pmatrix} 1 \\ 1 \end{pmatrix} + \beta(\omega,\theta) \begin{pmatrix} -1 \\ 1 \end{pmatrix} \tag{9}$$

where $\begin{pmatrix} 1 \\ 1 \end{pmatrix}$ and $\begin{pmatrix} -1 \\ 1 \end{pmatrix}$ represent the in-phase superradiant and out-of-phase subradiant eigenstates, respectively. Here $\alpha(\omega,\theta)$ and $\beta(\omega,\theta)$ are the amplitudes of the in-phase and out-of-phase eigenstates, respectively. They are given by:

$$\alpha(\omega,\theta) = \frac{i\kappa_\theta S(\theta) cos(\frac{\pi\, sin(\theta)\, d}{\lambda})}{\omega - \omega_0 + i\gamma - \gamma_r - i\gamma_i} \tag{10a}$$

$$\beta(\omega,\theta) = \frac{-\kappa_\theta S(\theta) \sin\left(\frac{\pi\, sin(\theta)\, d}{\lambda}\right)}{\omega - \omega_0 + i\gamma + \gamma_r + i\gamma_i} \tag{10b}$$

The energy in the two resonators $|\, a_1|^2$ and $|\, a_2|^2$ can be written as:

$$|\, a_1|^2 = |\alpha(\omega,\theta)|^2 + |\beta(\omega,\theta)|^2 - 2|\alpha(\omega,\theta)\beta(\omega,\theta)|\cos(\Delta\phi) \tag{11a}$$

$$|\, a_2|^2 = |\alpha(\omega,\theta)|^2 + |\beta(\omega,\theta)|^2 + 2|\alpha(\omega,\theta)\beta(\omega,\theta)|\cos(\Delta\phi) \tag{11b}$$

Here $\Delta\phi$ is the phase difference between $\alpha(\omega,\theta)$ and $\beta(\omega,\theta)$.When the two resonators are completely decoupled, i.e. $\gamma_r = 0$ and $\gamma_i = 0$, the phase difference between the two eigenstates is always $\Delta\phi = \pi/2$, independent of the excitation frequency (dashed black line in Fig. 4.12(a)). This phase difference simply results from having even (cosine-like) and odd (sine-like) modes.

Without any form of coupling, this value of $\Delta\phi$ is also independent of the incident angle. Since the energy difference between the resonators is given by $4|\alpha(\omega,\theta)\beta(\omega,\theta)|\cos(\Delta\phi)$, the value of $\Delta\phi = \pi/2$ results in equal stored energy in the two resonators. This is intuitively expected for identical resonators without any type of optical coupling.

On the other hand, when the two resonators are coupled together, the phase difference generally deviates from $\pi/2$. Generally, both real and imaginary parts of coupling are present. In Fig. S3a we show the case where $\gamma_r = -0.5\gamma$ and $\gamma_i = 0.5\gamma$. In contrast to the case without coupling (dashed line), we have a phase difference close to π around the Eigen-frequency, resulting in very strong angular response (See Fig. 4.12(b)).

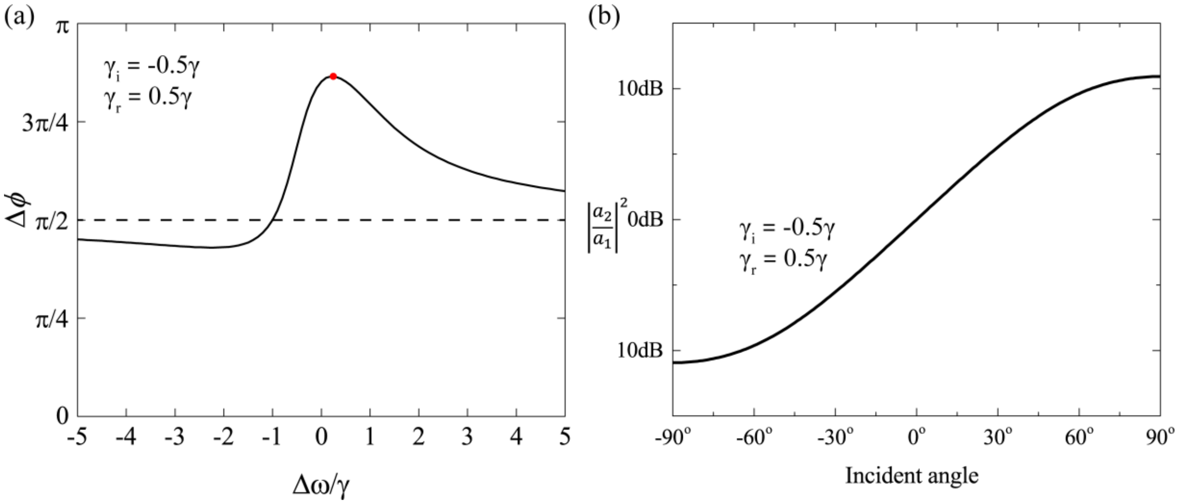

Fig. 4.12 Phase difference and contrast ratio of two resonators. (a) Phase difference for different amounts of frequency detuning from resonance ($\Delta\omega = \omega - \omega_0$). Here γ is the intrinsic decay rate of an individual resonator. The dashed line indicates the case without coupling, i.e. $\gamma_i = 0$ and $\gamma_r = 0$. The solid line indicates a case with both non-zero real and imaginary parts of the coupling strength, i.e. $\gamma_i = -0.5\gamma$ and $\gamma_r = 0.5\gamma$. (b) Contrast ratio at the maximum phase difference, which is marked in (a) by the red dot. The coupling provides a way to unambiguously determine the incident angle of a light beam.

Next, we elucidate the different ways in which the real and the imaginary parts of the coupling change our ability to determine the angle of an incident beam. This intimately linked to the way in which the coupling can modify the phase difference between the superradiant and subradiant eigenstates. In general, as the frequency of the excitation wave sweeps across an Eigen-frequency, the phase of the eigenstate incurs a π phase swing, starting from 0 far below the Eigen-frequency, gradually increasing to $\pi/2$ at the Eigen-frequency, and then eventually to π at frequencies far above the Eigen-frequency. As the frequency is increased, the amplitude also changes and reaches a maximum value at the resonance frequency. Figure 4.13(a) shows the characteristic phase evolution for the superradiant $\alpha(\omega,\theta)$ and subradiant $\beta(\omega,\theta)$ Eigenstates if we assume no coupling between the resonators, i.e. $|\gamma_i| = |\gamma_r| = 0$. Here, we offset the phase $\alpha(\omega,\theta)$ by $\pi/2$ to emphasize that the phase of $\beta(\omega,\theta)$ progresses in exactly the same manner. This results in a constant phase difference between the two at all frequencies (Fig. 4.13(d)). This is expected as both Eigenstates have the same resonant frequency and the same bandwidth. As $\Delta\phi = \pi/2$, each resonator features the same stored energy.

The coupling breaks this constant $\pi/2$ phase difference. In an open system, both the real and the imaginary parts of the coupling are generally non-zero, which makes the system non-Hermitian. To understand their different impact, we first look at the role of the imaginary part of the coupling γ_i by choosing a case where $|\gamma_i| \gg |\gamma_r|$. The imaginary part of the coupling does not break the energy degeneracy between the superradiant and subradiant Eigenstates. However, this coupling does change the bandwidth over which the π phase evolution occurs. The in-phase superradiant eigenstate decays more quickly at the rate $\gamma - \gamma_i$ and shows a faster phase evolution whereas the out-of-phase subradiant eigenstate decays more slowly at the rate $\gamma + \gamma_i$ and displays a slower phase evolution. Note γ_i is mostly negative for deep subwavelength. The resulting difference in the phase evolution (Fig. 4.13(b)) results in a spectral regime where the phase difference between the two Eigenstates can approach π, or 0 (Fig. 4.13(e)). Such phase differences result in a redistribution of the energy between the resonators and produce an angular response.

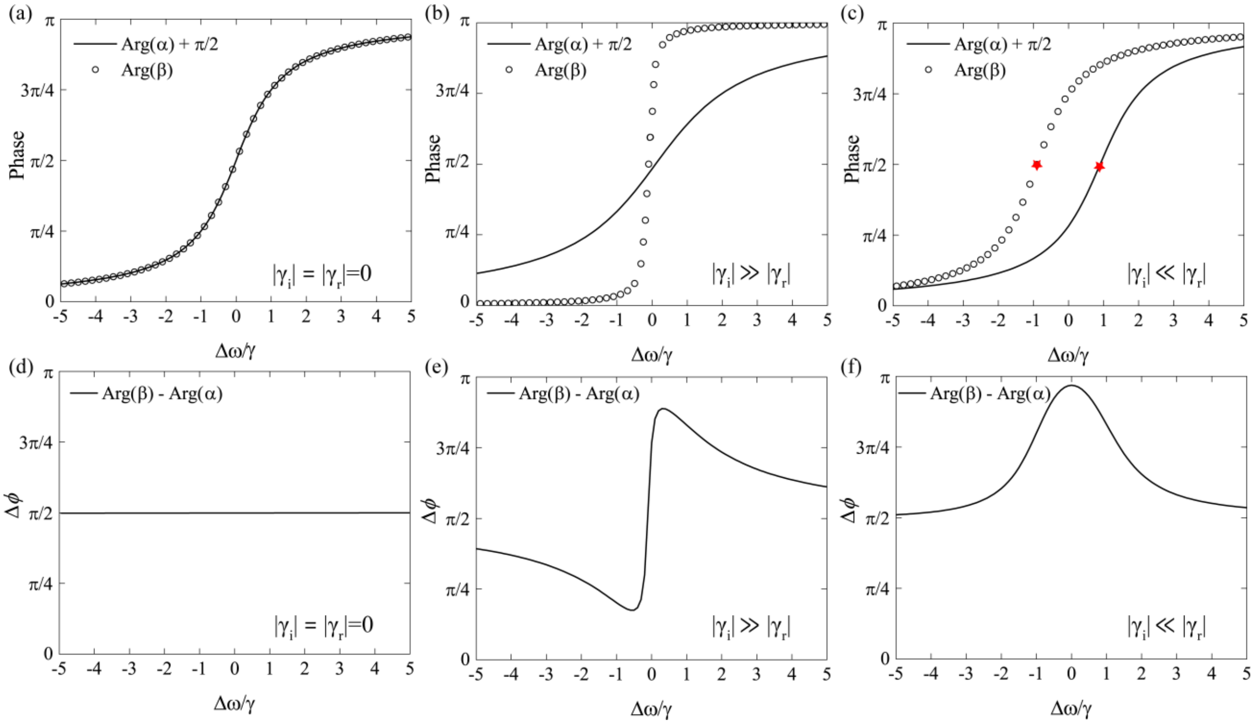

Fig. 4.13 Phase analysis of superradiant and subradiant Eigenstates. (a)-(c) Phases of the even and odd Eigenstates (a) without coupling, (b) when the imaginary part of coupling dominates, and (c) when the real part of coupling dominates. Note the phase of the in-phase eigenstate is always offset by $\pi/2$ for better visualization. Lines are the phase of superradiant Eigenstate while circles are for subradiant one. (d)-(f) Phase differences between the eigenstates (d) without coupling, (e) when the imaginary part of coupling is dominated, and (f) when the real part of coupling is dominated. Without coupling, the phase difference is always $\pi/2$. In great contrast, the couplings deviate the phase difference from $\pi/2$ by either changing the bandwidth (e) or shifting Eigen-frequency (f).

Next, we look at the impact of the real part of the coupling by choosing a case with $|\gamma_r| \gg |\gamma_i|$. The real part of the coupling lifts the energy degeneracy between superradiant and subradiant Eigenstates. The Eigen-frequency of the superradiant eigenstate becomes $\omega_0 + \gamma_r$, whereas that of the subradiant Eigenstate becomes $\omega_0 - \gamma_r$. These Eigen-frequencies are the centers of the phase swing as shown by the stars in Fig. 4.13(c). The lifting of the degeneracy splits the two phase evolution curves and this also results in a spectral regime where the phase difference deviates significantly from $\pi/2$ (Fig. 4.13(f)). However, the real part of the coupling cannot be much stronger than the bandwidth of the resonators, in which case the two Eigenstates energies are split so far that interference effects become weak.

4.12 Coupled mode theory: Calculation of the real and the imaginary parts of coupling coefficients

In this section, we show the calculation of the real and the imaginary parts of coupling coefficients between two coupled resonant modes in detail.

The imaginary part of coupling coefficient: The imaginary part of coupling measures the indirect interaction between the resonant modes, where photons radiated by one of the resonant modes coupled back to the other resonant modes through the continuum. This is often referred as real-photon interaction in quantum electrodynamics. In the absence of excitation light and absorption loss, the coupled mode equation for two coupled resonant modes is:

$$i\frac{d}{dt}\begin{pmatrix} a_1 \\ a_2 \end{pmatrix} = \begin{pmatrix} \omega_0 - i\gamma & 0 \\ 0 & \omega_0 - i\gamma \end{pmatrix}\begin{pmatrix} a_1 \\ a_2 \end{pmatrix} + \begin{pmatrix} 0 & \gamma_r + i\gamma_i \\ \gamma_r + i\gamma_i & 0 \end{pmatrix}\begin{pmatrix} a_1 \\ a_2 \end{pmatrix} \tag{12}$$

Here a_1 and a_2 are the resonant amplitudes. $|a_{1,2}|^2$ is normalized to represent the energy of the resonant modes. γ is the radiative decay rate of the resonant modes. The amplitudes of a resonant mode decays into the continuum due to coupling to outgoing plane waves. The radiating field can be described by the superposition of many plane waves. The amplitude of the plane wave propagating in the θ direction is given by:

$$S_{rad}(\theta) = \kappa_\theta \left(e^{i\frac{\pi\, sin(\theta) d}{\lambda}} \quad e^{-i\frac{\pi\, sin(\theta) d}{\lambda}} \right) \begin{pmatrix} a_1 \\ a_2 \end{pmatrix} \tag{13}$$

where κ_θ is the coupling rate of the resonant amplitude due to radiation to the continuum and $|S_{rad}|^2$ is the power. Each different multipolar mode will feature a different angular dependence for κ_θ. The units for κ_θ and $|S_{rad}|^2$ are 1/sec and W, respectively. The total power radiated by the coupled resonator system can be calculated by integrating the power radiated by all the plane waves as:

$$\begin{aligned} P_{rad} &= \int_{-\pi}^{\pi} d\theta\, S_{rad}^*(\theta) S_{rad}(\theta) \\ &= (a_1^* \quad a_2^*) \begin{pmatrix} \int_{-\pi}^{\pi} d\theta\, \kappa_\theta^* \kappa_\theta & \int_{-\pi}^{\pi} d\theta\, \kappa_\theta^* \kappa_\theta e^{-i\frac{2\pi\, sin(\theta) d}{\lambda}} \\ \int_{-\pi}^{\pi} d\theta\, \kappa_\theta^* \kappa_\theta e^{i\frac{2\pi\, sin(\theta) d}{\lambda}} & \int_{-\pi}^{\pi} d\theta\, \kappa_\theta^* \kappa_\theta \end{pmatrix} \begin{pmatrix} a_1 \\ a_2 \end{pmatrix} \\ &= (a_1^* \quad a_2^*) \begin{pmatrix} \int_{-\pi}^{\pi} d\theta\, \kappa_\theta^* \kappa_\theta & \int_{-\pi}^{\pi} d\theta\, \kappa_\theta^* \kappa_\theta \cos\left(\frac{2\pi\, sin(\theta)\, d}{\lambda}\right) \\ \int_{-\pi}^{\pi} d\theta\, \kappa_\theta^* \kappa_\theta \cos\left(\frac{2\pi\, sin(\theta)\, d}{\lambda}\right) & \int_{-\pi}^{\pi} d\theta\, \kappa_\theta^* \kappa_\theta \end{pmatrix} \begin{pmatrix} a_1 \\ a_2 \end{pmatrix} \end{aligned} \tag{14}$$

The diagonal term $\int_{-\pi}^{\pi} d\theta\, \kappa_\theta^* \kappa_\theta$ indicates the radiative decay rate γ of the resonant mode. The off-diagonal term $\int_{-\pi}^{\pi} d\theta\, \kappa_\theta^* \kappa_\theta \cos\left(\frac{2\pi\, sin(\theta) d}{\lambda}\right)$ quantifies the degree of overlap between the far-field radiation patterns from the two neighboring resonators.

On the other hand, the total radiation energy can also be calculated by examining the decay of energy in the resonators:

$$P_{rad} = -\frac{d}{dt}\left(\begin{pmatrix} a_1^* & a_2^* \end{pmatrix}\begin{pmatrix} a_1 \\ a_2 \end{pmatrix}\right) = -\left(\frac{d}{dt}\begin{pmatrix} a_1^* & a_2^* \end{pmatrix}\right)\begin{pmatrix} a_1 \\ a_2 \end{pmatrix} - \begin{pmatrix} a_1^* & a_2^* \end{pmatrix}\frac{d}{dt}\begin{pmatrix} a_1 \\ a_2 \end{pmatrix}$$

$$= -i\begin{pmatrix} a_1^* & a_2^* \end{pmatrix}\begin{pmatrix} \omega_0 + i\gamma^* & \gamma_r - i{\gamma_i}^* \\ \gamma_r - i{\gamma_i}^* & \omega_0 + i\gamma^* \end{pmatrix}\begin{pmatrix} a_1 \\ a_2 \end{pmatrix} + i\begin{pmatrix} a_1^* & a_2^* \end{pmatrix}\begin{pmatrix} \omega_0 - i\gamma & \gamma_r + i\gamma_i \\ \gamma_r + i\gamma_i & \omega_0 - i\gamma \end{pmatrix}\begin{pmatrix} a_1 \\ a_2 \end{pmatrix}$$

$$= \begin{pmatrix} a_1^* & a_2^* \end{pmatrix}\begin{pmatrix} \gamma + \gamma^* & -\gamma_i - {\gamma_i}^* \\ -\gamma_i - {\gamma_i}^* & \gamma + \gamma^* \end{pmatrix}\begin{pmatrix} a_1 \\ a_2 \end{pmatrix}$$

$$= \begin{pmatrix} a_1^* & a_2^* \end{pmatrix}\begin{pmatrix} 2\gamma & -2\gamma_i \\ -2\gamma_i & 2\gamma \end{pmatrix}\begin{pmatrix} a_1 \\ a_2 \end{pmatrix} \tag{15}$$

By comparing Eq. 15 and Eq. 14, it is straightforward to obtain:

$$\gamma = \frac{1}{2}\int_{-\pi}^{\pi} d\theta\, \kappa_\theta^* \kappa_\theta \tag{16a}$$

$$\gamma_i = -\frac{1}{2}\int_{-\pi}^{\pi} d\theta\, \kappa_\theta^* \kappa_\theta \cos\left(\frac{2\pi\, sin(\theta)\, d}{\lambda}\right) \tag{16b}$$

In order to calculate the imaginary part of coupling coefficients, it's necessary to obtain the far-field radiation pattern and the radiative decay rate γ of the resonant modes. As an example, we consider a pair of parallel nanowires as in the main text. The cross-sectional dimensions of the nanowires are 100 nm by 100 nm and the gap between them is also 100 nm. To make the discussion more concise, the refractive indices of the nanowires are fixed at $4 + j0.025$ and we assume they are embedded in free space. Each nanowire supports two degenerate TM modes at the same wavelength of 610 nm, i.e. the $|A_x\rangle$ and $|A_y\rangle$ modes. As shown in Fig. 4.14(a), the $|A_x\rangle$ mode is a magnetic dipole along the *x* axis, which can be clearly seen by its field profile (top panel). Its far-field ration pattern has a $\cos^2\theta$ shape (bottom panel). The radiative decay rate γ is obtained by measuring the full width at half maximum (FWHM) of the absorption spectrum. We excited the $|A_x\rangle$ mode by putting line current sources in a single nanowire and calculating the spectrum of the absorbed power from FDFD simulation. The line current sources are carefully distributed according to the mode profile. The radiative decay rate γ then is obtained as $\gamma = \frac{1}{2}FWHM - \gamma_a$, where the absorption rate γ_a can be calculated by integrating $\sigma(\omega)|E|^2$ in the structures where $\sigma(\omega)$ is the conductivity at the angular frequency ω and E is the electric field.

The decay rate $\kappa_{\theta x}$ for the $|A_x\rangle$ mode then is given by $\kappa_{\theta x} = \sqrt{\frac{2\gamma}{\pi}}\cos\theta$. The imaginary part of coupling coefficient for the $|A_x\rangle$ mode in our structures then can be calculated as:

$$\begin{aligned}\gamma_{ix} &= -\frac{1}{2}\int_{-\pi}^{\pi} d\theta\, \kappa_{\theta x}^{*}\kappa_{\theta x} \cos\left(\frac{2\pi\, sin(\theta)\, d}{\lambda}\right) \\ &= -\frac{\gamma}{\pi}\int_{-\pi}^{\pi} d\theta \cos^2\theta \cos\left(\frac{2\pi\, sin(\theta)\, d}{\lambda}\right) \qquad (17)\end{aligned}$$

On the other hand, the $|A_y\rangle$ mode is a magnetic dipole along the y axis, which can also be clearly seen by its field profile in Fig. 4.14(b). Its far-field radiation pattern has a $\sin^2\theta$ shape and its decay rate $\kappa_{\theta y}$ is given by $\kappa_{\theta y} = \sqrt{\frac{2\gamma}{\pi}}\sin\theta$. Similarly, the imaginary part of coupling coefficient for the $|A_y\rangle$ mode in our structures can be calculated as:

$$\begin{aligned}\gamma_{iy} &= -\frac{1}{2}\int_{-\pi}^{\pi} d\theta\, \kappa_{\theta y}^{*}\kappa_{\theta y} \cos\left(\frac{2\pi\, sin(\theta)\, d}{\lambda}\right) \\ &= -\frac{\gamma}{\pi}\int_{-\pi}^{\pi} d\theta \sin^2\theta \cos\left(\frac{2\pi\, sin(\theta)\, d}{\lambda}\right) \qquad (18)\end{aligned}$$

Note the imaginary part of coupling between the $|A_x\rangle$ mode and the $|A_y\rangle$ mode in different nanowires is zero, which can be directly shown as $\int_{-\pi}^{\pi} d\theta \sin\theta \cos\theta \cos\left(\frac{2\pi\, sin(\theta) d}{\lambda}\right) = 0$.

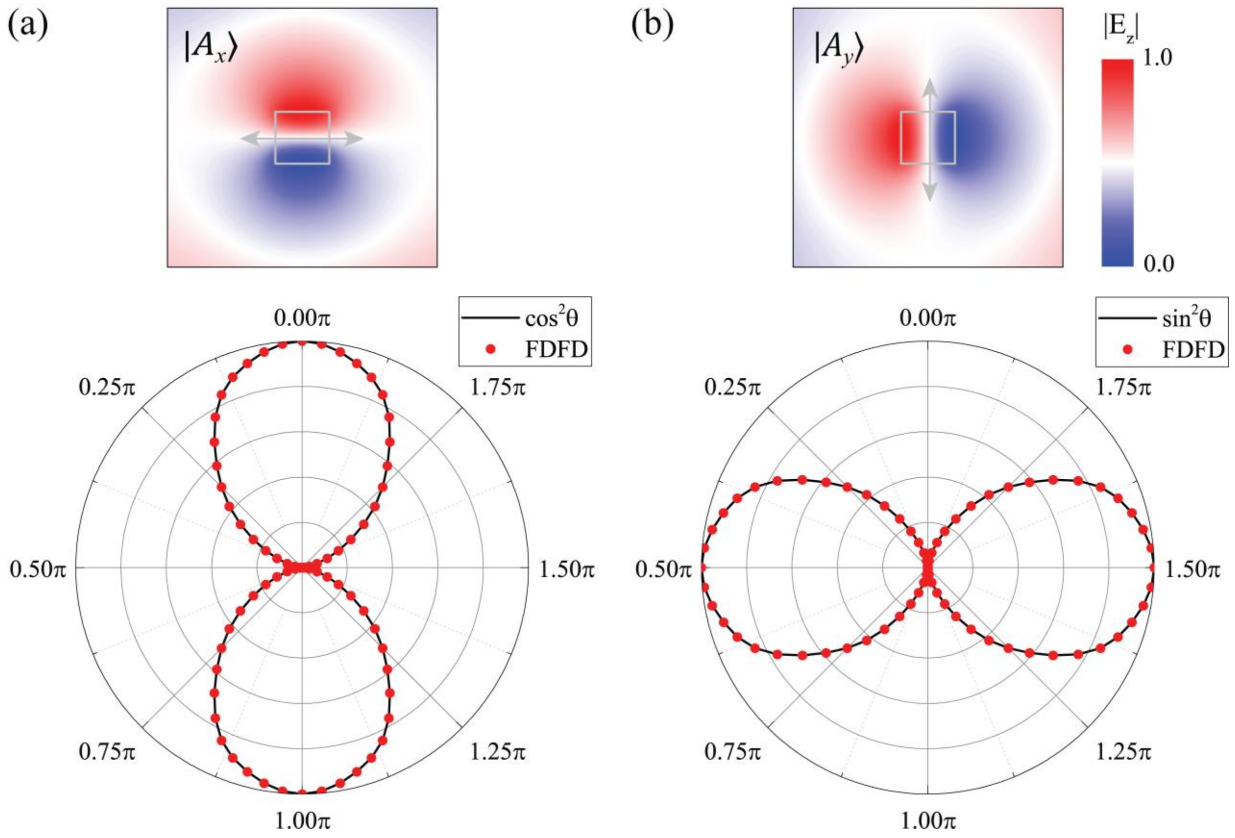

Fig. 4.14 Far-field radiation patterns for the $|A_x\rangle$ and $|A_y\rangle$ modes. (a) The $|A_x\rangle$ mode is a magnetic dipole in the *x* direction (gray arrow), whose electric field distribution is shown in the upper panel. Its far-field emission profile has a $cos^2\theta$ shape, which can be seen by comparing the analytic curve (black solid line) and FDFD simulation (red circles) in the lower panel. (b) The $|A_y\rangle$ mode is a magnetic dipole in the *y* direction (gray arrow), which has a $sin^2\theta$ shape far-field radiation profile.

The real part of coupling coefficient: The real part of coupling measures the direct interaction between the resonant modes, where the two resonant modes interact through virtual photons. The real part of coupling coefficient between two coupled modes can be directly calculated from the overlapping of the resonant field distribution, which is given by the following equation

$$\gamma_r = \frac{\omega_0}{4} \frac{\int\int dx_a dy_a\, \epsilon_a(x,y)\boldsymbol{E}_{\boldsymbol{a}}^*(x,y) \cdot \boldsymbol{E}_{\boldsymbol{b}}(x,y)}{\int_{-\infty}^{\infty}\int_{-\infty}^{\infty} dxdy\, |\boldsymbol{E}_{\boldsymbol{a}}(x,y)|^2} \tag{19}$$

Here $\boldsymbol{E}_{\boldsymbol{a}}(x,y)$ and $\boldsymbol{E}_{\boldsymbol{b}}(x,y)$ are the resonant electric field from wire a and b, respectively. $\epsilon(x,y)$ is the relative dielectric function with only wire a in the space. The integral in the numerator is performed within the volume of wire a.

The real part of coupling coefficient can be quantified by using Finite-Difference Frequency-Domain simulations of electric fields for the relevant resonant modes. These modes are excited by putting line current sources inside the nanowires (Fig. 4.15), where the line current sources are carefully distributed according to the mode profile. Then we perform the integral numerically to calculate the real part of coupling coefficients.

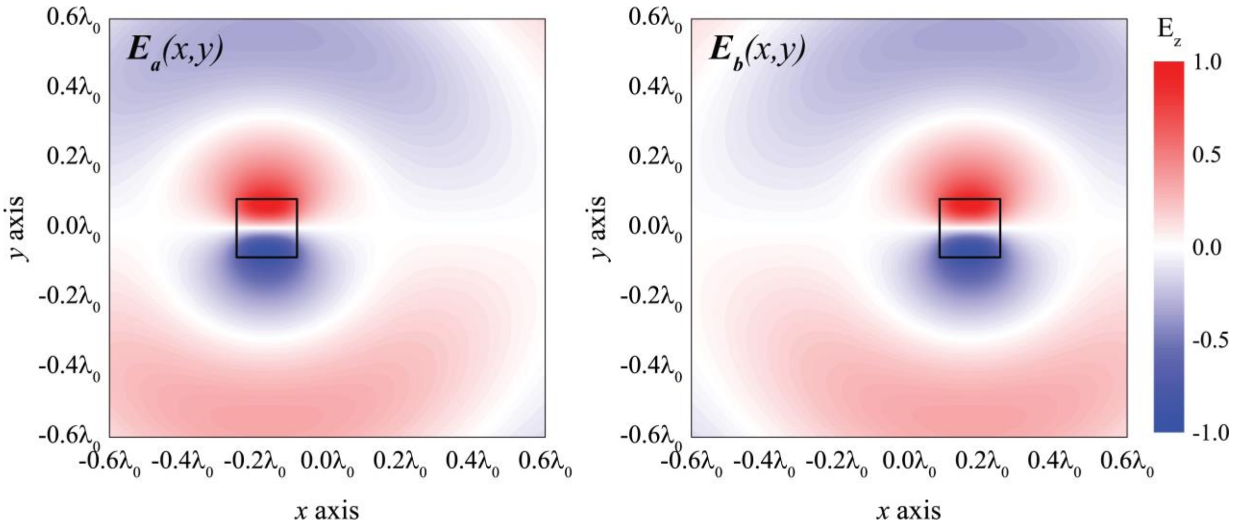

Fig. 4.15 Resonant electric field distributions for the modes near each wire. We plot the $|A_x\rangle$ mode as an example.

4.13 Coupled mode theory: derivation of the energy in coupled resonators in free space.

We will solve the coupled-mode equation described by Eq. 7 to obtain the energy in resonators under illumination from different incident angles. Under steady-state excitation with an angular frequency ω, Eq. 7 can be written as:

$$\begin{pmatrix} \omega - \omega_0 + i\gamma & -\gamma_r - i\gamma_i \\ -\gamma_r - i\gamma_i & \omega - \omega_0 + i\gamma \end{pmatrix} \begin{pmatrix} a_1 \\ a_2 \end{pmatrix} = i\kappa_\theta S(\theta) \begin{pmatrix} e^{-i\frac{\pi\, sin(\theta)d}{\lambda}} \\ e^{i\frac{\pi\, sin(\theta)d}{\lambda}} \end{pmatrix} \tag{20}$$

Therefore, we can get the resonance amplitude of the resonators as:

$$\begin{pmatrix} a_1 \\ a_2 \end{pmatrix} = i\kappa_\theta S(\theta) \begin{pmatrix} \omega - \omega_0 + i\gamma & -\gamma_r - i\gamma_i \\ -\gamma_r - i\gamma_i & \omega - \omega_0 + i\gamma \end{pmatrix}^{-1} \begin{pmatrix} e^{-i\varphi} \\ e^{i\varphi} \end{pmatrix}$$

$$= \frac{i\kappa_\theta S(\theta)}{(\omega - \omega_0 + i\gamma)^2 + (\gamma_r + i\gamma_i)^2} \begin{pmatrix} \omega - \omega_0 + i\gamma & \gamma_r + i\gamma_i \\ \gamma_r + i\gamma_i & \omega - \omega_0 + i\gamma \end{pmatrix} \begin{pmatrix} e^{-i\varphi} \\ e^{i\varphi} \end{pmatrix}$$

$$= \frac{i\kappa_\theta S(\theta)}{(\omega - \omega_0 + i\gamma)^2 + (\gamma_r + i\gamma_i)^2} \begin{pmatrix} (\omega - \omega_0 + i\gamma)e^{-i\varphi} + (\gamma_r - i\gamma_i)e^{i\varphi} \\ (\omega - \omega_0 + i\gamma)e^{i\varphi} + (\gamma_r - i\gamma_i)e^{-i\varphi} \end{pmatrix} \tag{21}$$

Here we define $\varphi = \frac{\pi\, sin(\theta)d}{\lambda}$ for simplification. The ratio between the resonator's energies then is:

$$\left|\frac{a_2}{a_1}\right|^2 = \frac{(\omega - \omega_0 + \gamma_i \sin 2\varphi + \gamma_r \cos 2\varphi)^2 + (\gamma + \gamma_i \cos 2\varphi - \gamma_r \sin 2\varphi)^2}{(\omega - \omega_0 - \gamma_i \sin 2\varphi + \gamma_r \cos 2\varphi)^2 + (\gamma + \gamma_i \cos 2\varphi + \gamma_r \sin 2\varphi)^2} \tag{22}$$

It's straightforward to see that the ratio is always 1 if there is no coupling between the resonators, *i.e.* $\gamma_i = 0$ and $\gamma_r = 0$.

4.14 Coupled mode theory for acoustic resonators

In this section, we show that coupled acoustic resonators also follow the same coupled mode theory. We follow the notation used in Ref [20]. Considering two identical acoustic resonators that are coupled to *N* scattering channels, the effective Hamiltonian is given by

$$\boldsymbol{H}_{eff} = \begin{pmatrix} E_0 & 0 \\ 0 & E_0 \end{pmatrix} - i\pi \sum_{n=1}^{N} \begin{pmatrix} V_n \\ V_n \end{pmatrix} \begin{pmatrix} V_n^* & V_n^* \end{pmatrix} \tag{23}$$

where E_0 is the eigenenergy of the resonator. $V_{1,n}$ and $V_{2,n}$ are the coupling coefficients of the 1st and 2nd resonator to the *n*th scattering channel, respectively.

The general solution to the effective Hamiltonian can be written as:

$$\psi = \chi_1\phi_1 + \chi_2\phi_2 + \sum_{n=1}^{N} f_n \tag{24}$$

Here ϕ_1 and ϕ_2 are the eigenfunctions in the 1st and 2nd resonators, respectively. χ_1 and χ_2 are resonance amplitudes, respectively. The general solution of waves in each scattering channel is written as a superposition of incoming and outgoing waves [20]:

$$f_n = p_n u_n(\xi) e^{ik_n\xi} + q_n u_n(\xi) e^{-ik_n\xi} \tag{25}$$

where p_n and q_n are the amplitudes of the incoming and outgoing waves, respectively. $u_n(\xi)$ is the eigen wavefunction in the *n*th scattering channel.

In order to find the resonance amplitudes χ_1 and χ_2, we can evaluate the scalar products$\langle \phi_m | \boldsymbol{H}_{eff} - E | \psi \rangle = 0$, where m = 1, 2. The scalar products lead us to a simple coupled mode equation for the resonance amplitudes χ_1 and χ_2. For the general case of two coupled acoustic resonators, it can be written in the matrix form as:

$$\begin{pmatrix} E_0 - E - i\pi g & 0 \\ 0 & E_0 - E - i\pi g \end{pmatrix} \begin{pmatrix} \chi_1 \\ \chi_2 \end{pmatrix} - i\pi \begin{pmatrix} 0 & g_c \\ g_c & 0 \end{pmatrix} \begin{pmatrix} \chi_1 \\ \chi_2 \end{pmatrix} = -i2\pi \begin{pmatrix} V_{inc} p_{inc} e^{i\varphi_1} \\ V_{inc} p_{inc} e^{i\varphi_2} \end{pmatrix} \tag{26}$$

where $g = \sum_{n=1}^{N} V_n V_n^*$ describes the total decay rate of the resonance to the scattering channels, and $g_c = \sum_{n=1}^{N} V_n V_n^* e^{i(\varphi_1 - \varphi_2)}$ describes the indirect interaction between the resonators through the scattering channels. φ_1 and φ_2 are the incident phase at the 1st and 2nd resonators, respectively. The interaction between coupled acoustic resonators is governed by an non-Hermitian Hamiltonian. This above equation shows that the wave coupling dynamics is the same for acoustic resonators and for optical waves (Eq. 7).

4.15 Conclusion

With this newly accessible information about the intrinsic properties of light, angle-sensing pixels can be created for imaging chips that enable a wide variety of new applications for advanced light sensing.

For example, light-field cameras, which can adjust the focus after a photo is taken, use a micro-lens-array [1] or integrated gratings [35] to measure incident angles. These micro-lenses degrade the resolution while increasing the cost. The proposed subwavelength angle-sensing pixels could replace the micro-lenses to increase the resolution and to reduce cost.

In addition, as we demonstrate in the depth-sensing experiment, the angular information of light may also provide better scene awareness for autonomous systems such as self-driving cars and sun-tracking solar panels. Furthermore, electrically-isolated and optically-coupled photodetectors could further be made to perform multi-modal sensing for polarization and wavelength.

These light sensors extract highly specific information from the environment and could become pervasive in next-generation smart optoelectronic systems.

References

[1] Ng, R. *et al*. Light field photography with a hand-held plenoptic camera, *Stanford Univ. C.S. Tech report CSTR 2005-02* (2005).

[2] Wang, A., Gill, P. & Molnar, A. Light field image sensors based on the Talbot effect. *Appl. Opt.* **48,** 5897–5905 (2009).

[3] Wang, A., Gill, P. & Molnar, A. Angle sensitive pixels in CMOS for lensless 3D imaging. *Proc. Cust. Integr. Circuits Conf.* 371–374 (2009). doi:10.1109/CICC.2009.5280840

[4] Sivaramakrishnan, S., Wang, A., Gill, P. R. & Molnar, A. Enhanced Angle Sensitive Pixels for Light Field Imaging. *2011 IEEE Int. Electron Devices Meet.* 191–194 (2011).

[5] Grothe, B., Pecka, M. & McAlpine, D. Mechanisms of sound localization in mammals. *Physiol. Rev.* **90,** 983–1012 (2010).

[6] Pollack, G. S. Sensory cues for sound localization in the cricket Teleogryllus oceanicus: interaural difference in response strength versus interaural latency difference. *J. Comp. Physiol. A Neuroethol. Sens. Neural. Behav. Physiol.* **189,** 143–151 (2003).

[7] Chung, S.-H., Pettigrew, A. & Anson, M. Dynamics of the amphibian middle ear. *Nature* **272,** 142–147 (1978).

[8] Miles, R. N., Robert, D. & Hoy, R. R. Mechanically coupled ears for directional hearing in the parasitoid fly Ormiaochracea. *J. Acoust. Soc. Am.* **98,** 3059–3070 (1995).

[9] Römer, H. & Schmidt, A. K. D. Directional hearing in insects with internally coupled ears. *Biol. Cybern.* **110,** 247–254 (2016).

[10] Christensen-Dalsgaard, J. & Manley, G. A. Directionality of the lizard ear. *Journal of Experimental Biology* **208,** 1209–1217 (2005).

[11] Christensen-Dalsgaard, J., Tang, Y. & Carr, C. E. Binaural processing by the gecko auditory periphery. *J. Neurophysiol.* **105,** 1992–2004 (2011).

[12] Vossen, C., Christensen-Dalsgaard, J. & Hemmen, J. L. van. Analytical model of internally coupled ears. *J. Acoust. Soc. Am.* **128,** 909–918 (2010).

[13] Vedurmudi, A. P. *et al.* How internally coupled ears generate temporal and amplitude cues for sound localization. *Phys. Rev. Lett.* **116,** 28101 (2016).

[14] Mie, G. Beiträge zur Optik trüber Medien, speziell kolloidaler Metallösungen. *Ann. Phys.* **330,** 377–445 (1908).

[15] Cao, L. *et al.* Engineering light absorption in semiconductor nanowire devices. *Nat Mater* **8,** 643–647 (2009).

[16] Kuznetsov, A. I., Miroshnichenko, A. E., Brongersma, M. L., Kivshar, Y. S. & Luk'yanchuk, B. Optically resonant dielectric nanostructures. *Science* **354,** 2472 (2016).

[17] Suh, W., Wang, Z. & Fan, S. Temporal coupled-mode theory and the presence of non-orthogonal modes in lossless multimode cavities. *IEEE J. Quantum Electron.* **40,** 1511–1518 (2004).

[18] Verslegers, L., Yu, Z., Catrysse, P. B. & Fan, S. Temporal coupled-mode theory for resonant apertures. *Journal of the Optical Society of America B* **27,** 1947 (2010).

[19] Verslegers, L., Yu, Z., Ruan, Z., Catrysse, P. B. & Fan, S. From electromagnetically induced transparency to superscattering with a single structure: A coupled-mode theory for doubly

resonant structures. *Phys. Rev. Lett.* **108,** 83902 (2012).

[20] Maksimov, D. N., Sadreev, A. F., Lyapina, A. A. & Pilipchuk, A. S. Coupled mode theory for acoustic resonators. *Wave Motion* **56,** 52–66 (2015).

[21] Scully, M. O. Collective Lamb Shift in Single Photon Dicke Superradiance. *Phys. Rev. Lett.* **102,** 143601 (2009).

[22] Zhang, S. *et al.* Anti-Hermitian Plasmon Coupling of an Array of Gold Thin-Film Antennas for Controlling Light at the Nanoscale. *Phys. Rev. Lett.* **109,** 193902 (2012).

[23] Dicke, R. H. Coherence in Spontaneous Radiation Processes. *Phys. Rev.* **93,** 99–110 (1954).

[24] Lyuboshitz, V. L. Resonance Interaction between Two Identical Dipole Emitters, Soviet Physics JETP, **26,** 937-942 (1968)

[25] Makhmetov, G. E., Borisov, A. G., Teillet-Billy, D. & Gauyacq, J. P. Interaction Between Overlapping Quasi-Stationary States: He(2 1 S and2 1 P) Levels in Front of an Aluminium Surface. *EPL Europhys. Lett.* **27,** 247 (1994).

[26] Okołowicz, J., Płoszajczak, M. & Rotter, I. Dynamics of quantum systems embedded in a continuum. *Phys. Rep.* **374,** 271–383 (2003).

[27] Brönstrup, G. *et al.* Optical properties of individual silicon nanowires for photonic devices. *ACS NANO* **4**, 7113-7122 (2010).

[28] Cao, L. Fan, P. & Brongersma, M. L. Optical coupling of deep-subwavelength semiconductor nanowires. *Nano Lett.* **11**. 1463-1468 (2011).

[29] Zhou, M., Shi, L., Zi, J. & Yu, Z. Extraordinarily large optical cross section for localized single nanoresonator. *Phys. Rev. Lett.* **115,** 23903 (2015).

[30] Behdad, N., Al-Joumayly, M. & Li, M. Biomimetic electrically small antennas. *Electron. Lett.* **46,** 1650–1651 (2010).

[31] Besl, P. J. Active, optical range imaging sensors. *Mach. Vis. Appl.* **1,** 127–152 (1988).

[32] Blais, F. Review of 20 Years of range sensor development. *J. Electron. Imaging* **13,** (2004).

[33] Hill, K. G. & Boyan, G. S. Sensitivity to frequency and direction of sound in the auditory system of crickets (Gryllidae). *J. Comp. Physiol.* **121,** 79–97 (1977).

[34] ON Semiconductor, NOIV1SN025KA - VITA 25K Image Sensor Data Sheet, 2016 Rev.10, http://www.onsemi.com/pub/Collateral/NOIV1SN025KA-D.PDF

[35] Wang, A. & Molnar, A. A light-field image sensor in 180 nm CMOS. *IEEE J. Solid-State Circuits* **47,** 257–271 (2012).

CHAPTER FIVE

CMOS IMAGE SENSOR INTEGRATED WAVEFRONT SENSOR

5.1 Introduction

Wavefront sensors are detectors that sense the wavefront of an incident light. Wavefront is an equiphase surface of a time varying electromagnetic wave [1]. In other words, a collection of all points in space having identical phase. Ideal waves such as spherical waves and plane waves have a well-known wavefront shape throughout the space which is not much of an interest. However, in reality, such an ideal wavefronts can be easily distorted due to an anisotropic property of a medium. This is a common issue encountered in astronomical telescopes where light emitted from a star goes through an atmospheric aberration as it enters the atmosphere of the earth [2]. As a result, it is difficult to achieve a stable focus of a star using a telescope. In an adaptive optics system, wavefront sensors can be used to detect the atmospheric aberration of a wavefront and this aberration information can be used to reconstruct an image that is computationally focused [3].

Shack-Hartmann wavefront sensor [4, 5] is one of the conventional sensors that is widely used for wavefront detection. Basic schematic of Shack-Hartmann wavefront sensor is shown in Fig. 5.1(a). It uses a lenslet array where each lenslet is used to focus the local incident light at the focal plane. A photodetector, typically CMOS image sensor is placed at the focal plane. Multiple pixels (usually hundreds or thousands of pixels) are occupied under each lenslet. Since the location where the local incident light will be focused upon the image sensor surface depends on the incident angle, local wavefront can be determined by analyzing the intensity distribution of image sensor pixels [4, 5]. This method however suffers from low resolution since multiple pixels are used to retrieve a single measurement point of local incident angle.

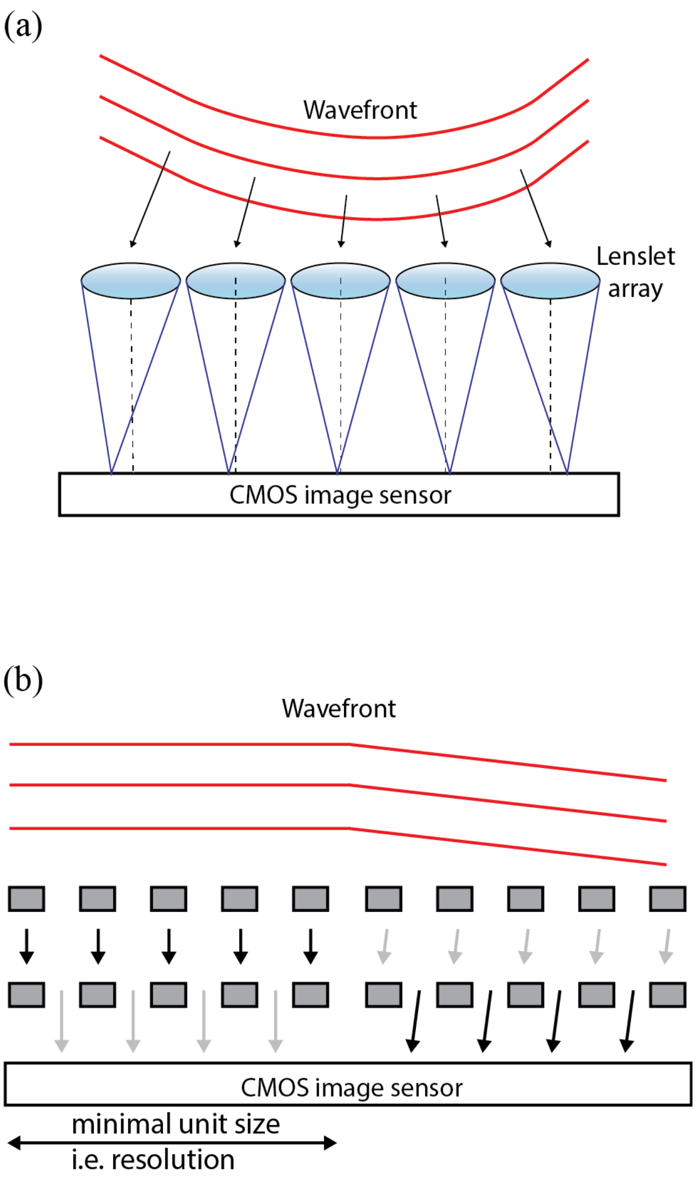

Fig. 5.1. (a) Schematic of Shack-Hartmann wavefront sensor. Lenslet arrays are used to focus the incident light at the image sensor plane. (b) Schematic of wavefront sensor based on gratings. Light intensity at image sensor plane is incident angle dependent.

Another method of detecting the wavefront is based on gratings [6, 7] as shown in Fig. 5.1(b). This method utilizes the Talbot effect [8]. Light passing through periodic structures such as gratings can generate an image of the periodic structures. The image will be angle dependent meaning that the light intensity distribution is also angle dependent. Thus, the light intensity will be a function of incident angle which eventually can be used to map out the wavefront.

However, there is a critical drawback for these existing methods. The drawback of these existing methods is the low spatial resolution. Under a single lenslet of Shack-Hartmann wavefront detector (Fig. 5.1(a)), hundreds or thousands of image sensor pixels are occupied. Typically, the diameter of lenslets for commercial Shack-Hartmann wavefront detectors range from 150 μm – 300 μm. This means that the spatial resolution of wavefront detection is 150 μm – 300 μm.

Gratings as in Fig. 5.1(b) require multiple elements to behave as a periodic structure. In addition, multiple arrangement of grating are required to figure out the incident angle of light in 3D space. This leads to a spatial resolution of tens of micron for wavefront detection.

Now, the problem with these low spatial resolution is that they will fail to detect a rapidly changing wavefront. Figure 5.2 shows an example of wavefronts having two different kind of aberration. It is clear that the wavefront in Fig. 5.2(a) and (b) are different. However, if the spatial resolution of the detector is not high enough, it will fail to capture this aberration and recognize as if these two wavefronts are identical even though they are clearly different.

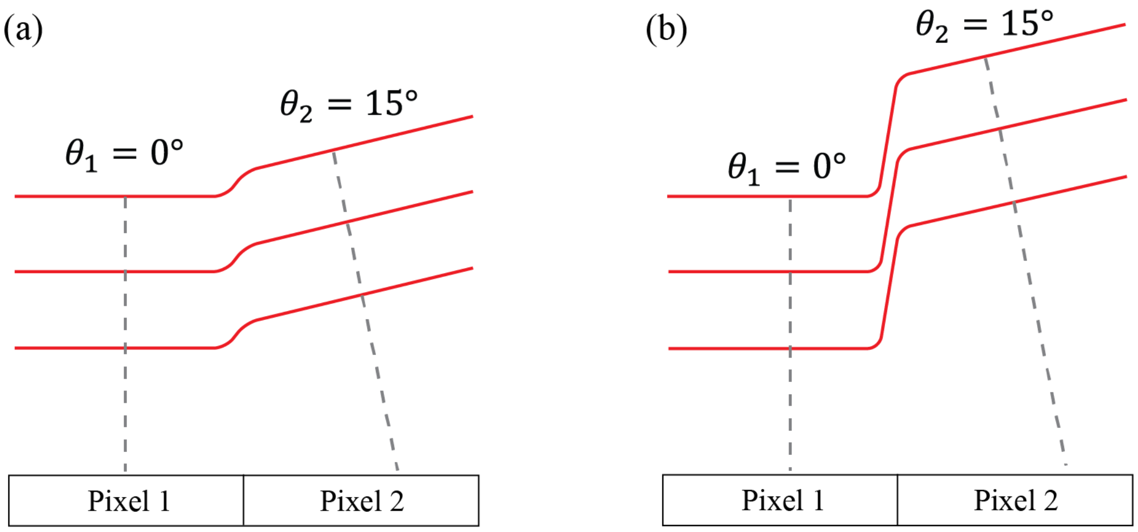

Fig. 5.2. Drawback of a low spatial resolution for wavefront detection. Both detectors at (a) and (b) are not able to sense the rapid wavefront change (red line). Thus, they are not able to tell the wavefront difference between (a) and (b).

Our proposed wavefront sensor, on the other hand, can greatly boost its resolution compared to conventional wavefront sensors since it does not require multiple pixels to extract angle information. In fact, it only requires 4 pixels of image sensor to measure the incident angle. These 4 pixels will read the actual relative phase difference with respect to the adjacent 4 pixel enabling every pixels contribute to the wavefront detection. This can be achieved since our proposed wavefront sensor does not rely on lenslet array nor gratings. Thus it does not require large spatial region to acquire one measurement point.

5.2 Angle sensing pixels

In a microscopic view, plane of wavefront is perpendicular to the incident angle direction. Thus, a collection of incident angles across the region can be used to calculate the wavefront of incident light. In our method, the first step is to design an image sensor which can detect the incident angle of light. This can be done by utilizing two neighboring pixels in a CMOS image sensor.

Figure 5.3 describes how the local incident angle can be detected using a CMOS image sensor. Imagine a bare CMOS image sensor with array of pixels. Individual pixels will absorb same amount of light regardless of the incident angle of an incoming light as shown in Fig. 5.3(a) and (b). It can be understood as a unit cell with a single pixel having a periodic boundary condition. No matter which direction the light is coming from, every individual pixels will have identical absorption of light.

However, once we place a mask on top of a CMOS image sensor, the angle independency of light absorption disappears. Figure 5.3(c) and (d) shows the mechanism of this technique. For a normal incident light, both pixels (pixel 1 and pixel 2) will absorb identical amount of light as shown in Fig. 5.3(a). However, when the light is oblique incident, light absorption of two neighboring pixels will not be identical as depicted in Fig. 5.3(b). This is because the mask on top of the image sensor blocks a partial region of pixels creating an unequal light absorption between neighboring pixels. As a matter of fact, the ratio of light absorption between two neighboring pixels can be expressed as a function of incident angle (θ).

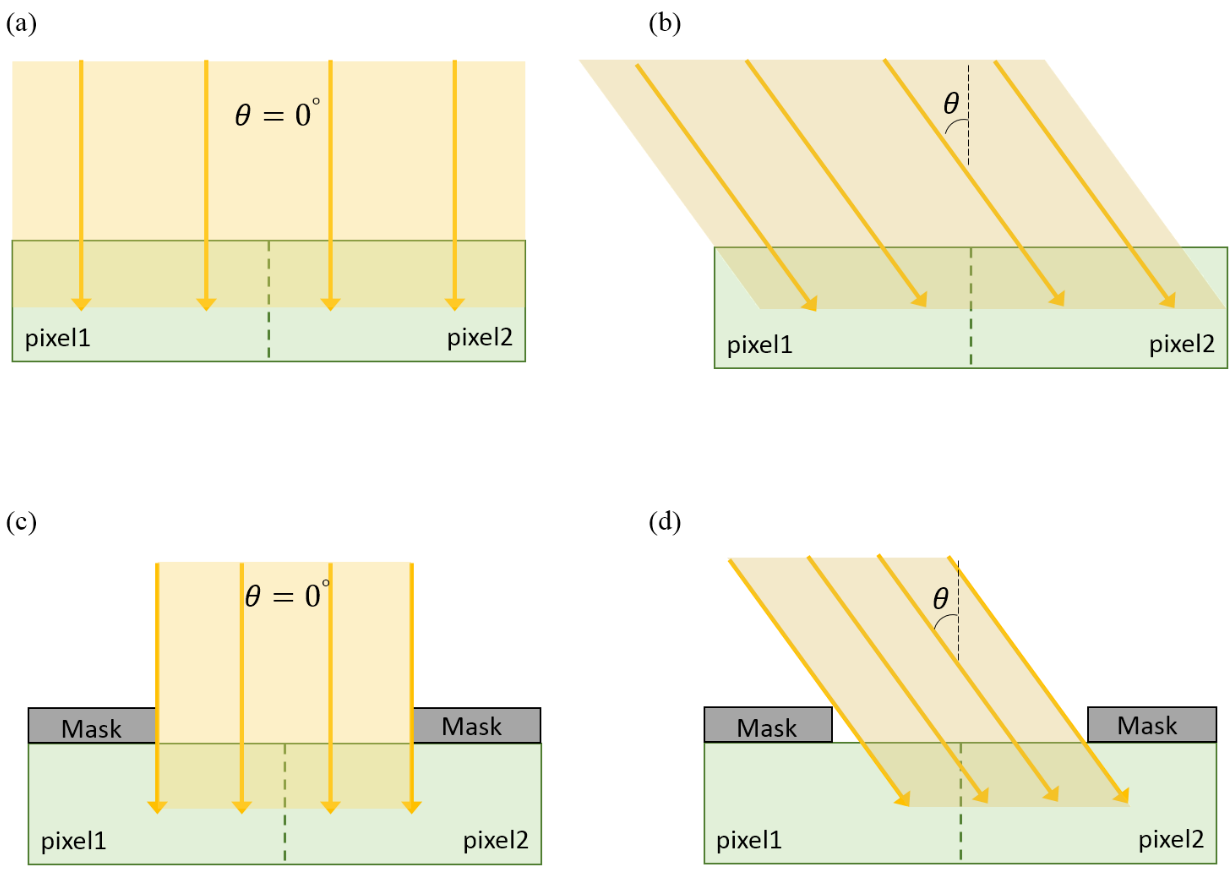

Fig. 5.3. (a) For normal incidence case, two neighboring pixels will absorb the same amount of light regardless of the incident angle of light. (b) With a mask on top of the pixels, light absorption ratio between two neighboring pixels are different and it becomes angle (θ) dependent.

Figure 5.4(a) is a plot showing an absorption ratio between two neighboring pixels with a mask on top versus the incident angle of light. For a normal incident case ($\theta = 0°$), light absorption in both pixels are identical thus the light absorption ratio between two neighboring pixels (P2/P1) is 0. This directly refers to the case shown in Fig. 5.3(c). However, as θ increases, pixel 2 will start to absorb more light than pixel 1 due to the shadowing effect of the mask and P2/P1 will start to increase. This refers to the case shown in Fig. 5.3(d). When $\theta = 30°$, P2/P1 reaches almost 2 meaning that the light absorption of pixel 2 (pixel further away from the incident light) has twice more of light absorption than the pixel 1 which is closer to the incident light. It is clear that the incident angle of light can be mapped out from the ratio (P2/P1) plot.

Figure 5.4(b)-(d) shows a gray scale image of an image sensor pixel intensity for three different incident angles A, B, and C which is depicted in Fig. 5.4(a). Black color corresponds to no light absorption and white color corresponds to the maximum intensity (saturation) of a pixel. As the incident angle increases, the contrast difference between two pixels increase. For angle detection, this method is valid in 2D space. However, we can extend this idea to measure the incident angle of light in 3D space.

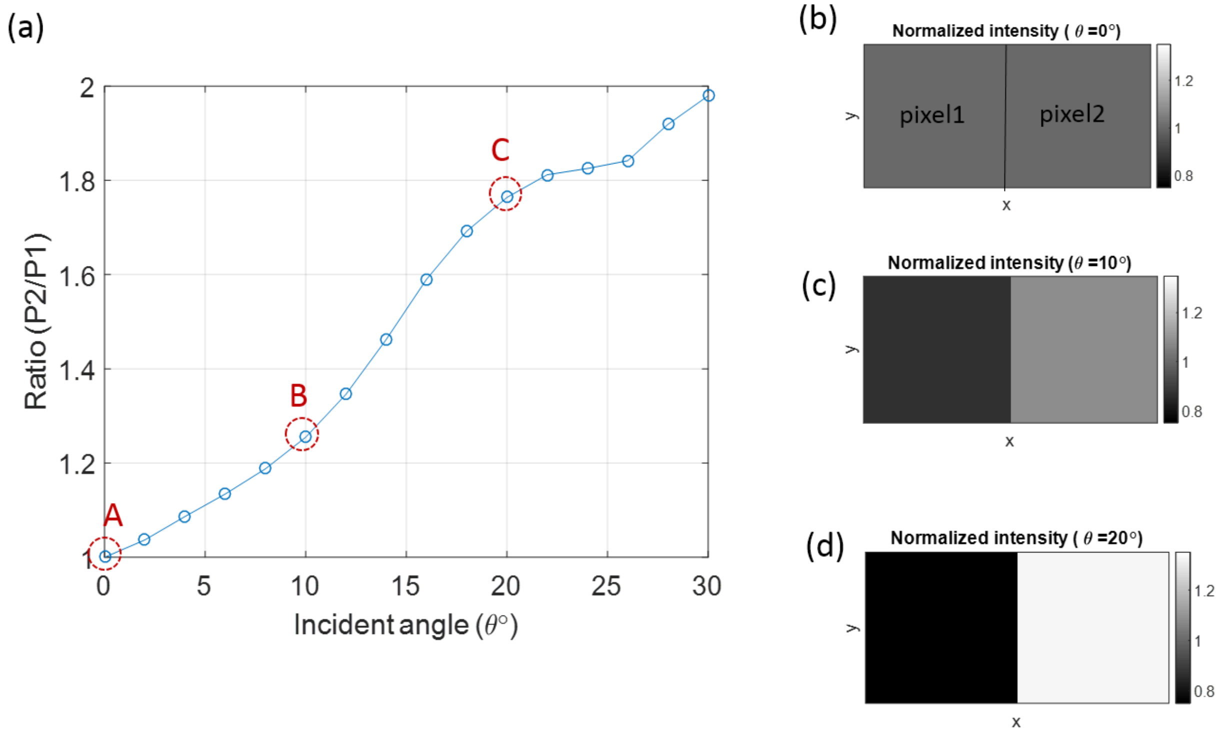

Fig. 5.4. (a) Absorption ratio of two neighboring pixels versus the incident angle of light. (b) - (d) Gray scale image of pixel brightness for three different incident angles A ($\theta = 0°$), B ($\theta = 10°$), and C ($\theta = 20°$) as depicted in (a).

5.3 Angle sensing in 3D Space

Extending the idea mentioned in the previous section, 4 pixels in a 2 by 2 element arrangement can be used to detect the incident angle in 3D space. Figure 5.5 shows a schematic of a unit cell that can detect the incident angle of light in 3D space. It consists of 4 pixels with a mask on top of the pixels which has an opening. The purpose of the mask is to block the incident light (yellow arrow). Thus, the mask can be any type of material which will reflect the incident light. For this research, 100nm of Al was deposited on top of image sensor to be used as a mask. The opening of the mask i.e. aperture lets the light reach 4 pixels. By comparing light absorption ratio between two pixels, incident angle can be extracted. There are 6 different ratios which can be analyzed. P1/P2, P2/P4, P4/P3, P3/P1, P1/P4 and P2/P3. Although a single ratio mapping, e.g. P1/P2 will show an angle ambiguity in 3D space for angle sensing, analyzing all 6 ratios enables to retrieve the incident angle of light in 3D space.

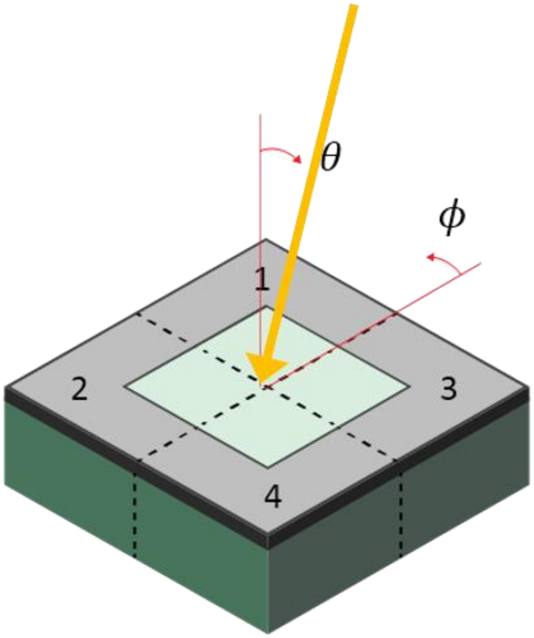

Fig. 5.5. Unit cell with 4pixels as 2 by 2 element arrangement which can be used to detect the incident angle of light in 3D space. Yellow arrow represents an incident angle of light. Green color represents pixels in an image sensor, and gray color represents a metallic mask.

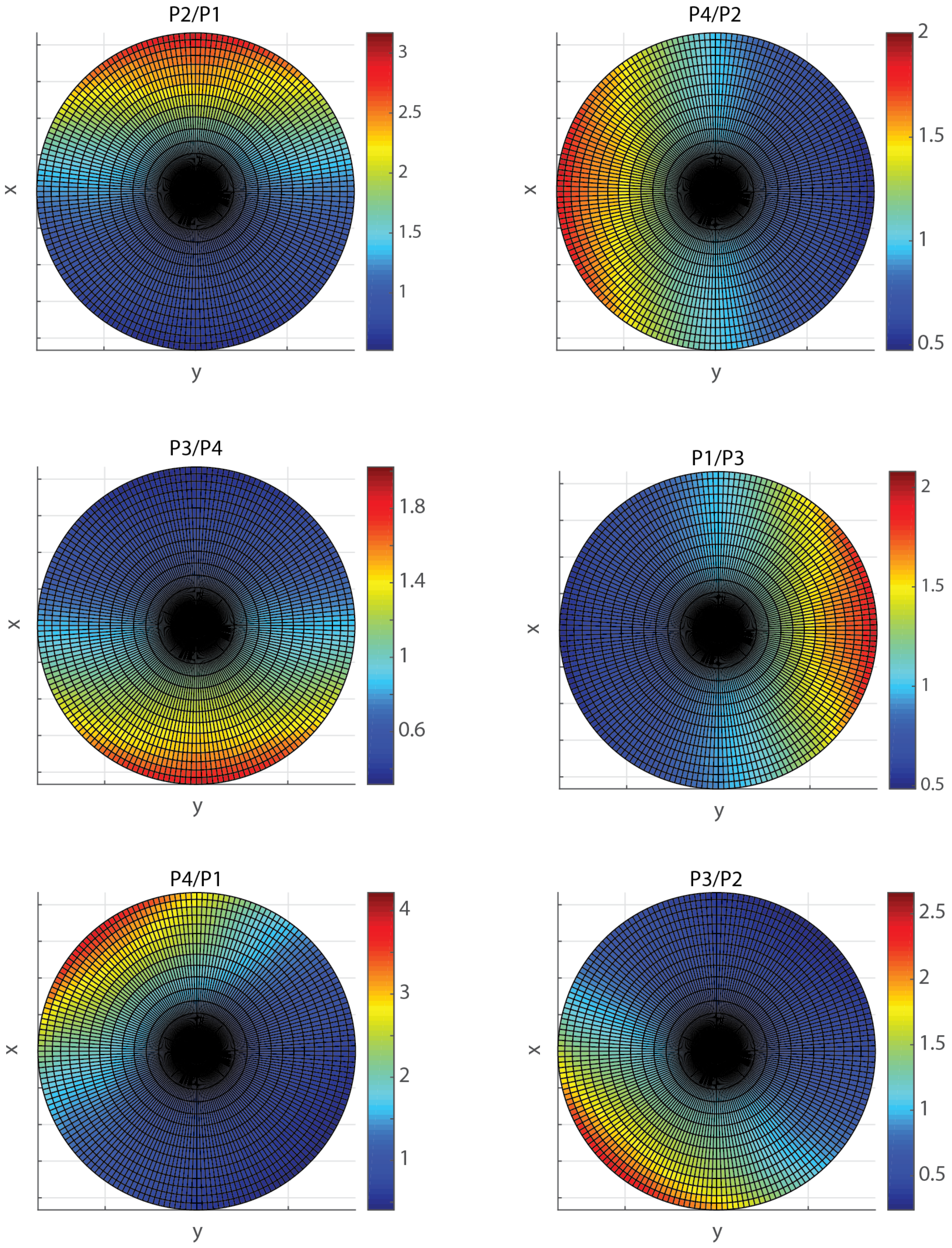

Fig. 5.6. Calibration map of absorption ratio versus incident angle of a unit cell for all 6 possible ratio combinations.

Figure 5.6 shows the calibration map of an absorption ratio versus incident angle for all 6 possible ratio combinations for a unit cell that is shown in Fig. 5.3. This plot can be understood using polar coordinates. The center of the circle corresponds to the normal incident case, i.e. $\theta = 0°$. The most outer side of the circle corresponds to $\theta = 30°$ case. $\phi = 0°$ along the x-axis for all positive x values. $\phi = 90°$ along the y-axis for all positive y values and same goes on for ϕ reaching all the way up to $360°$. Note that 6 ratio plots show different angular response for a certain incident angle. For example, when $\theta = 0°$, all 6 ratios will be 1. However, when $\theta \neq 0°$, 6 ratio maps will designate to different ratio values. Thus, this calibration map can be used to get rid of the angle ambiguity and determine the incident angle of light in 3D space. Having an array of unit cell in Fig. 5.5, collection of local incident angles can be retrieved and this information can be used to calculate the wavefront of the incident light. In others words, the proposed wavefront sensor is basically a periodic structure having a unit cell as shown in Fig. 5.5.

5.4 Fabrication of wavefront sensor

Figure 5.7(a) shows a microscope image of a fabricated wavefront sensor. Four neighboring pixels which consist a unit cell are surrounded with a metal (Al) mask. These unit cells are distributed as a periodic structure in a 2D plane. Photo-lithography is used to pattern the mask. The metal mask is deposited on top of CMOS image sensor using electron beam evaporation using Aluminum as a source material. Lift-off process will finalize the shape of the mask as shown in Fig. 5.7(a). CMOS image sensor used for this research has a 5.2 μm pixel size. Thus the size of the unit cell is 10.4 μm. This means that the spatial resolution of the wavefront detector is 10.4 μm assuming direct project of the wavefront without any magnification.

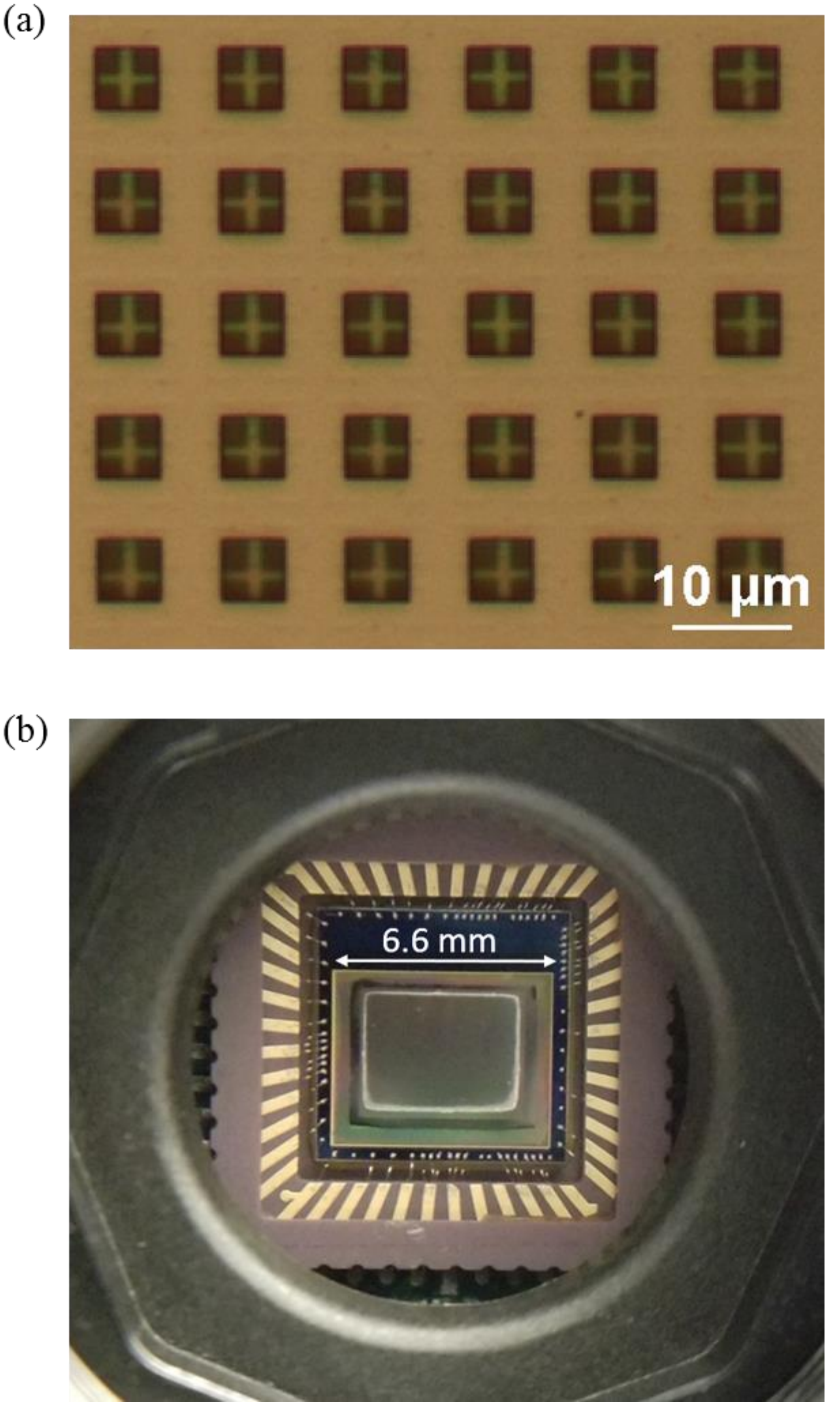

Fig. 5.7. (a) Microscope image of a fabricated wavefront sensor showing an array of unit cells. Pixel size of the image sensor is 5.2 μm and the unit cell size is 10.4 μm. (b) Fabricated wavefront sensor mounted on a chip and a black plastic body.

Figure 5.7(b) shows the fabricated wavefront sensor mounted on a chip covered by a black plastic body. Dimension of the active pixels in the horizontal direction is 6.6 mm. However, now all regions are covered with a mask due to a fabrication process. We believe the whole active pixel area can be easily covered with a mask under a standard CMOS fabrication process.

5.5 Wavefront measurement in 3D Space

We demonstrate the performance of our wavefront sensor by capturing a wavefront of a diverging beam at three different locations. Figure 5.8(a) shows the overall measurement setup. Collimated light having 550 nm wavelength is used for the light source. A biconvex lens with a focal length of 25 mm is used to focus the beam. Once the beam passes the focal point, it will diverge generating a diverging wavefront. Diverging beam has a spherical wavefront where the curvature of the wavefront corresponds to the distance from the focal point to the point of interest beyond the focal point. For our measurement, wavefront was captured at three different locations A, B and C as depicted in Fig. 5.8 (a). The distance from the focal point to curvature A, B and C are 2 mm, 4 mm and 6 mm respectively. Wavefront was reconstructed using zonal estimation [9].

Figure 5.8 (b) shows the reconstructed wavefronts at three different locations A, B and C. As it can be seen, the radius of the curvature will increase as the wavefront is captured further away from the focal point of the lens.

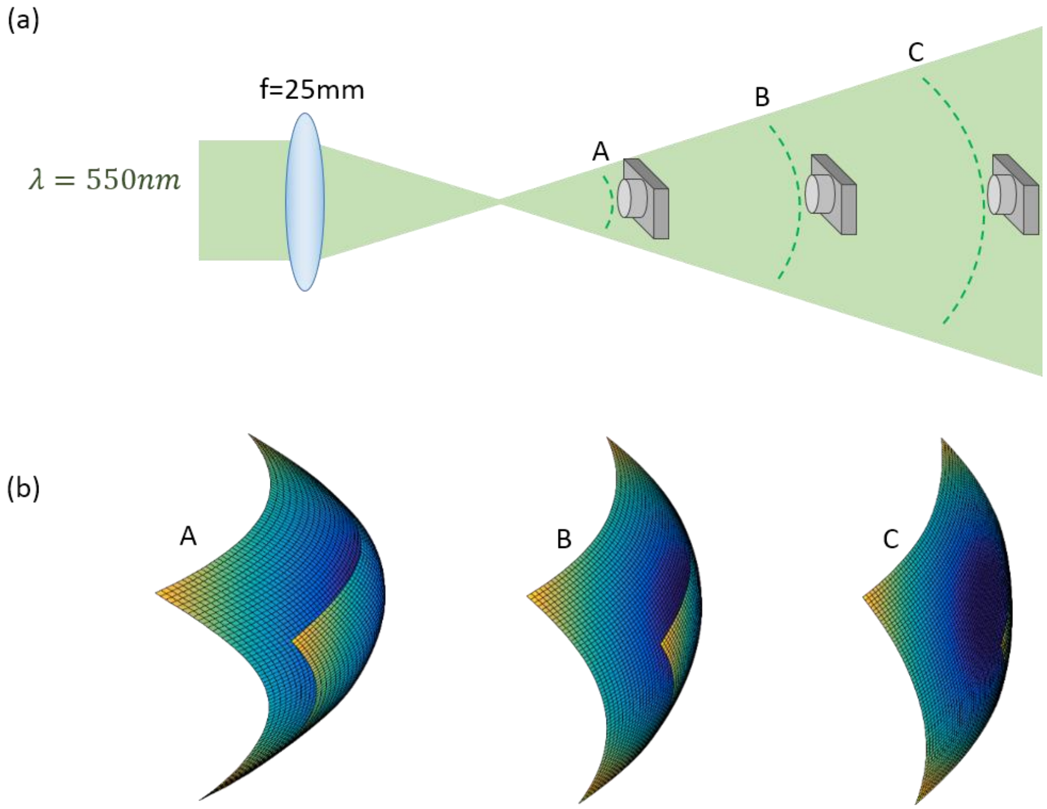

Fig. 5.8. (a) Measurement setup for capturing the wavefront of a diverging beam at three different locations A, B and C. A biconvex lens is used to generate a diverging wave beyond the focal point. (b) Reconstructed wavefront at three different positions A, B and C. Wavefront have larger radius of curvature as the wavefront is captured further away from the focal point.

The proposed wavefront detector can not only detect a spherical wavefront but also an arbitrarily shaped wavefront. In order to demonstrate this, we will measure a wavefront generated from a test sample which has a drop of PMMA on top of a quartz piece. A drop of PMMA was baked for 3min at 180 degree under a hot plate. The 4f-system was used to project the wavefront of the test sample to the wavefront sensor as shown in Fig. 5.9. The object plane is setup to have the PMMA layer. This object plane will consists of the wavefront which is aberrated due to the random thickness of a PMMA layer. The 4f-system is setup so that the wavefront sensor is located at the image plane. Measuring the wavefront at the image plane can determine the wavefront at the object plane which is inverted due to the lens.

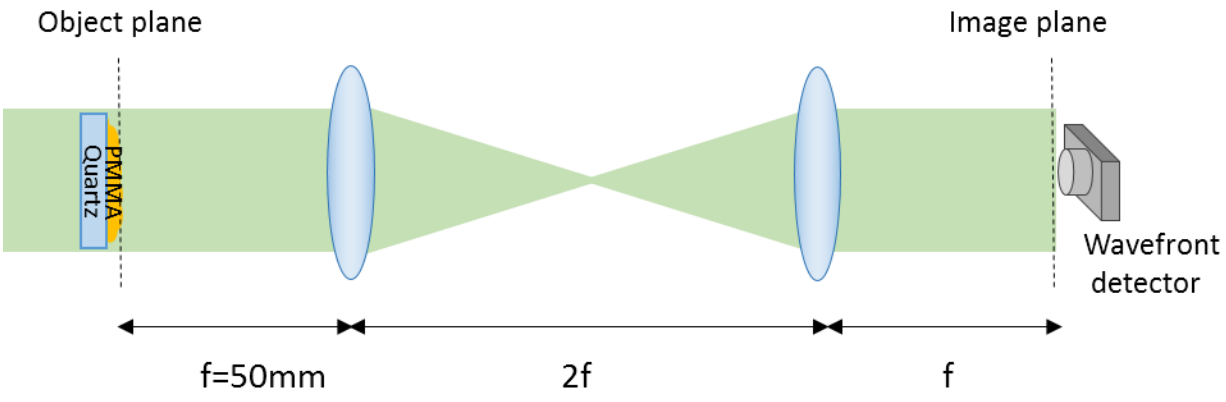

Fig. 5.9. The 4f- system used to measure the wavefront aberration caused from the PMMA layer. PMMA layer is located at the object plane and the wavefront sensor is located at the image plane.

Figure 5.10(a) shows a reconstructed wavefront at the image plane using the proposed wavefront sensor. Due to the random thickness of a PMMA layer at the object plane, the wavefront is not a plane wave but an aberrated wavefront. The spatial resolution of the reconstructed wavefront is 10.4 μm which is only twice the size of an image sensor pixel size.

In order to compare our result with an existing wavefront sensor, we plot the identical wavefront measured by a commercial Shack-Hartmann wavefront sensor at Fig. 5.10(b). This measurement result was acquired under the same optical setup as in Fig. 5.9. The diameter of lenslet used in Shack-Hartmann wavefront sensor was 150 μm. It is clear that our device has much higher spatial resolution (almost 15 time higher) compared to Shack-Hartmann wavefront sensor. The result in Fig. 5.10(b) does not have the details of the aberrated wavefront as in Fig. 5.10(a) due to a much lower spatial resolution.

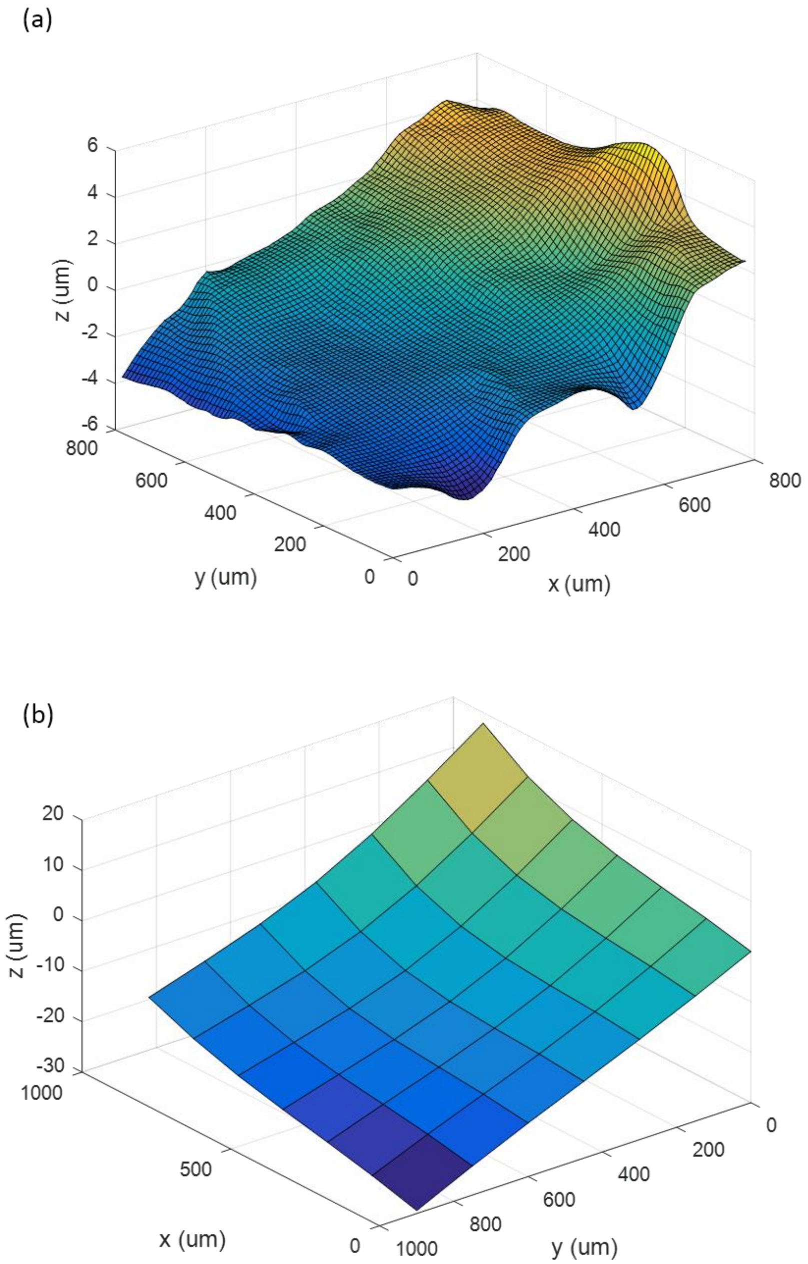

Fig. 5.10 (a) Wavefront captured using our wavefront sensor. (b) Wavefront captured using a commercial Shack-Hartmann wavefront detector.

Note that there are only 49 measurement points in Fig. 5.10(b) which used a Shack-Hartmann wavefront detector for the wavefront measurement while there are more than 5,000 measurement points in Fig. 5.10(a) which used our wavefront detector for the measurement. Thus the proposed wavefront sensor is possible to capture much more details of the aberrated wavefront than a commercial Shack-Hartmann wavefront sensor.

5.6 Conclusion

The proposed wavefront detector has a very high resolution which is an order of magnitude higher than a commercial Shack-Hartmann wavefront detector. This is possible since we are not relying on lenslet array nor gratings to measure the wavefront. Instead, 4 neighboring pixels of an imaging sensor with a mask on top (unit cell) is used to detect local incident angle. Array of this unit cell is capable of measuring the wavefront with a spatial resolution that is much higher than a commercial wavefront detector. The cost of manufacturing for the proposed wavefront sensor is expected to be low since it only requires one additional mask layer on top of a commercial CMOS image sensor. As a result, mass production is expected to be easy under a low manufacturing cost. The high spatial resolution of the proposed wavefront sensor is expected to enhance the performance of adaptive optics when integrated with adaptive optics system.

References

[1] P. M. Whelan and M. J. Hodgson, *Essential Principles of Physics*, 2nd edition. London: John Murray, 1978.

[2] J. M. Beckers, “Adaptive Optics for Astronomy: Principles, Performance, and Applications,” *Annu. Rev. Astron. Astrophys.*, vol. 31, no. 1, pp. 13–62, 1993.

[3] R. K. Tyson, *Principles of Adaptive Optics, Second Edition*, 2 edition. Boston: Academic Press, 1997.

[4] B. C. Platt and R. Shack, “History and principles of Shack-Hartmann wavefront sensing,” *J. Refract. Surg. Thorofare NJ 1995*, vol. 17, no. 5, pp. S573-577, Oct. 2001.

[5] D. R. Neal, J. Copland, and D. A. Neal, “Shack-Hartmann wavefront sensor precision and accuracy,” in *Advanced Characterization Techniques for Optical, Semiconductor, and Data Storage Components*, 2002, vol. 4779, pp. 148–161.

[6] A. Wang, P. Gill, and A. Molnar, “Light field image sensors based on the Talbot effect,” *Appl. Opt.*, vol. 48, no. 31, pp. 5897–5905, Nov. 2009.

[7] A. Wang and A. Molnar, “A Light-Field Image Sensor in 180 nm CMOS,” *IEEE J. Solid-State Circuits*, vol. 47, no. 1, pp. 257–271, Jan. 2012.

[8] H. F. Talbot, “Facts relating to optical science. No. IV,” *Lond. Edinb. Dublin Philos. Mag. J. Sci.*, vol. 9, no. 56, pp. 401–407, Dec. 1836.

[9] W. H. Southwell, “Wave-front estimation from wave-front slope measurements,” *J. Opt. Soc. Am.*, vol. 70, no. 8, pp. 998–1006, Aug. 1980.